

AD-A149843

RIA-84-U455

AD A149843

CONTRACTOR REPORT ARLCB-CR-84034

USADACS Technical Library



5 0712 01000901 6

# STRESS CORROSION CRACKING BEHAVIOR OF TUNGSTON HEAVY ALLOYS

JIN-GON CHUNG

DAVID J. DUQUETTE

MATERIALS ENGINEERING DEPT.  
RENSSELAER POLYTECHNIC INSTITUTE  
TROY, N. Y.

OCTOBER 1984



US ARMY ARMAMENT RESEARCH AND DEVELOPMENT CENTER  
LARGE CALIBER WEAPON SYSTEMS LABORATORY  
BENET WEAPONS LABORATORY  
WATERVLIET N.Y. 12189

APPROVED FOR PUBLIC RELEASE; DISTRIBUTION UNLIMITED

#### DISCLAIMER

The findings in this report are not to be construed as an official Department of the Army position unless so designated by other authorized documents.

The use of trade name(s) and/or manufacture(s) does not constitute an official indorsement or approval.

#### DISPOSITION

Destroy this report when it is no longer needed. Do not return it to the originator.

REPORT DOCUMENTATION PAGE		READ INSTRUCTIONS BEFORE COMPLETING FORM
1. REPORT NUMBER Contractor Report ARLCB-CR-84034	2. GOVT ACCESSION NO.	3. RECIPIENT'S CATALOG NUMBER
4. TITLE (and Subtitle) STRESS CORROSION CRACKING BEHAVIOR OF TUNGSTEN HEAVY ALLOYS		5. TYPE OF REPORT & PERIOD COVERED Final
		6. PERFORMING ORG. REPORT NUMBER
7. AUTHOR(s) Jin-Gon Chung David J. Duquette		8. CONTRACT OR GRANT NUMBER(s) DAAA22-81-C-0138
9. PERFORMING ORGANIZATION NAME AND ADDRESS Materials Engineering Department Rensselaer Polytechnic Institute Troy, NY 12180		10. PROGRAM ELEMENT, PROJECT, TASK AREA & WORK UNIT NUMBERS
11. CONTROLLING OFFICE NAME AND ADDRESS US Army Armament Research & Development Center Large Caliber Weapon Systems Laboratory Dover, NJ 07801-5001		12. REPORT DATE October 1984
		13. NUMBER OF PAGES 147
14. MONITORING AGENCY NAME & ADDRESS (if different from Controlling Office) U.S. Army Research & Development Center Benet Weapons Laboratory, SMCAR-LCB-RM Watervliet, N.Y. 12189		15. SECURITY CLASS. (of this report) UNCLASSIFIED
		15a. DECLASSIFICATION/DOWNGRADING SCHEDULE
16. DISTRIBUTION STATEMENT (of this Report)  Approved for Public Release; Distribution Unlimited		
17. DISTRIBUTION STATEMENT (of the abstract entered in Block 20, if different from Report)		
18. SUPPLEMENTARY NOTES  Dr. Joseph A. Kapp - Benet Weapons Laboratory, Project Engineer		
19. KEY WORDS (Continue on reverse side if necessary and identify by block number) High Density Alloys Stress Corrosion Cracking Fracture Fracture Mechanics Fracture Mechanisms		
20. ABSTRACT (Continue on reverse side if necessary and identify by block number) Stress corrosion cracking behavior of 90W-Ni-Fe (W-10) and 97W-Ni-Fe-Cu-Co (W-3) alloys has been studied in solutions of NaCl, NACE, and 10% H <sub>2</sub> SO <sub>4</sub> . The influences of electrochemical polarization, hydrogen catalyst, and heat treatment on K <sub>ISCC</sub> , static load crack growth rate, and fracture morphology were studied.  (CONT'D ON REVERSE)		

## 20. ABSTRACT (CONT'D)

The W-10 alloy exhibited SCC susceptibility in NaCl solution. Electrochemical polarization, addition of a hydrogen catalyst (As) to the NaCl solution and heat treatment in hydrogen increased SCC susceptibility. SCC susceptibility was also observed in the sulfide cracking solution and when cathodically charged in 10% H<sub>2</sub>SO<sub>4</sub> with a hydrogen catalyst (As). At the corrosion potential and anodic potentials in NaCl solution, SCC propagated by separation of tungsten-tungsten and tungsten-matrix interfaces with ductile rupture of the matrix. In other cases, cracks propagated by separation of tungsten-matrix and tungsten-tungsten interfaces with some cleavage of tungsten grains.

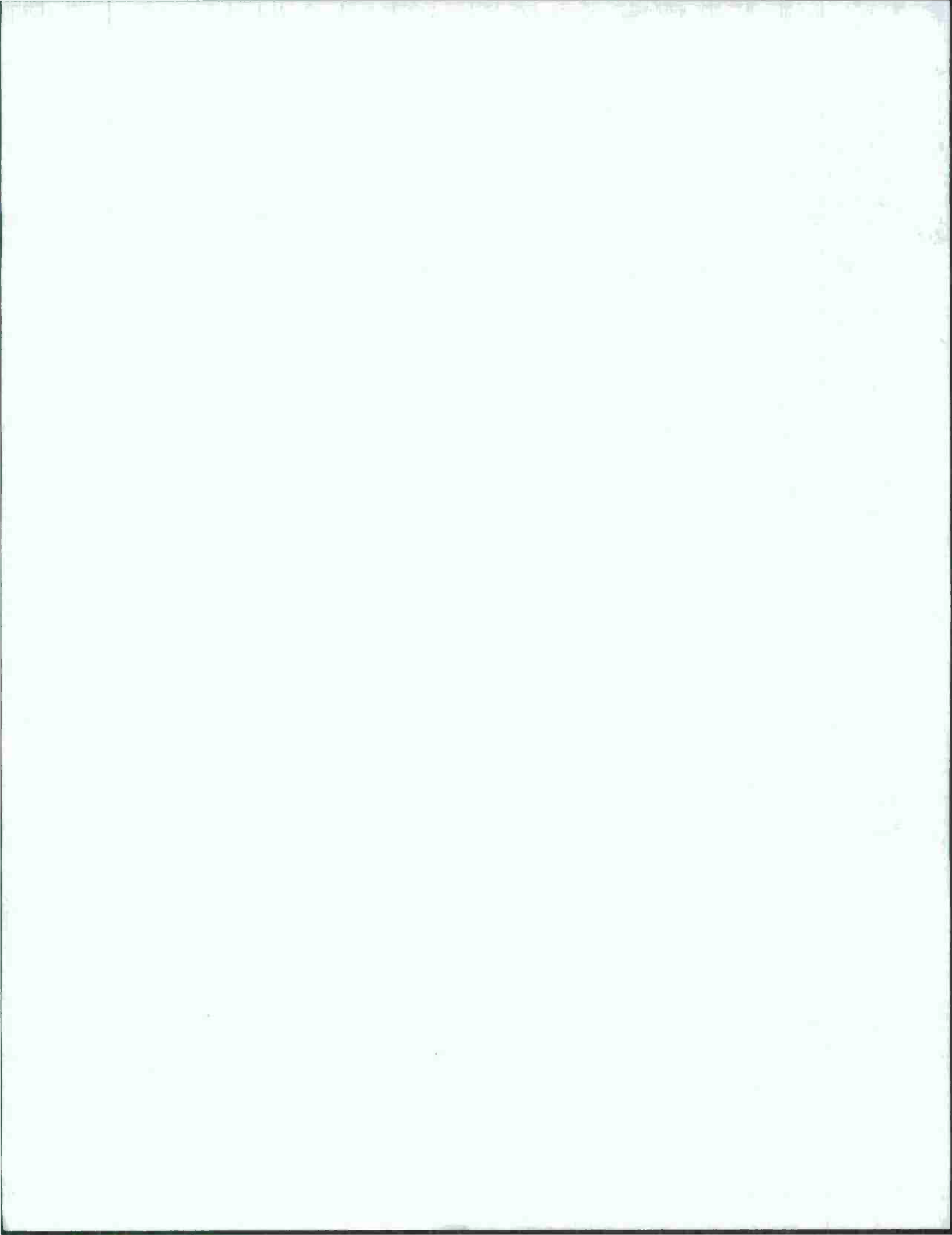
The W-3 alloy did not exhibit SCC susceptibility in NaCl solution, under any conditions. SCC did occur in the sulfide cracking solution and when cathodically charged in 10% H<sub>2</sub>SO<sub>4</sub> with a hydrogen catalyst (As), however, it was much more resistant than the W-10 alloy. Fracture occurred primarily by dimple formation in the matrix and cleavage of tungsten grains.

SCC in the W-10 alloy is thought to occur by electrochemical dissolution of the matrix. Small matrix volume and high tungsten contiguity in the W-3 alloy prevents cracks from growing even though severe matrix dissolution occurs.

The observed susceptibility of both alloys to cracking in the NACE recommended sulfide cracking solution and when cathodically charged in 10% H<sub>2</sub>SO<sub>4</sub> with As indicates that both alloys are highly susceptible to hydrogen embrittlement.

:





# CONTENTS

	Page
LIST OF TABLES.....	iv
LIST OF FIGURES.....	v
ACKNOWLEDGEMENTS.....	xii
ABSTRACT.....	xiii
1. INTRODUCTION.....	1
2. LITERATURE REVIEW.....	3
2.1 Alloy System.....	3
2.1.1 Sintering Mechanisms.....	4
2.1.2 Mechanical Properties and Embrittle- ment.....	5
2.1.3 Fracture Behavior.....	7
2.2 Stress Corrosion Cracking.....	9
2.2.1 Test Methods for SCC.....	9
2.2.1.1 Constant Strain and Constant Load Tests.....	9
2.2.1.2 Constant Strain Rate Tests	11
2.2.1.3 $K_{ISCC}$ Tests.....	12
2.2.2 SCC Mechanisms.....	14
2.2.2.1 The Film Rupture Model....	17
2.2.2.2 The Tunnel Model.....	18
2.2.2.3 The Adsorption Model.....	18
2.2.2.4 The Tarnish Rupture Model.....	21
2.2.2.5 The Selective Dissolution Model.....	21
2.3 Hydrogen Embrittlement.....	23
2.3.1 HE Mechanisms.....	26
2.3.1.1 The Decohesion Model.....	26
2.3.1.2 The Adsorption Model.....	26
2.3.1.3 The High Pressure Bubble Formation Model.....	26

	Page
2.3.1.4 The Hydrogen-Stimulated Plastic Deformation model...	27
2.3.1.5 The Hydride Formation Model.	28
2.3.2 Fracture Morphology.....	30
2.3.3 HE of Tungsten.....	30
3. EXPERIMENTAL PROCEDURE.....	32
3.1 Materials.....	32
3.2 Tension Tests.....	35
3.3 SCC Tests.....	35
3.4 Electrochemical Tests.....	42
3.5 Optical and Electron Microscopy.....	42
4. RESULTS.....	44
4.1 SCC Behavior.....	44
4.1.1 Effects of Polarization.....	44
4.1.2 Effects of Hydrogen Catalyst.....	52
4.1.3 Effects of Heat Treatment.....	61
4.1.4 Constant Load Tests.....	68
4.1.5 SCC in Sulfide Cracking Solution.....	68
4.2 Fractography.....	71
5. DISCUSSION.....	94
5.1 Effects of Polarization.....	94
5.2 Effects of Hydrogen Catalyst.....	104
5.3 Effects of Heat Treatment.....	104
5.4 Effects of Alloy Composition.....	106
5.5 Sulfide Stress Cracking.....	109
5.6 Mechanisms.....	111
6. CONCLUSIONS.....	114
7. SUGGESTIONS FOR FUTURE WORK.....	117
8. REFERENCES.....	118
9. APPENDICES.....	124
I. Slow Strain Rate Tests.....	124
II. Crack Initiation Tests.....	127
III. Copper Electrodeposition.....	132

## LIST OF TABLES

	Page
Table 1	Chemical Compositions of the Alloys.... 33
Table 2	Mechanical and Physical Properties of the Alloys..... 37
Table 3	Compositions of the W-10 Alloy Phases.. 63
Table 4	Compositions of the W-3 Alloy Phases... 64
Table 5	Results of Slow Strain Rate Tests on Pure Tungsten..... 125
Table 6	Compositions and Operating Conditions of Dilute Cyanide Bath..... 133
Table 7	Compositions and Operating Conditions of Copper Sulfate Bath..... 134



## LIST OF FIGURES

	Page
Figure 1      Schematic Showing Basic Principle of Modified WOL Specimen <sup>25</sup> .....	15
Figure 2      Difference in Behavior for Modified WOL and Cantilever-Beam Specimens <sup>25</sup> .....	16
Figure 3      Schematic Representation of Crack Propaga- tion by the Film-Rupture Model, as Suggested by Staehle <sup>31</sup> .....	19
Figure 4      Schematic of Tunnel Model, Showing the Initiation of a Crack by the Formation of Corrosion Tunnels at a Slip Step and the Subse- quent Rupture of the Metal Ligaments <sup>36,37</sup> .....	20
Figure 5      Schematic of Tarnish-Rupture Model, Modi- fied to Incorporate Intergranular Penetra- tion <sup>45</sup> .....	22
Figure 6      Schematic Illustration of Various Sequential Processes Involved in Embrittlement of Ferrous Alloys by External Hydrogen.....	24
Figure 7      Summary of Hydrogen Processes: Sources Leading to Hydrogen in Solution, Transport Leading to Accumulation at Microstructural Locations, and Finally Fracture. Dashed Line Refers to Cleavage of Hydrides. From Thompson and Bernstein <sup>51</sup> .....	25

	Page
Figure 8 Schematic Showing the Mechanism of Hydride Embrittlement by Stress Induced Hydride Formation. <sup>58</sup> .....	29
(a) Flux of Hydrogen to the Crack Tip Due to the Reduction of the Hydrogen Chemical Potential in the Tensile Stress Field.....	29
(b) Formation of the Hydride Due to the Reduction of the Hydride Chemical Potential by the Applied Stress.....	29
(c) Cleavage of the Hydride Along Its Cleavage Plane Resulting in Crack Advance.....	29
(d) Repetition of (a).....	29
Figure 9 Optical Micrographs of (a) the W-10 Alloy and (b) the W-3 Alloy.....	34
Figure 10 Tensile Specimen Geometry.....	36
Figure 11 Modified WOL Specimen.....	39
Figure 12 Modified WOL Specimen Showing Crack Arrest Line.	41
Figure 13 Polarization Curve for the W-10 Alloy in Aerated 3% NaCl Solution.....	45
Figure 14 Polarization Curve for the W-3 Alloy in Aerated 3% NaCl Solution.....	46
Figure 15 SCC Behavior of the W-10 Alloy in Aerated 3% NaCl Solution.....	48

	Page
Figure 16 Polarization Effects on the $K_{ISCC}$ and Crack Growth Rate of the W-10 Alloy in 3% NaCl Solution.....	50
Figure 17 Optical Micrograph for the W-10 Alloy Specimen Showing Crack Propagation Through the Dissolved Matrix Ahead of the Crack Tip, at 0.2 V vs. SCE in 3% NaCl Solution.....	51
Figure 18 Optical Micrograph for the W-10 Alloy Specimen Through the Tungsten-Matrix and Tungsten-Tungsten Interfaces, at -1.2 V vs. SCE in 3% NaCl Solution	53
Figure 19 Specimen Surface of the W-10 Alloy Showing Severe Corrosion Attack, Especially in the Matrix Area	54
Figure 20 Effect of As Addition on the Cathodic Polarization Curves for the W-10 Alloy in Aerated 3% NaCl Solution.....	56
Figure 21 Effect of As Addition on the Cathodic Polarization Curves for the W-3 Alloy in Aerated 3% NaCl Solution.....	57
Figure 22 Influence of a Hydrogen Catalyst (As) on the $K_{ISCC}$ and Crack Growth Rate of the W-10 Alloy at -1.2 V vs. SCE in NaCl Solution.....	59
Figure 23 The Stress Intensity Factor vs. Crack Growth Rate Curves for the W-10 Alloy at -1.2 V vs. SCE (a) in 10% $H_2SO_4$ Solution Containing 60 ppm of As, and (b) in 3% NaCl Solution Containing	

	Page
60 ppm of As.....	60
Figure 24 SCC Behavior of the W-3 Alloy at -1.2 V vs. SCE in 10% H <sub>2</sub> SO <sub>4</sub> Containing 60 ppm of As.....	62
Figure 25 Optical Micrographs Showing Microstructure of the Heat Treated (a) W-10 Alloy and (b) W-3 Alloy.....	65
Figure 26 Influence of Heat Treatment in Argon Atmosphere on the SCC Behavior of the W-10 Alloy in NaCl Solution. No Remarkable Differences Exist Between the As-Received and the Heat Treated Specimens.....	67
Figure 27 Influence of Heat Treatment in Hydrogen Atmos- phere on the SCC Behavior of the W-10 Alloy in NaCl Solution. K <sub>ISCC</sub> Was Lowered and Crack Growth Rate Was Increased.....	69
Figure 28 Influence of Heat Treatment in Hydrogen Atmos- phere on the K <sub>ISCC</sub> and Crack Growth Rate of the W-10 Alloy at -1.2 V vs. SCE in NaCl Solu- tion. K <sub>ISCC</sub> was lowered and Crack Growth Rate Was Not Changed Very Much.....	70
Figure 29 SCC Behavior of the W-10 Alloy in Sulfide Cracking Solution.....	72
Figure 30 Heat Treatment Effects on the K <sub>ISCC</sub> and Crack Growth Rate of the W-3 Alloy in Sulfide Cracking Solution.....	73



	Page
Figure 31 Fractographs for Tension Specimen of the W-10 Alloy, Showing Rupture of the Matrix (A), Tungsten-Tungsten Interfaces (B), Cleavage of the Tungsten Particles (C), Dimples in the Matrix (D), and Secondary Cracks (E).....	74
Figure 32 Fracture Surface of the W-10 Alloy in the Pre-cracked Region.....	75
Figure 33 Fracture Surface of the W-10 Alloy Specimen Tested at the Open-Circuit Potential in 3% NaCl Solution.....	77
Figure 34 Fracture Morphology of the W-10 Alloy Sample Tested at -0.2 V vs. SCE in 3% NaCl Solution...	78
Figure 35 Fractograph for the W-10 Alloy Sample Tested at -1.2 V vs. SCE in NaCl Solution.....	79
Figure 36 Scanning Electron Micrographs for the W-10 Alloy Showing Regions of Brittle Interphase Boundary Precipitates Exposed on Fracture Surface.....	80
Figure 37 Fracture Surface of the W-10 Alloy Showing Precipitates Exposed on the Tungsten-Tungsten Grain Boundaries.....	81
Figure 38 Fractographs for a Tension Specimen of the W-3 Alloy Showing Dimples (A) and River Lines (B) in the Matrix, Cleavage of the Tungsten Particles (C), and Tungsten-Tungsten Interfaces (D).....	82

	Page
Figure 39 Fracture Surface of the W-3 Alloy in the Pre-cracked Region, Showing Ductile Rupture of the Matrix with Cleavage of the Tungsten Grains.	84
Figure 40 Fracture Appearance of the W-10 Alloy in 3% NaCl Solution Containing 60 ppm of As.....	85
Figure 41 Fracture Morphology of the W-10 Alloy Tested at -1.2 V vs. SCE in 10% H <sub>2</sub> SO <sub>4</sub> Containing 60 ppm of As.....	86
Figure 42 Fracture Appearance of the W-3 Alloy Tested at -1.2 V vs. SCE in 10% H <sub>2</sub> SO <sub>4</sub> Containing 60 ppm of As.....	87
Figure 43 Fracture Morphology of the Heat Treated W-10 Alloy Sample Tested in 3% NaCl Solution.....	88
Figure 44 Fracture Morphology of the W-3 Alloy Sample Tested in 3% NaCl Solution Under Constant Load..	90
Figure 45 Fractographs for the W-10 Alloy Tested in the Sulfide Cracking Solution.....	91
Figure 46 Fracture Appearance of the W-3 Alloy Tested in the Sulfide Cracking Solution.	
(a) Dimples in the Matrix.....	92
(b) Cleavage of the Tungsten Grains and Dimples in the Matrix.....	92
(c) Higher Magnification of the Cleavage in (b)	93
(d) Higher Magnification of the Dimples in (b).	93

	Page
Figure 47 Polarization Curves of W-3.5Ni-1.5Fe, W, and Ni-24Fe-21W Exposed to 0.1M NaCl, pH = 9 <sup>78</sup> ....	95
Figure 48 Schematic of the Crack Blunting by Anodic Dissolution in the Matrix of the Crack Surface Due to the Lack of Passive Film.....	99
Figure 49 $K_I$ - da/dt Curves Showing That Crack Growth Rate in the Plateau Region is Independent of the Specific Anion Present and Its Aggressiveness, at -1.2 V vs. SCE.....	102
Figure 50 Schematic Representation of Stresses Around A Tungsten Grain From the Matrix During Tensile Testing <sup>3</sup> .....	107
Figure 51 Load vs. Displacement Curves from Slow Strain Rate Tests of Pure Tungsten in Air and 3% NaCl Solution.....	126
Figure 52 Optical Micrograph Showing Crack Initiation and Propagation of the Cu Diffused W-10 Alloy in 3% NaCl Solution.....	129
Figure 53 Fracture Appearance of the Cu Diffused W-10 Alloy Specimen Tested in 3% NaCl Solution.....	130
Figure 54 EDAX Spectrum of (a) the As-Received W-10 Alloy and (b) the Cu Diffused W-10 Alloy.....	131

## ACKNOWLEDGEMENT

The author wishes to express his gratitude to Professor David J. Duquette for the encouragement, guidance, and personal freedom received during the course of this investigation. The author also wishes to thank Professors Norman S. Stoloff and Roger N. Wright for many helpful suggestions.

Special thanks are extended to Dr. Joseph A. Kapp and the Watervliet Arsenal for many helpful discussions and providing experimental materials.

The author is very grateful to N. Lewis and C. Chalek for performing EPMA work, and James Might and Richard Wistrom for various assistance connected with this investigation.

Finally, the author wishes to thank his parents and lovely wife, Min-Sook, for the understanding, moral support, and the sacrifices they made to allow the completion of this work.



## ABSTRACT

Stress corrosion cracking behavior of 90W-Ni-Fe (W-10) and 97W-Ni-Fe-Cu-Co (W-3) alloys has been studied in solutions of NaCl, NACE and 10%  $H_2SO_4$ . The influences of electrochemical polarization, hydrogen catalyst, and heat treatment on  $K_{ISCC}$ , static load crack growth rate, and fracture morphology were studied.

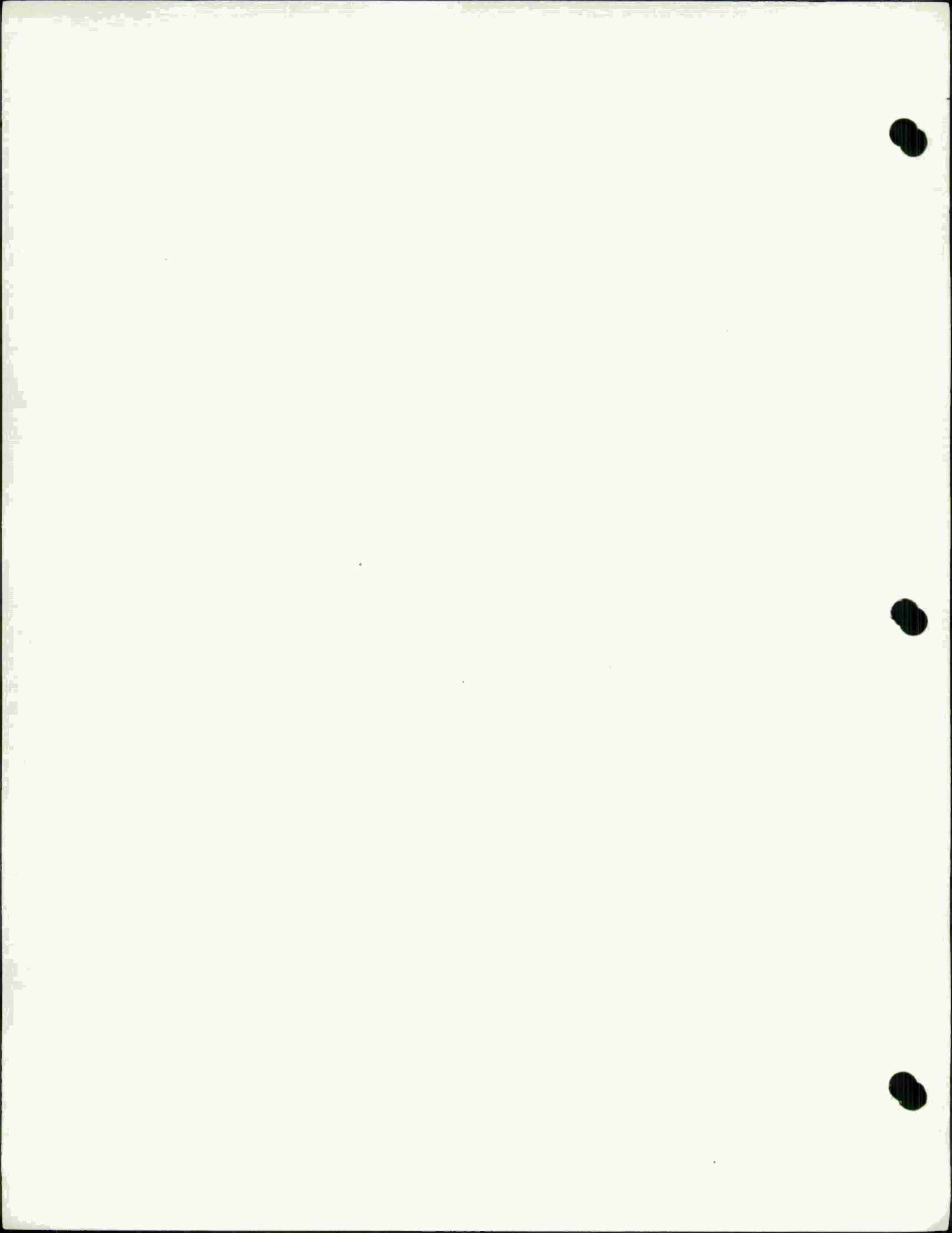
The W-10 alloy exhibited SCC susceptibility in NaCl solution. Electrochemical polarization, addition of a hydrogen catalyst (As) to the NaCl solution and heat treatment in hydrogen increased SCC susceptibility. SCC susceptibility was also observed in the sulfide cracking solution and when cathodically charged in 10%  $H_2SO_4$  with a hydrogen catalyst (As). At the corrosion potential and anodic potentials in NaCl solution, SCC propagated by separation of tungsten-tungsten and tungsten-matrix interfaces with ductile rupture of the matrix. In other cases, cracks propagated by separation of tungsten-matrix and tungsten-tungsten interfaces with some cleavage of tungsten grains.

The W-3 alloy did not exhibit SCC susceptibility in NaCl solution, under any conditions. SCC did occur in the sulfide cracking solution and when cathodically charged in 10%  $H_2SO_4$  with a hydrogen catalyst (As), however, it was much more resistant than the W-10 alloy. Fracture

occurred primarily by dimple formation in the matrix and cleavage of tungsten grains.

SCC in the W-10 alloy is thought to occur by electrochemical dissolution of the matrix. Small matrix volume and high tungsten contiguity in the W-3 alloy prevents cracks from growing even though severe matrix dissolution occurs.

The observed susceptibility of both alloys to cracking in the NACE recommended sulfide cracking solution and when cathodically charged in 10%  $H_2SO_4$  with As indicates that both alloys are highly susceptible to hydrogen embrittlement.



## PART 1

### INTRODUCTION

Due to their high densities and strengths, tungsten-based materials known as heavy alloys are used in mass balancing, inertial systems, structural radioactive shielding, heavy duty electrical contacts, artillery shell cores, etc.

The alloys are manufactured by liquid phase sintering. In this process, tungsten dissolves in the nickel-iron or nickel-copper liquid so that finally an apparently two-phase structure is obtained, consisting of rounded tungsten grains and a matrix solid solution of tungsten-nickel-iron or tungsten-nickel copper. The detailed characteristics of the manufacturing process have been documented previously.<sup>1</sup>

The mechanical properties of heavy alloys are affected primarily by the nickel:iron and nickel:copper ratios, tungsten contiguity, sintering conditions, and conditions of post sintering heat treatment. For the tungsten-nickel-iron alloys the optimum strength and ductility is found when the nickel:iron ratio is 7:3 to 3:7.<sup>1,2</sup> The maximum elongation depends strongly upon tungsten contiguity. A high contiguity produces a lower ductility.<sup>3</sup> The lower sintering temperature yields better mechanical properties due to finely distributed porosities and reduction of grain



growth.<sup>4</sup> Annealing combined with quenching as the post sintering heat treatment improves strength and ductility.<sup>5,6</sup>

The influence of heat treatment is connected with grain size, distribution of impurities, intermetallic compound formation, and matrix phase composition.

Although numerous studies on the sintering mechanism, mechanical properties, and fracture behavior have been done for liquid phase sintered tungsten heavy alloys, little work has been done on the stress corrosion cracking behavior of these alloys.

This investigation was undertaken with the aim of examining the stress corrosion cracking behavior of the tungsten heavy alloys in several aqueous solution. The overall investigation involves the evaluation of the  $K_{ISCC}$  and static load crack growth rate performances in sodium chloride solution and NACE recommended sulfide cracking solution. Additional variables being studied in this program include solution chemistry, influence of heat treatment, and influence of electrochemical polarization.

## PART 2

### LITERATURE REVIEW

#### 2.1 Alloy System

The group of tungsten-based alloys known as heavy alloys by virtue of their high density (16 to 18.5 g/cm<sup>3</sup>) have found an increasing number of applications in mass balancing and inertial systems, for example, gyroscopes and vibration dampeners, and in ordnance, radioactive shielding and heavy duty electrical contacts.

The alloys are manufactured by first pressing mixed powders to produce a green compact which is then sintered in a dry hydrogen atmosphere at a temperature sufficient to cause melting of the non-tungsten components of the system.

The liquid phase dissolves some of the tungsten and to minimize surface energy some tungsten particles grow at the expense of others. This is thought to occur by dissolution and precipitation,<sup>7</sup> and coalescence.<sup>8</sup> The final structure is an apparently two phase structure containing rounded tungsten grains and a matrix solid solution.

The non-tungsten components which have received the most study are nickel-iron and nickel-copper. Nickel is used because it has the high solubility for tungsten necessary for its transport during sintering; according

to Ellinger and Sykes,<sup>9</sup> nickel can dissolve up to 45 wt. pct tungsten in the binary system at 1495°C. The ternary alloying element is used to reduce the melting point of the matrix and hence enable lower sintering temperatures to be employed, but both iron and copper reduce the solubility of tungsten in the nickel.

### 2.1.1 Sintering Mechanisms

In 1938, Price, Smithells and Williams<sup>7</sup> discovered the heavy alloys where they were able to achieve full density by liquid-phase sintering tungsten-nickel-copper at temperature well below half of the absolute melting temperature of tungsten. The growth of the tungsten particles was attributed to the dissolution of the small tungsten spheroids with simultaneous precipitation of tungsten from the molten matrix onto the larger spheroids, the process being driven by the difference in surface energy between the smaller and larger spheroids.

A theory for the sintering of metal particles was proposed by Kuczynski<sup>10</sup> in 1949, when he found that the interface formed between two particles during sintering changed at different rates if the growth was due to either (1) viscous or plastic flow, (2) evaporation and condensation, (3) volume diffusion, or (4) surface diffusion. A theoretical treatment<sup>11</sup> of these various diffusion mechanisms showed that the predominant mechanism responsible for particle growth during sintering under any

particular set of sintering conditions could be identified.

Cannon and Lenel<sup>12</sup> divided the sintering process into three stages, "liquid flow", "solution and reprecipitation" and "solid phase sintering". The density of the compact increases during the liquid flow stage, and the particles grow during the other stages. The final particle size should be limited because a very low dihedral angle is reached between two solid-liquid surfaces and the liquid phase will not permit two particles of the solid phase to touch each other as long as the particles have different orientations.

Zukas and Sheinberg<sup>9</sup> proposed that the spheroids coalesce when contact is made between spheroids of similar orientations, and that this process occurs throughout the liquid phase sintering cycle. Undoubtedly, dissolution of the small spheroids and reprecipitation of tungsten from the molten matrix onto the larger spheroids occurs simultaneously, but the spheroid growth from this process is slow.

### 2.1.2 Mechanical Properties and Embrittlement

The mechanical properties of tungsten heavy alloys are affected primarily by the tungsten content, nickel:iron ratio, sintering condition, and post-sintering heat treatment condition. As the tungsten content increases, there is less chance for the tungsten grain



to be completely surrounded by matrix phase.<sup>13</sup> Accordingly, there is a higher tungsten contiguity as the volume fraction of solid increases. Contiguity is defined as the ratio of the surface area involved in tungsten-tungsten contacts and the surface area of tungsten grains. In tungsten heavy alloys, the maximum elongation depends strongly upon its contiguity. A high contiguity produces a lower ductility.<sup>3</sup> For the tungsten-nickel-iron alloys, the optimum strength and ductility is found when the nickel:iron ratio is 7:3 to 3:7.<sup>1,2</sup> The lower sintering temperature yields better mechanical properties due to finely distributed porosities and reduction of grain growth.<sup>4</sup> Annealing combined with quenching as the post sintering heat treatment improves strength and ductility.<sup>5,6</sup> The influence of heat treatment is connected with grain size, impurity distribution, intermetallic compound formation, and matrix phase composition.

The embrittlement of heavy alloys is caused by intermetallic phase formation, impurity segregation, hydrogen embrittlement, shrinkage pore formation, etc. From Charpy impact tests with 90 W-5 Ni-5 Fe alloy, Edmonds and Jones<sup>14</sup> found that intermetallic compound formation at the matrix-tungsten interfaces was responsible for embrittlement. This intermetallic compound formation has also been suggested as the cause of embrittlement in slowly cooled alloys with a nickel:iron ratio of 7:3.<sup>15</sup>

However, Henig, et al.<sup>16</sup> claimed no detrimental effect from this intermetallic compound. Other investigators<sup>1</sup> have been unable to confirm the existence of this phase in embrittled material with a nickel:iron ratio of 1:1.

Several reports<sup>14,17</sup> have shown a strong impurity influence, wherein the elements such as phosphorus and sulfur segregate to the tungsten-matrix interface during slow cooling from elevated temperatures.

Yoon et al.<sup>18</sup> found strength and ductility degradation with heat treatment in a hydrogen atmosphere. Sczerzenie and Rogers<sup>19</sup> have found that the sensitivity of the heavy alloys to hydrogen embrittlement is dependent on the matrix composition in the tungsten-nickel-iron alloys. The effect of hydrogen is thought to weaken the tungsten-matrix interfaces.

Kang et al.<sup>20</sup> have shown mechanical property decrements due to rapid cooling from the sintering temperature. The formation of matrix phase solidification porosity with rapid cooling is quite detrimental to the properties: Churn and Yoon<sup>4</sup> have given a clear demonstration of the porosity effect.

### 2.1.3 Fracture Behavior

In tungsten heavy alloys, fracture usually occurs by one or more of the following four possible paths:

- (1) failure of the tungsten-tungsten grain boundaries,

- (2) separation of the tungsten-matrix interfaces,
- (3) failure in the matrix phase, and
- (4) cleavage of the tungsten grains.

The fracture behavior of the tungsten heavy alloys has been studied by several investigators. However, there is some controversy in the literature concerning the relationships between both strength and ductility with fracture behavior. Edmonds and Jones<sup>14</sup> reported that tough material requires good adhesion at the matrix-tungsten interfaces such that failure occurs by ductile rupture of the matrix with separation of the tungsten-tungsten interfaces and/or cleavage of the tungsten grains.

Sczerzenie and Rogers<sup>19</sup> showed that the fracture behavior of the tungsten phase in heavy alloys is controlled by the strength of the tungsten-matrix interface. When the matrix-tungsten interface is strong, fracture occurs by transcrystalline cleavage of the tungsten phase with a knife edge failure in the matrix. When the matrix-tungsten is weakened by hydrogen, there is an early separation of tungsten particles and matrix, and the matrix can neck down and rupture independent of the tungsten particles.

However, Brandon et al.<sup>21</sup> demonstrated that the presence of the strong tungsten-tungsten grain

boundaries is obviously a key to the strong and ductile material.

## 2.2 Stress Corrosion Cracking

Stress corrosion cracking (SCC) is defined as premature cracking under the simultaneous action of a generally specific corrosive agent and a tensile stress. To obtain the specific result of SCC, four primary agents must be concurrently contributing:

- (1) a specific alloy composition,
- (2) a unique microstructure resulting from metallurgical processing,
- (3) a tensile stress at exposed surfaces, and,
- (4) a specific environment.

### 2.2.1 Test Methods for SCC

#### 2.2.1.1 Constant Strain and Constant Load

Tests. The traditional method of determining SCC resistance of an alloy has been to expose stressed, smooth specimens in the environment of interest. Such specimens usually are exposed under applied stresses near or beyond their yield strengths. Specimens may be tested under conditions of constant strain or constant load. Examples of constant strain specimens are plastically deformed U-bends, C-rings, and beams supported in restraining jigs. The major advantages of constant strain specimens



are that they are compact and relatively inexpensive, which makes them suitable for multiple, long term exposure tests or exposure in restricted condition, e.g., in tubing or casing. A disadvantage of constant strain tests is that stress levels are not known accurately and are difficult to reproduce from specimen to specimen.

Constant load tests employ either tensile or bend specimens. They require more complex apparatus than constant strain tests, but they have the advantage that the stress level is well defined and easily measured. Loads may be applied by weights, levers, springs, or hydraulically. An advantage of constant load tests compared to constant strain tests is that crack propagation decreases the cross sectional area and increases the net section stress. Consequently, such tests are more likely to lead to early and total failure than are constant strain tests.

Both types of specimens are normally exposed in the environment of interest for a predetermined period. The susceptibility to SCC may be expressed quantitatively by time to failure. Such tests have produced much useful information, particularly for low strength alloys. However, results can be very misleading because time to failure represents the sums of the times required for crack initiation, subcritical crack growth, and fast fracture. If an alloy is not susceptible to or is highly



resistant to pitting, failure may not occur within the exposure period and the alloy may be classified as immune to SCC, when, in fact, it may be highly susceptible to crack propagation. To be sure of complete immunity, it would be necessary to expose specimens for excessive periods. This is impractical in most engineering applications.

A method which has frequently been used to speed up the generation of SCC susceptibility data is to increase the severity of tests by altering the composition of the environment, raising the temperature, or introducing a notch or a precrack. While notched or precracked specimens are very useful in the study of crack propagation kinetics and crack arrest conditions, they have the disadvantage of eliminating the initiation stage which is rate controlling in many systems.

2.2.1.2 Constant Strain Rate Tests. Many of the disadvantages of constant strain and constant load tests are eliminated by testing smooth specimens at a constant strain rate. The constant strain rate test is a form of simple tensile test in which a smooth specimen is pulled in tension in the environment of interest at a constant strain rate until failure occurs. The major advantage of the test is its ability to produce rapid, positive indications of SCC susceptibility. SCC

growth markedly decreases the ductility of the specimen and results in the formation of secondary cracks near the main fracture. The test requires a few days at most, depending upon the ductility of the alloy and the strain rate.

Conceptually, the constant strain rate test achieves a balance between the rates of mechanical processes which promote ductile failure and the rates of corrosion processes which promote SCC propagation and brittle fracture. So, the choice of the strain rate used is the most important factor governing the outcome of a test. In most systems, SCC occurs at strain rates between  $10^{-5}$  to  $10^{-7}$ /sec. However, the optimum rate will vary with material and environment and should be determined for each case.

SCC susceptibility may be classified by comparing time to failure, percent reduction in area, percent elongation, plastic strain to failure, or energy absorbed prior to fracture.

**2.2.1.3 K<sub>ISCC</sub> Tests.** The application of linear elastic fracture mechanics concepts to study SCC has met with considerable success. Because stress corrosion attack would be expected to occur in the highly stressed region at the crack tip, it is logical to use the stress intensity factor to characterize the mechanical component of the driving force in SCC. Sufficient data have been

published to support this observation.<sup>22-24</sup>

The most widely used specimens for  $K_{ISCC}$  tests are the cantilever-beam specimen under constant load and the wedge-opening-loading (WOL) specimen under constant displacement conditions (modified WOL specimen) that was developed by Novak and Rolfe.<sup>25</sup> The  $K_{ISCC}$  value for a particular material and environment is the plane-strain stress intensity threshold below which subcritical cracks will not propagate. Since Brown<sup>26,27</sup> introduced the  $K_{ISCC}$  threshold concept by using precracked cantilever-beam specimens, it has been widely used for studying the subcritical crack extension characteristics.

In the cantilever-beam technique, approximately 10 precracked specimens are required to establish  $K_{ISCC}$  for a particular material and environment. After first establishing the critical stress intensity factor for failure in air,  $K_{IC}$ , subsequent specimens are dead-weight loaded to successively lower  $K_I$  levels in the environment and times to failure recorded.

The WOL fracture specimen was originally developed by Manjoine.<sup>28</sup> Subsequently, Manjoine<sup>29</sup> published a detailed review of the work with this specimen, introducing the original design and stress analysis, and Wessel<sup>30</sup> presented a report describing the application of the WOL specimen to fracture testing.

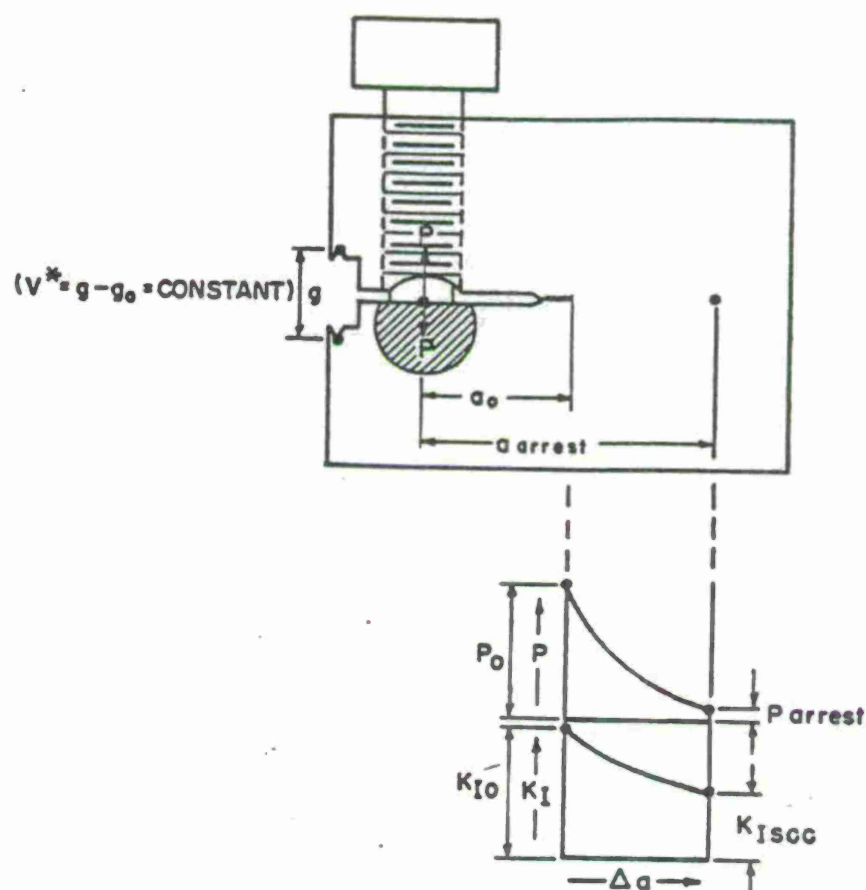
The WOL specimen was modified by the use of



a bolt and loading tup so that it can be self-stressed without using a tensile machine. The crack opening is fixed by the bolt, and the loading is by constant displacement rather than by constant load as in the cantilever-beam specimen. Because a constant crack-opening-displacement (COD) is maintained throughout the test, the force,  $P$ , decreases as the crack length,  $a$ , increases. In cantilever-beam testing, the  $K_I$  value increases ( $a$  increases and  $P$  is constant), which lead to fracture for each specimen; in contrast in the modified WOL specimen, the  $K_I$  value decreases ( $a$  increases and  $P$  decreases), which leads to crack arrest. The effect of decrease in  $P$  more than compensates for the increase in  $a$ . Basic principle of modified WOL specimen is schematically illustrated in Figure 1. A comparison of these two types of behavior is shown in Figure 2. Thus, only a single specimen is required to establish the  $K_{ISCC}$  level because  $K_I$  approaches  $K_{ISCC}$  in the limit. However, duplicate specimens are usually tested to demonstrate reproducibility.

### 2.2.2 SCC Mechanisms

The various models of SCC has been proposed and can be largely divided into two basic classes: those which consider that crack propagation proceeds by anodic dissolution at the crack tip and those which consider



\* V - CRACK-OPENING DISPLACEMENT  
(COD) FOR A RIGID BOLT

Figure 1 Schematic Showing Basic Principle of Modified WOL Specimen.<sup>25</sup>



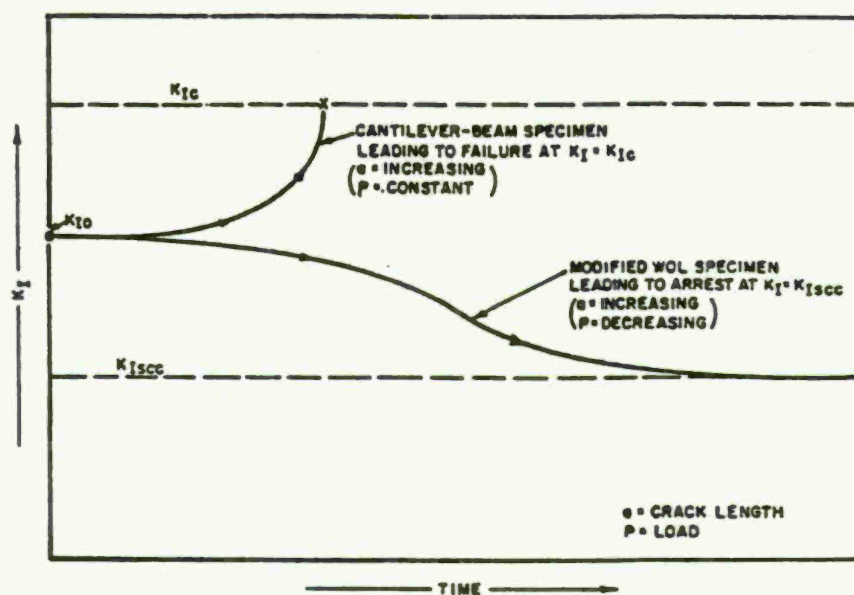


Figure 2 Difference in Behavior for Modified WOL and Cantilever-Beam Specimens.<sup>25</sup>

that crack propagation is essentially mechanical.

2.2.2.1 The Film Rupture Model. This model referred to as the slip-dissolution model by some investigators,<sup>31</sup> was originally developed by Champion<sup>32</sup> and Logan.<sup>33</sup> The basic concept is that a protective surface film is ruptured by localized plastic deformation at the crack tip, permitting rapid anodic dissolution of the exposed substrate while the non-deforming crack walls remain protected by the film. The potential difference between filmed and unfilmed surface could constitute a strong driving force for the reaction.

Since such film breakdown could occur also on non-susceptible alloys and in non-cracking environments, Scully<sup>34,35</sup> placed great emphasis on the relationship between two kinetic processes: creating fresh metal area and film growth on the fresh metal area. The essential requirement for crack propagation was defined as a condition of "inadequate repassivation". If repassivation took place too rapidly then too little corrosion would have occurred for an increment of crack growth to have been achieved. If repassivation took place too slowly, then too much corrosion would have occurred and, instead of highly localized corrosion, which is necessary for cracking, attack over a broad front would have occurred. Repassivation at some unspecified rate relative to the

rate of creation of fresh metal surface was considered to be the essential condition for SCC.

However, Staehle<sup>31</sup> has the different view that the crack tip becomes completely repassivated during propagation, and that film rupture results from the emergence of slip steps through the passive film. So, the crack propagation is thought to be discontinuous. This idea is illustrated in Figure 3.

2.2.2.2 The Tunnel Model. Swann et al.<sup>36,37</sup> proposed that cracking is initiated at slip steps by the formation of arrays of fine corrosion tunnels which grow in length and diameter until the remaining metal ligaments fail by ductile rupture as shown in Figure 4. The crack is then thought to propagate discontinuously by repeated cycles of tunnel growth and ductile fracture. The fracture surfaces would be expected to exhibit a series of grooves extending in the direction of crack propagation, with the walls between neighboring grooves matching peak-to-peak on the opposite faces.

2.2.2.3 The Adsorption Model. It is postulated by Petch<sup>38</sup> that specific species adsorb and interact with strained bonds at the crack tip, reducing bond strength and the surface energy required to form a crack and permitting brittle fracture at low stresses. As yet, there is no direct evidence for the hypothesized

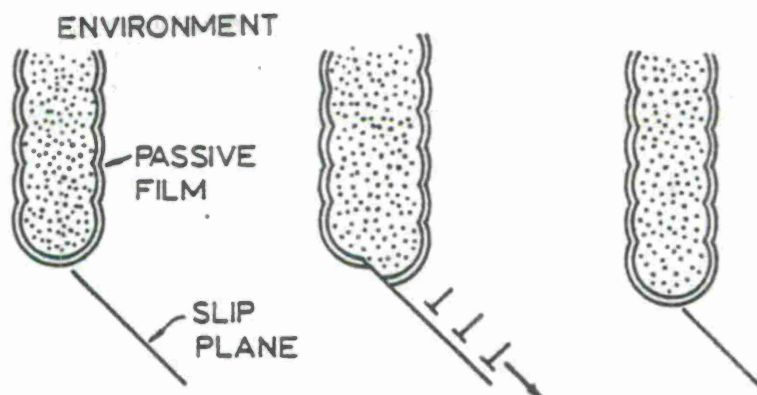


Figure 3 Schematic Representation of Crack Propagation by the Film-Rupture Model, As Suggested by Staehle.<sup>31</sup>

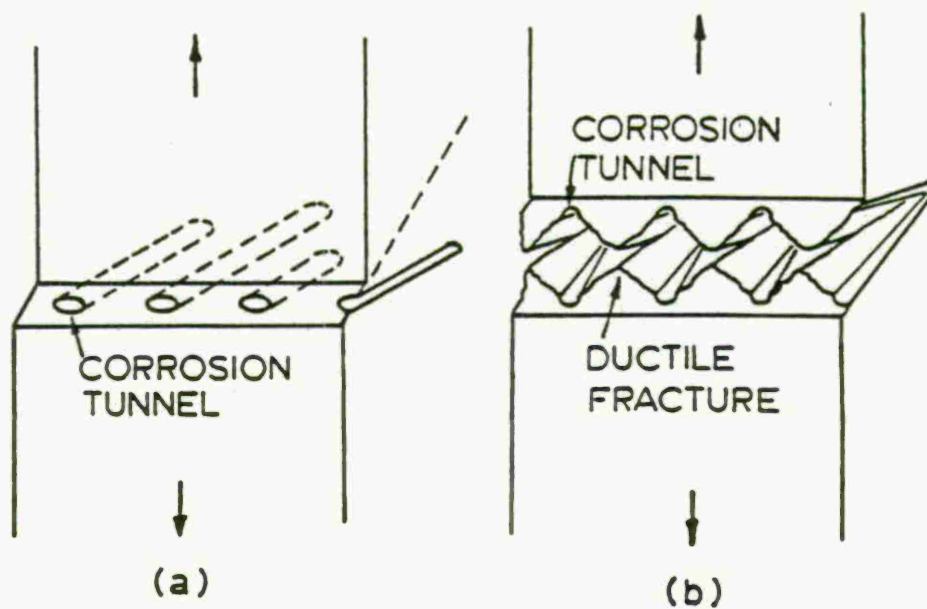


Figure 4 Schematic of Tunnel Model Showing the Initiation of a Crack by the Formation of Corrosion Tunnels at a Slip Step and the Subsequent Rupture of the Metal Ligaments.<sup>36,37</sup>



adsorption induced reduction in bond strength, but the concept has been applied to various embrittlement phenomena such as liquid-metal embrittlement,<sup>39</sup> hydrogen embrittlement,<sup>40</sup> corrosion fatigue,<sup>41</sup> and SCC.<sup>42</sup>

**2.2.2.4 The Tarnish Rupture Model.** This model was initiated by Forty et al.<sup>43</sup> to explain SCC of copper-zinc alloys in aqueous ammonia, and developed by McEvily and Bond.<sup>44</sup> In its most recent form, it has been referred to as stress-assisted intergranular corrosion.<sup>45</sup> The model proposes that the grain boundary ahead of the crack tip is penetrated by a brittle oxide and that propagation proceeds by the repeated formation and rupture of this layer as shown in Figure 5. Rupture of the brittle tarnish was attributed to elastic strains introduced by creep in the surrounding metal.

**2.2.2.5 The Selective Dissolution Model.** This model was proposed by Forty<sup>46</sup> to account for the transgranular SCC of alpha brass in aqueous ammonia solutions. It was suggested that the selective dissolution of zinc from the alloy results in vacancy injection which sufficiently restricts local plastic deformation to permit the initiation of a cleavage crack. The crack was thought to propagate at high speeds until it encounters a pre-existing slip-band, at which arrest occurs by plastic blunting. Repeated cycles of this process were believed

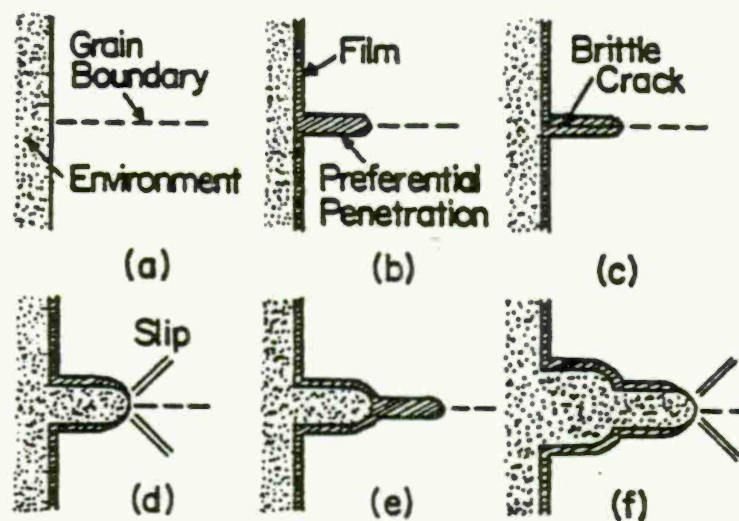


Figure 5 Schematic of Tarnish-Rupture Model, Modified to Incorporate Intergranular Penetration.<sup>45</sup>

to lead to crack propagation by discontinuous cleavage.

### 2.3 Hydrogen Embrittlement

Hydrogen induced losses in strength or ductility are called hydrogen embrittlement (HE). In general, two sources of hydrogen may be available to initiate failure: internal or solute hydrogen and external. In the former case, the hydrogen must reach the point at which failure occurs by diffusion<sup>47</sup> and/or by dislocation sweeping.<sup>48,49</sup> The hydrogen diffusivity in most systems is quite high and exceeds about  $10^{-6}$  cm<sup>2</sup>/sec in the temperature ranges where embrittlement is observed.<sup>47</sup>

The processes occurring during hydrogen entry from the gas phase<sup>50</sup> consist of (a) physisorption of H<sub>2</sub>, (b) molecular chemisorption, (c) dissociation of H<sub>2</sub>, and (d) entry of H into the lattice. These processes are illustrated in Figure 6. A schematic description of overall hydrogen processes<sup>51</sup> is presented in Figure 7.

It has been pointed out<sup>52</sup> that HE requires the development of a critical hydrogen concentration at the stress concentration sites and that a uniform distribution of hydrogen solute below this critical concentration will not cause embrittlement.

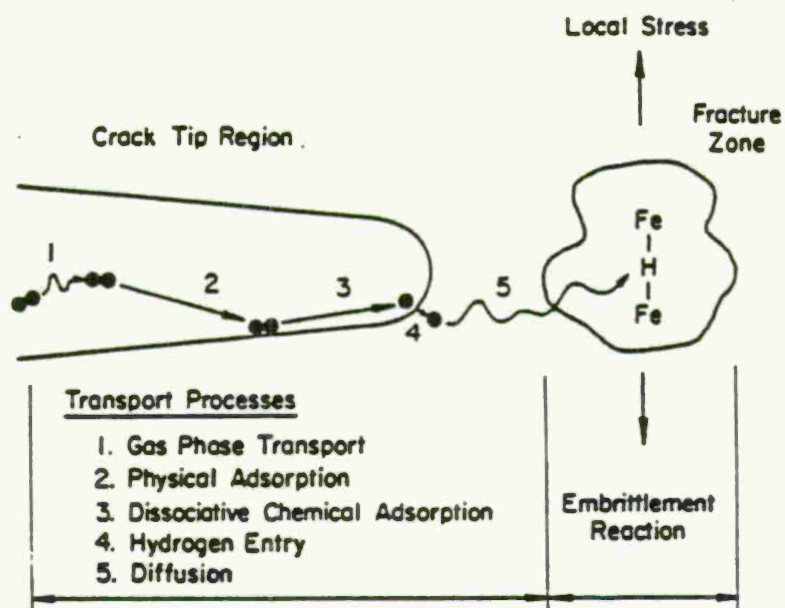


Figure 6 Schematic Illustration of Various Sequential Processes Involved in Embrittlement of Ferrous Alloys by External Hydrogen.

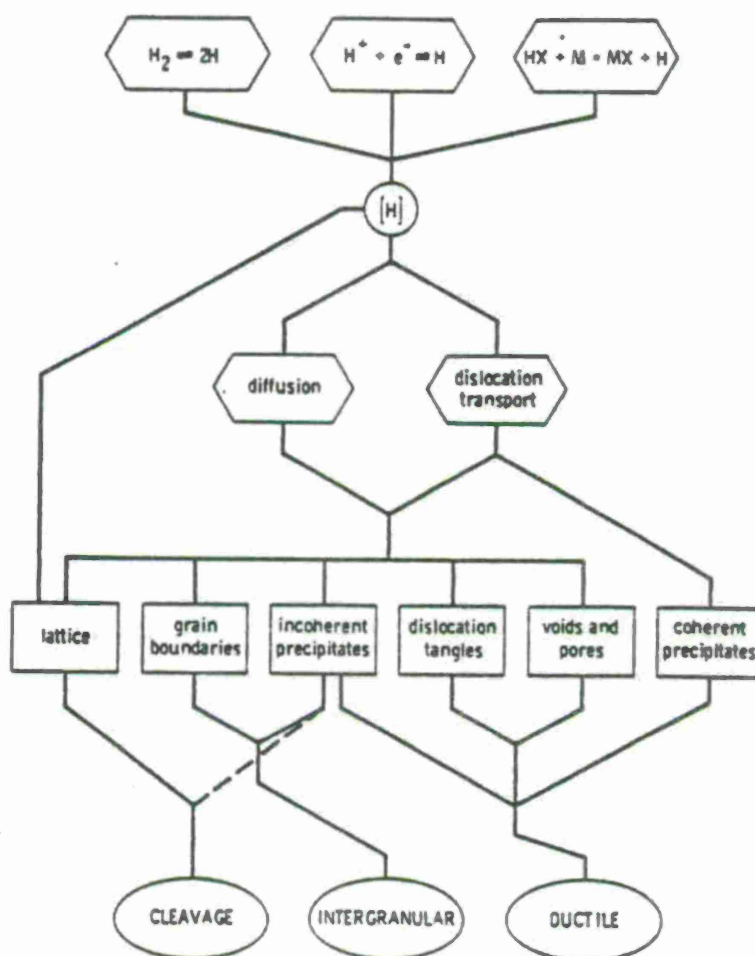


Figure 7 Summary of Hydrogen Processes: Sources Leading to Hydrogen in Solution, Transport Leading to Accumulation at Microstructural Locations, and Finally Fracture. Dashed Line Refers to Cleavage of Hydrides. From Thompson and Bernstein.<sup>51</sup>



### 2.3.1 HE Mechanisms

2.3.1.1 The Decohesion Model. The basic concept of this model is that brittle fracture occurs when the local stress exceeds the atomic bond strength and that the presence of hydrogen as a solute decreases the atomic bond strength. Hydrogen is accumulated at regions of elevated triaxial stress, according to the thermodynamics of stressed solids.<sup>53</sup> The attainment of sufficiently large local hydrogen concentration at or near a crack tip can affect the bond strength.

2.3.1.2 The Adsorption Model. Petch<sup>38</sup> proposed that adsorption of hydrogen at surfaces reduce the surface energy required to create a crack, and in the spirit of the Griffith analysis, facilitates crack propagation. As Oriani<sup>54</sup> has pointed out, this model and decohesion model are closely linked to each other. In the Petch's adsorption mechanism attention is focussed on the effects of hydrogen on the surface energy of surfaces produced by an advancing crack while the decohesion model discusses the effects on the atomic bond energy at the crack tip.

2.3.1.3 The High Pressure Bubble Formation Model. HE mechanisms based on the formation of high pressure bubbles have been proposed by Zappfe.<sup>55</sup> The basic concept is that hydrogen accumulates in internal

voids and cracks, and the resulting high gas pressure bubbles exerts an internal stress to assist fracture. The bubbles which form can often attain internal pressure of the order of  $10^5$  atmospheres.

In these mechanisms the driving force for crack propagation is the internal pressure of the bubble or the external stress and the internal pressure. While the internal pressure in the bubble provides an initial driving force for crack propagation, this would decrease rapidly in the absence of a continuous source of high fugacity hydrogen. The observation that fracture often occurs under conditions where such a decrease in bubble pressure must occur as the crack propagates, such as embrittlement by solute hydrogen, suggests that the pressurized bubble theory is not sufficient to account for the embrittlement. So, this model can be applicable to the case which has a continuous source of high fugacity hydrogen such as hydrogen charging.

2.3.1.4 The Hydrogen-Stimulated Plastic Deformation Model. Beachem<sup>56</sup> has proposed that hydrogen can induce changes in dislocation mobility, in particular a reduction in the local stress needed for dislocation motion. As has been discussed by Hirth and Johnson,<sup>57</sup> this could result in a lower stress intensity for crack propagation if growth occurs by contained plastic flow

with a plastic zone size fixed by inclusion spacings.

**2.3.1.5 The Hydride Formation Model.** Many metals which exhibit severe HE are known to form hydrides. In some systems, such as Group Vb metals and zirconium alloys, precipitated hydrides have been shown to nucleate cracks. In other systems such as nickel and aluminum alloys, hydrides are known to form but only at much higher hydrogen fugacity than is thought to occur during HE.

A qualitative mechanism for the stress induced hydride embrittlement was proposed by Westlake.<sup>58</sup> The mechanism is shown schematically in Figure 8. Application of a tensile stress decreases the hydrogen solute chemical potential at stress concentrators and results in a flux of hydrogen to the region. The hydrogen concentration increases until the stress-induced chemical potential gradient is removed. However, the stress also decreases the free energy of the hydride and hydride precipitation occurs. The kinetics of this process are controlled by the flux of hydrogen to the stress concentration sites. Once the brittle hydride forms, it cleaves, the crack runs to the hydride-matrix interface at which point it is blunted by deformation in the ductile matrix. The process propagates by repeated stress-induced hydride formation and cleavage.

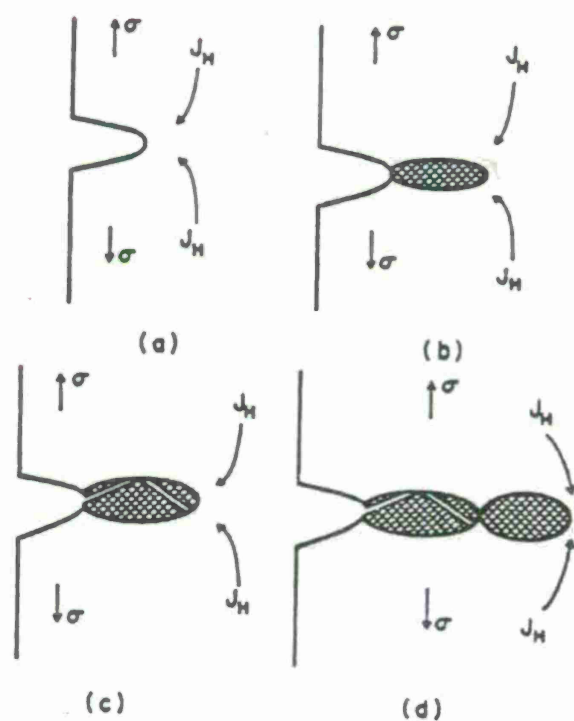


Figure 8 Schematic Showing the Mechanism of Hydride Embrittlement by Stress Induced Hydride Formation. (a) Flux of Hydrogen to the Crack Tip Due to the Reduction of the Hydrogen Chemical Potential in the Tensile Stress Field. (b) Formation of the Hydride Due to the Reduction of the Hydride Chemical Potential by the Applied Stress. (c) Cleavage of the Hydride Along Its Cleavage Plane Resulting in Crack Advance.<sup>58</sup>



### 2.3.2 Fracture Morphology

Hydrogen-induced fracture is usually thought of as brittle, and intergranular fractures are in fact common; but many materials exhibit ductile fracture in the presence of hydrogen. Cleavage can also occur, either in the matrix or through a precipitated hydride phase.

In systems which exhibit ductile failure,<sup>59</sup> the fracture morphology is unaffected by hydrogen except to a secondary degree such as changes in the size of dimples or microvoids which characterize the fracture surface.<sup>60,61</sup>

In systems which form stable hydrides, the failure mode in the absence of hydrogen is ductile, whereas when hydrogen is added as a solute a cleavage failure mode occurs.<sup>62</sup>

In non-hydride forming systems such as nickel and iron alloys the hydrogen induced brittle fracture generally occurs intergranularly.

### 2.3.3 HE of Tungsten

The group VIa b.c.c. alloys (based on molybdenum or tungsten) have generally been considered to be unaffected by hydrogen. These systems have no stable hydrides, a very low hydrogen solubility and a positive heat of solution in equilibrium with the gas phase.

In tungsten-hydrogen system,<sup>63</sup> where the hydrogen

diffusivity is relatively low at room temperature, embrittlement is observed only if the hydrogen is delivered directly to the crack tip as in simultaneous cathodic charging and tensile testing.

## PART 3

### EXPERIMENTAL PROCEDURE

#### 3.1 Materials

The materials used in this study were 90%W-Ni-Fe alloy (W-10) and 97%W-Ni-Fe-Cu-Co alloy (W-3). The alloys were prepared from powders by isostatic pressing and then sintering in dry hydrogen atmosphere. Sintering temperature was 1450°C for the W-10 alloy and 1540°C for the W-3 alloy. The W-10 alloy was heat treated at 1090°C in vacuum after sintering and cold-swaged by 24% reduction in area. The W-3 alloy was cold-swaged by 15% reduction in area without post-sintering heat treatment. The alloys were manufactured by Kennametal Inc. and supplied in the form of cylindrical rod. Their chemical compositions are listed in Table 1.

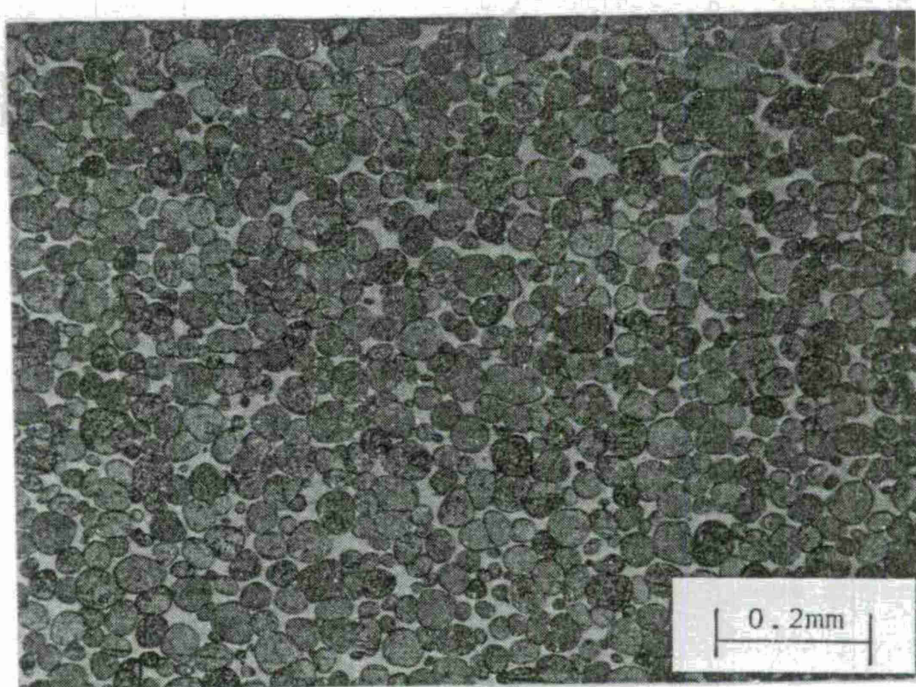
The appearances of both alloys under the light microscope are shown in Figure 9. Etching was carried out with Murakami's reagent,<sup>64</sup> which is composed of 10g of  $K_3Fe(CN)_6$ , 10g of KOH, and 100 ml of  $H_2O$ . The average grain diameters of the W-10 and W-3 alloys are 40  $\mu m$  and 110  $\mu m$ , respectively. Different sintering conditions could make that big difference in the grain size. It is well known that initial powder size does not affect the final grain size in the sintering of tungsten heavy alloy systems.

Table 1  
Chemical Compositions of the Alloys

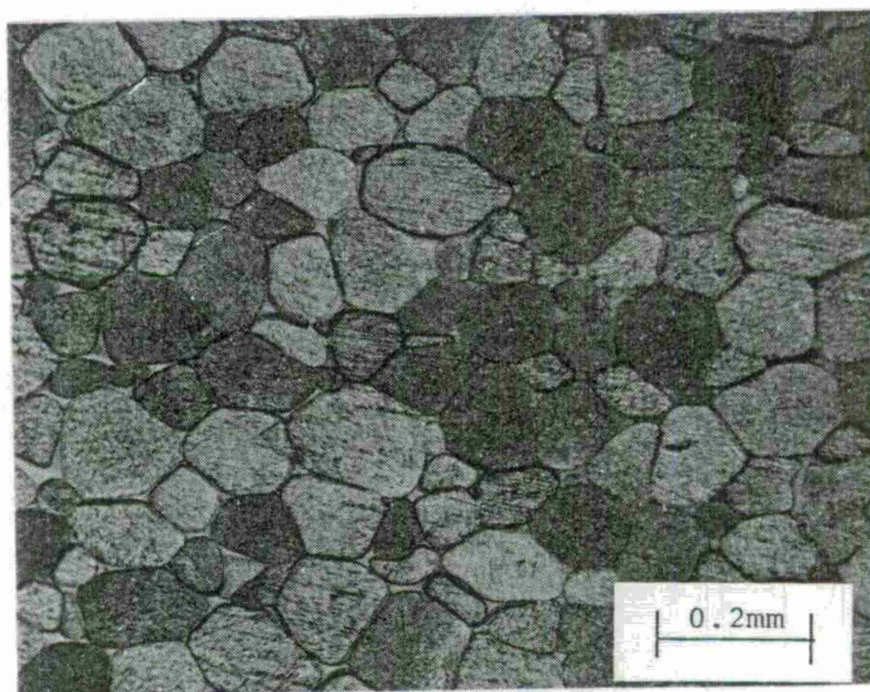
(unit: wt. %)

Elements	The W-10 Alloy	The W-3 Alloy
Ni	6.08	1.35
Fe	2.87	0.63
Cu	--	0.46
Co	--	0.09
W	Balance	Balance





(a)



(b)

Figure 9    Optical Micrographs of (a) the W-10 Alloy  
and (b) the W-3 Alloy.

### 3.2 Tension Tests

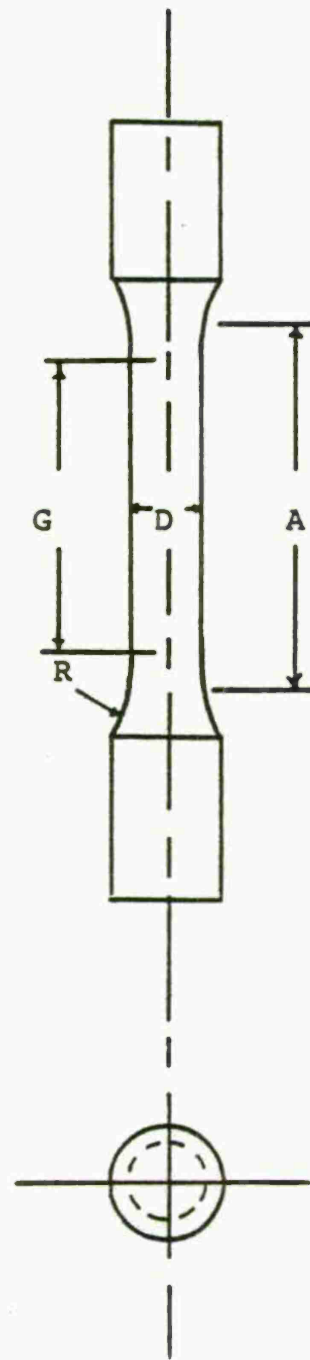
Tension tests were conducted with an Instron machine at the cross head speed of 0.05 in/min. The geometry of the tension specimen is given in Figure 10.

Yield strength, ultimate tensile strength, elongation, and Young's modulus were obtained and listed in Table 2. Young's modulus was measured by attaching strain gages to the specimen. The wide range in mechanical properties is caused primarily by non-uniform pore distribution. Many previous investigators<sup>2,5</sup> have experienced the poor reproducibility of mechanical properties. Superior strength and ductility of the W-10 alloy may result from more severe cold working, finer grain, and larger matrix area.

Results of the macro and micro hardness tests are also presented in Table 2. Macro hardness testing was conducted with Rockwell hardness tester, and micro hardness testing was conducted with Vickers micro hardness tester.

### 3.3 SCC Tests

Most of the SCC tests were conducted on modified WOL type compact toughness specimens. The specimens were machined from the rod such that the plane of the machined notch was parallel to the swaging direction and perpendicular to the axis of the cylindrical rod.



Dimensions:

A: 0.750 in.  
G: 0.640  
D: 0.160  
R: 0.156

Figure 10 Tensile Specimen Geometry.

**Table 2**  
**Mechanical and Physical Properties of the Alloys**

Properties	The W-10 Alloy	The W-3 Alloy
Yield Strength, (0.2%), MPa	1137-1247 av. 1185	503-792 av. 696
Ultimate Tensile Strength, MPa	1178-1281 av. 1261	758-1151 av. 1020
Elongation, %	2.1-8.7 av. 4.6	0.7-5.4 av. 2.1
Young's Modulus, $10^4$ MPa	34.5-37.6 av. 37.0	34.2-41.2 av. 38.2
Hardness, $R_C$	41-42	40-41
Microhardness in the W grain, KHN	558	495
Microhardness in the matrix, KHN	466	371

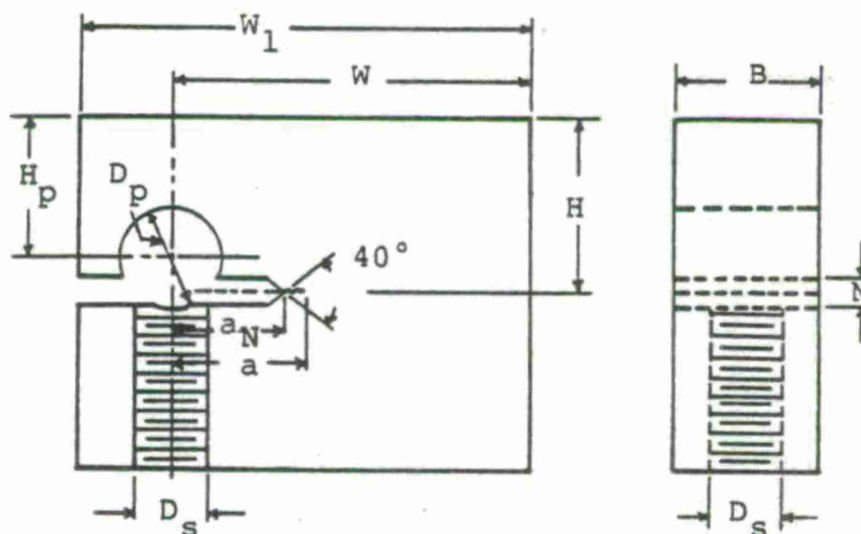


The specimen geometry is shown in Figure 11. Following machining, the specimens were mechanically ground on 240 through 600 grit SiC papers. After grinding, specimens were thoroughly cleaned in acetone.

Prior to the environmental testing, all specimens were fatigue precracked in air approximately 1.0 mm beyond the notch tip. Fatigue precracking was performed at 30 Hz with a Satec Model SF-10 fatigue machine in the tension-tension mode. This fatigue machine is an inertial, rotating mass machine which provides a constant cyclic force.

The  $K_{ISCC}$  tests were conducted under constant COD loading conditions. COD value was measured using the NASA type clip gage.<sup>65</sup> The constant COD tests were performed in accordance with the techniques described by Novak and Rolfe.<sup>25</sup> In a modified WOL specimen, load can be applied by the use of a bolt and loading tup. The bolt and loading tup were machined from steel heat treated to a high strength to prevent plastic flow in the bolt at high stress levels.

The environments used were an aerated 3% NaCl solution and the NACE recommended sulfide cracking solution<sup>66</sup> containing 5% NaCl and 0.5% acetic acid, saturated with hydrogen sulfide gas. Saturation was maintained throughout the tests by bubbling the gas through the solution. Some tests also were carried out in a 10% sulfuric acid solution.



Dimensions:

$B = 1.00 \text{ cm} = 0.394 \text{ in.}$   
 $W = 2.47 \text{ cm} = 0.973 \text{ in.}$   
 $W_1 = 3.10 \text{ cm} = 1.221 \text{ in.}$   
 $H = 1.22 \text{ cm} = 0.479 \text{ in.}$   
 $H_p = 0.98 \text{ cm} = 0.388 \text{ in.}$   
 $a_N = 0.93 \text{ cm} = 0.366 \text{ in.}$   
 $D_s = \frac{1}{4} \times 28 \text{ through thread}$   
 $D_p = \frac{1}{4} \text{ in. drilled hole}$   
 $N = 0.24 \text{ cm} = 0.094 \text{ in.}$

Figure 11 Modified WOL Specimen.

Crack propagation was monitored under an optical microscope. Crack arrest was estimated from the stress intensity factor ( $K_I$ ) vs. crack growth rate ( $da/dt$ ) curve developed after sufficiently long SCC experiment. Figure 12 shows crack arrest line of the modified WOL specimen.

The stress intensity factor at the crack tip was calculated with the following equation:<sup>25</sup>

$$K_I = \frac{E \cdot V_o \cdot C_3 (a/W)}{\sqrt{a} \cdot C_6 (a/W)}$$

where  $a$  is the crack length,  $W$  is the width of the specimen,  $E$  is Young's modulus,  $V_o$  is the initial COD,

$$C_3(a/W) = 30.96(a/W) - 195.8(a/W)^2 + 730.6(a/W)^3 \\ - 1186.3(a/W)^4 + 754.6(a/W)^5,$$

and

$$C_6(a/W) = \exp\{4.495 - 16.130(a/W) + 63.838(a/W)^2 \\ - 89.125(a/W)^3 + 46.815(a/W)^4\}.$$

Owing to the decrease of stress intensity factor with increase of the crack length in constant COD specimens,  $K_{ISCC}$  can be measured with one specimen. However, duplicate specimens were tested.

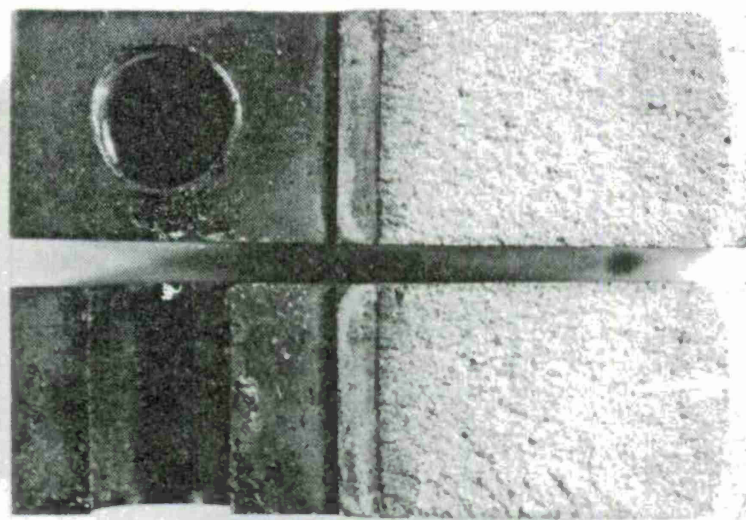


Figure 12 Modified WOL Specimen Showing Crack Arrest Line.

### 3.4 Electrochemical Tests

Electrochemical polarization tests were carried out on the basis of ASTM Standard G5-72.<sup>67</sup> In preparation for testing, samples were wet ground on all sides with 240 through 600 grit silicon carbide papers. Just prior to immersion into the test cell, each sample was wet ground on the 600 grit paper with gloved hands and cleaned in distilled water.

Potentiodynamic polarization scans were run using a Princeton Applied Research Model 173 potentiostat/galvanostat. Prior to polarization, the sample was placed in a corrosion cell and allowed to freely corrode. After reaching a stable state, the open-circuit potential was measured using a saturated calomel electrode. Generally, it took 20 to 30 minutes to stabilize. Samples were then polarized either anodically or cathodically at a sweep rate of 0.3 mV/sec. The tests were monitored with a Hewlett Packard 9816 computer. The data were stored and plotted using the computer. Platinum and saturated calomel were used as a counter electrode and a reference electrode, respectively.

### 3.5 Optical and Electron Microscopy

To examine the nature of the corrosion attack on the specimen surfaces, optical metallography techniques were utilized.



In an attempt to determine fracture morphology and elucidate mechanisms of environmental failure, fracture surfaces were analyzed with an AMR 1000 scanning electron microscope.

Qualitative determination of the fracture surface composition was performed with EDAX (energy dispersive analysis by X-ray).

Chemical compositions in the tungsten grain and matrix phases were determined by EPMA (electron probe microanalysis). The analyses were performed with Automated Cameca MBX microprobe at General Electric R&D Center. Operating voltage was 15 kV, and constant current of 60 nA was used for beam regulation. Characteristic lines of  $W_{M\alpha}$ ,  $Ni_{K\alpha}$ ,  $Fe_{K\alpha}$ ,  $Cu_{K\alpha}$ , and  $Co_{K\alpha}$  were employed to determine chemical compositions.

## PART 4

### RESULTS

#### 4.1 SCC Behavior

##### 4.1.1 Effects of Polarization

In addition to  $K_{ISCC}$  tests conducted at the open-circuit potential, a number of tests were carried out under conditions of applied potentiostatic polarization. Polarization curves obtained for the W-10 and W-3 alloys in aerated 3% NaCl solution are presented in Figures 13 and 14, respectively. The corrosion potentials of the W-10 and W-3 alloys are -0.340 V vs. SCE and -0.240 V vs. SCE, respectively. Both alloys appear to undergo an active-passive transition. The critical current density and current density at passivity are about 100 times greater for the W-3 alloy than for the W-10 alloy. Therefore, passivity of the W-10 alloy can be achieved more easily than the W-3 alloy, and effectiveness of the passive film is better for the W-10 alloy than the W-3 alloy. The big difference in anodic polarization curve between the two alloys may result from the different volume fraction and chemical composition of the matrix.

Polarization in the active direction favors cathodic reduction reactions. In aerated neutral solutions, the principal reaction that occurs is the oxygen reduction reaction:

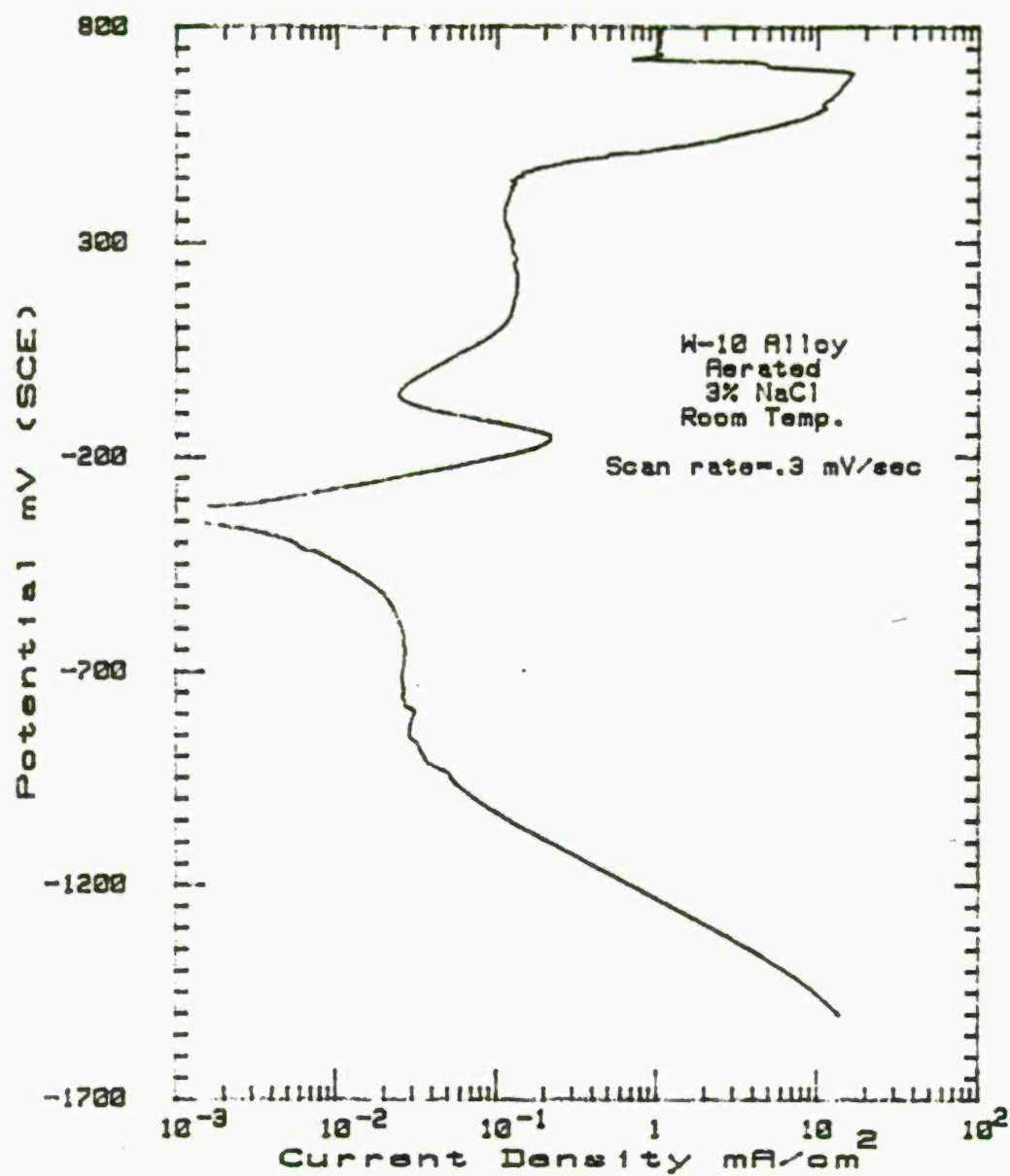


Figure 13 Polarization Curve for the W-10 Alloy in Aerated 3% NaCl Solution.

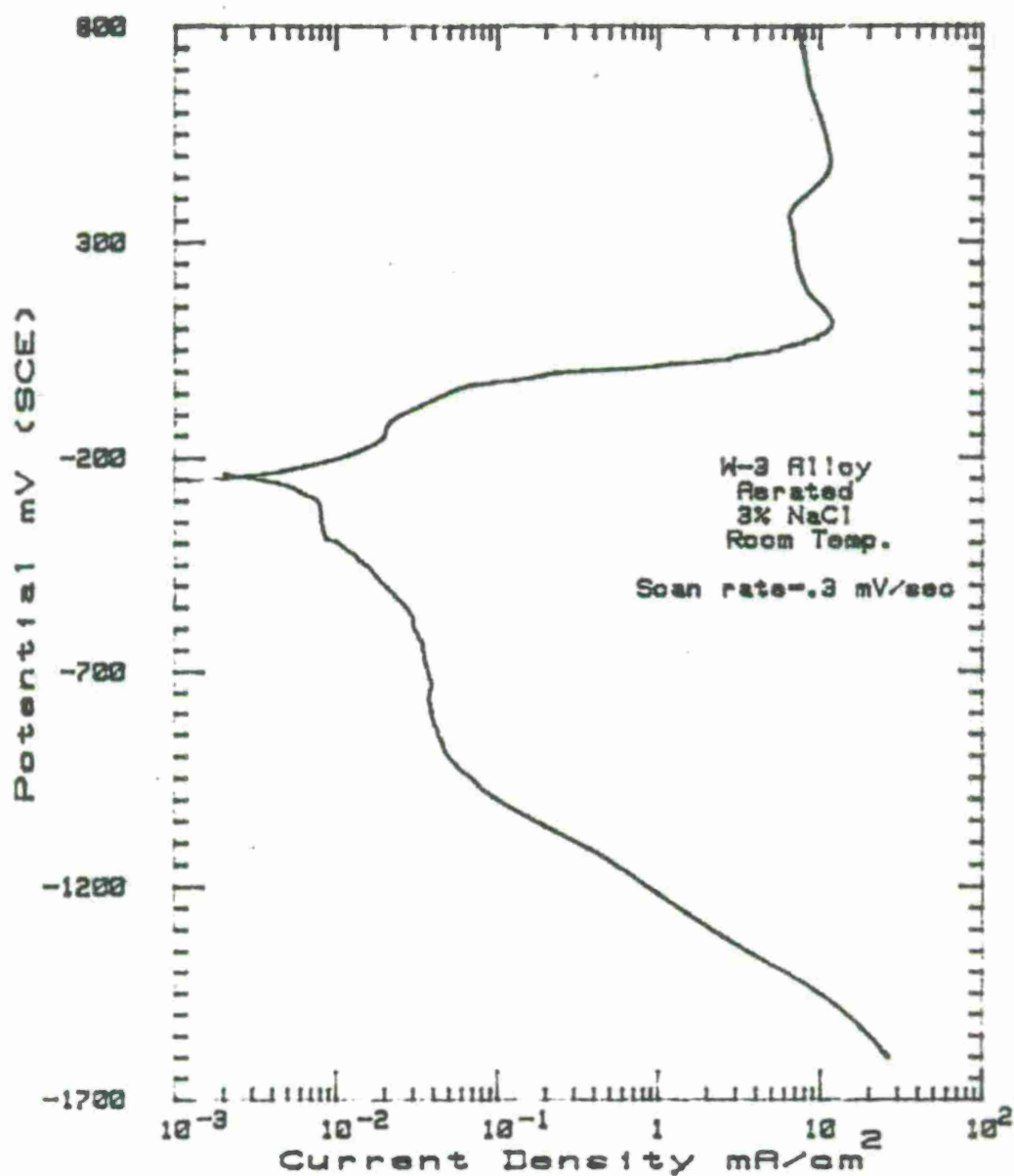


Figure 14 Polarization Curve for the W-3 Alloy in Aerated 3% NaCl Solution.



This reaction reaches its limiting current density as the oxygen content of the solution adjacent to the electrode surface becomes depleted. Once the limiting current density is reached, further cathodic polarization produces little increase in the measured current density.

At about -1.0 V vs. SCE, the hydrogen evolution reaction becomes the dominating cathodic reaction:



and



This reaction initially obeys Tafel equation:

$$\eta = \beta \log \frac{i}{i_0}$$

where  $\eta$  is hydrogen overvoltage,  $\beta$  is Tafel slope, and  $i_0$  is the exchange current density. The Tafel slope for the W-10 and W-3 alloys are -0.2 V/decade and -0.22 V/decade, respectively.

The stress intensity factor vs. crack propagation rate curve for the W-10 alloy in aerated 3% NaCl solution is shown in Figure 15. The crack growth rate in the plateau region was  $3.8 \times 10^{-8}$  m/sec and  $K_{\text{ISCC}}$  was



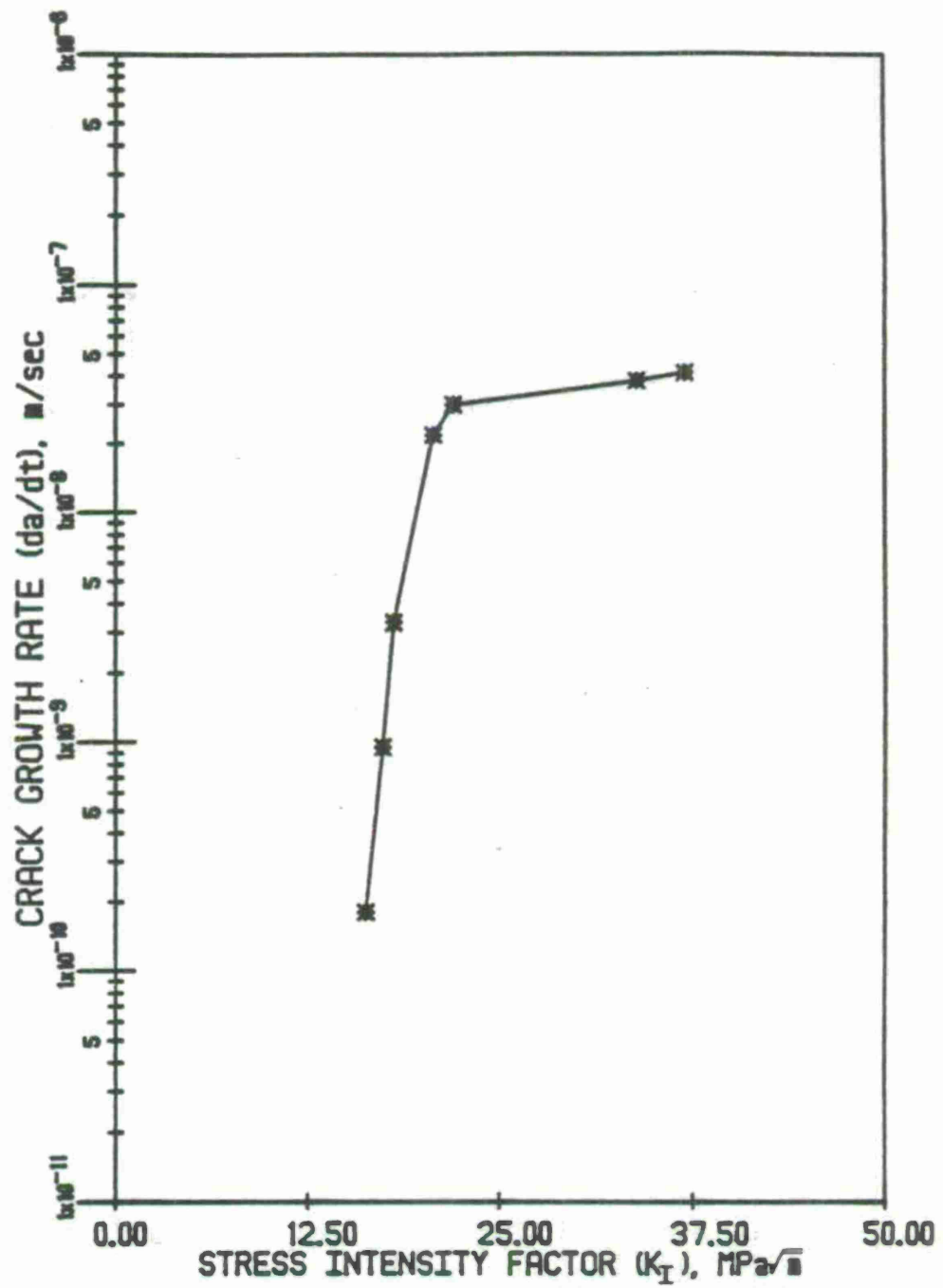


Figure 15 The SCC Behavior of the W-10 Alloy in Aerated 3% NaCl Solution.

16.3 MPa $\sqrt{m}$ .

The results of polarization effects on the  $K_{ISCC}$  and crack propagation rate of the W-10 alloy are plotted in Figure 16. Specimens were polarized at potentials in the regions of active dissolution, passive, and hydrogen evolution. When anodic potential of -0.2 V vs. SCE was applied,  $K_{ISCC}$  and the crack growth rate remain the same as for the case of the open-circuit potential.

When the specimen was polarized at an anodic potential of 0.2 V vs. SCE, the crack propagated as fast as in the case of -0.2 V vs. SCE and  $K_{ISCC}$  was remarkably lowered.

With the applied cathodic potential of -1.2 V vs. SCE, the crack growth rate in the plateau increased substantially and the  $K_{ISCC}$  was not altered.

At the open circuit potential and anodic potentials, corrosion started to occur in the plastically deformed area near the crack tip. As corrosion proceeded, the specimen surfaces were severely attacked, and the crack propagated. Optical micrograph, Figure 17, indicates that corrosion attack preferentially occurred in the matrix ahead of the crack tip, and that the crack propagated along the dissolved matrix area perpendicular to the loading direction. Slight dissolution occurred in the matrix of the sides of the crack because of a passive film on the surface.

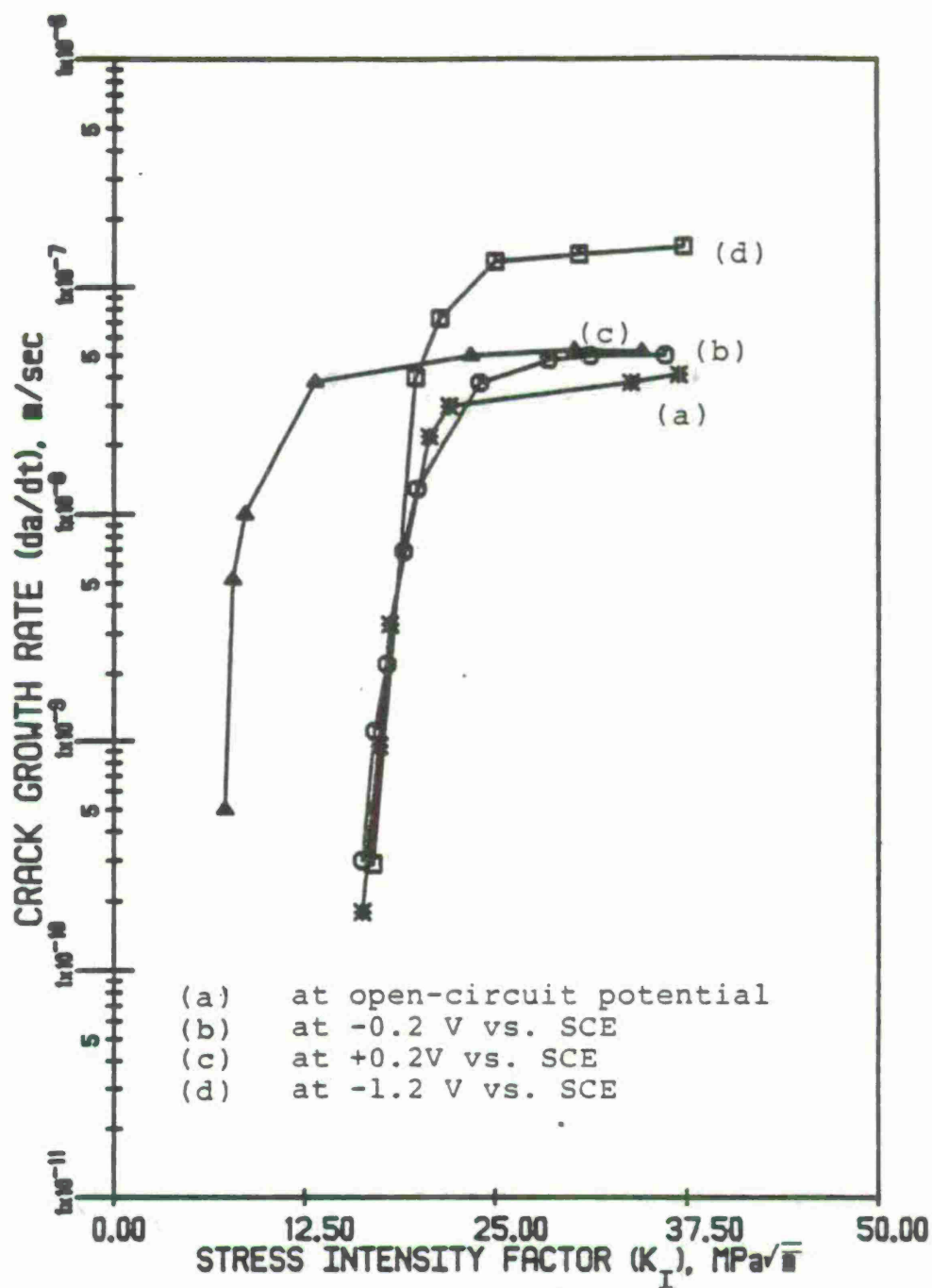


Figure 16 Polarization Effects on the  $K_{I_{SCC}}$  and Crack Growth Rate of the W-10 Alloy in 3% NaCl Solution.

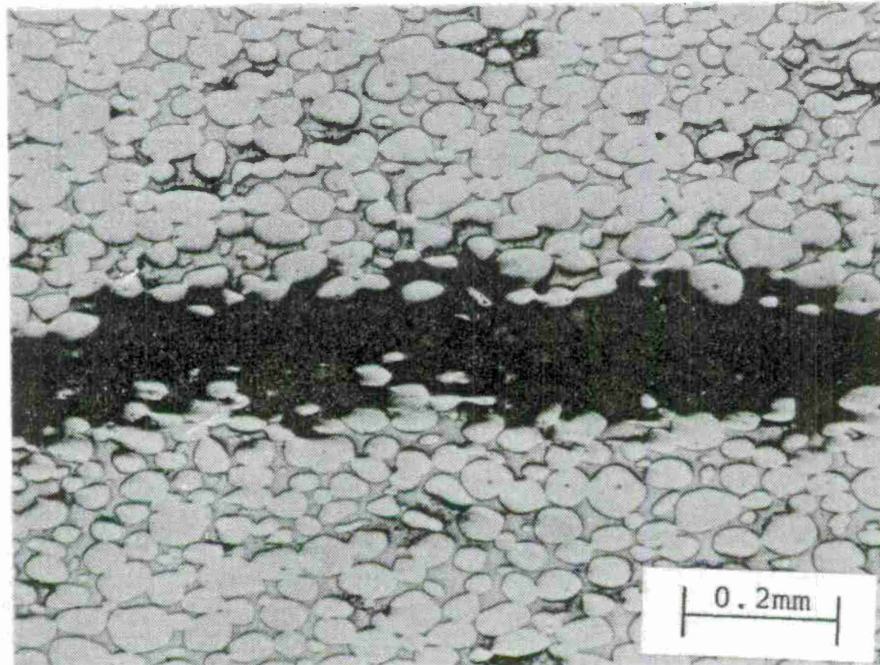


Figure 17 Optical Micrograph for the W-10 Alloy Specimen Showing Crack Propagation through the Dissolved Matrix Ahead of the Crack Tip, at 0.2 V vs. SCE in 3% NaCl Solution.





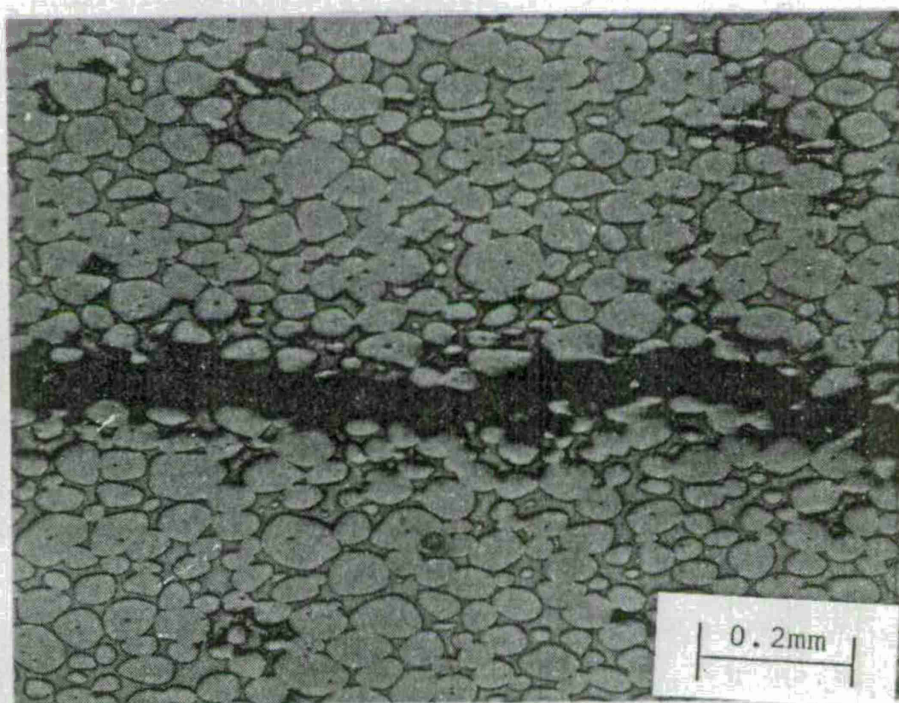


Figure 18      Optical Micrograph for the W-10 Alloy Specimen  
Showing Crack Propagation Through the Tungsten-  
Matrix and Tungsten-Tungsten Interfaces, at  
-1.2V vs. SCE in 3% NaCl Solution.

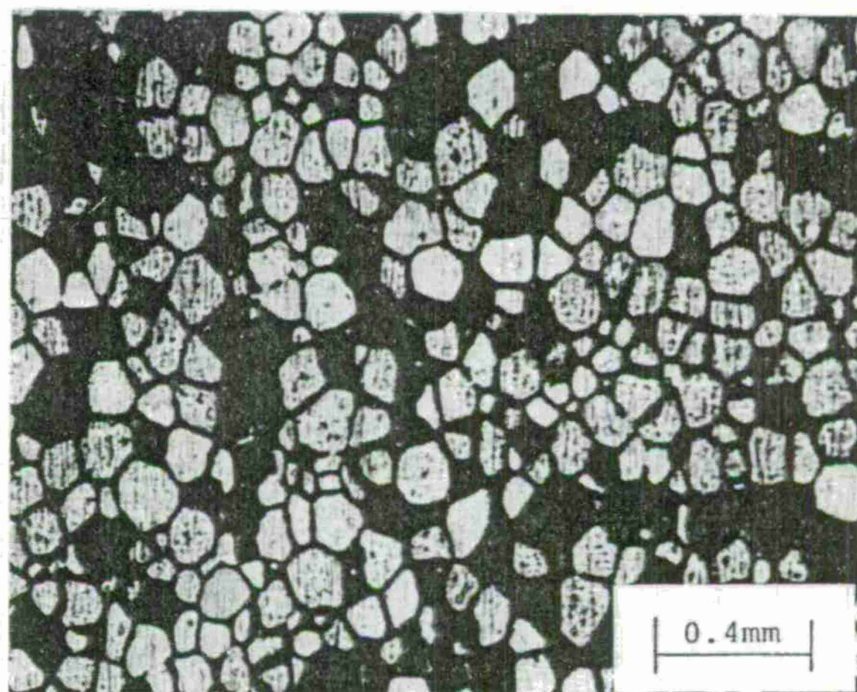


Figure 19 Specimen Surface of the W-10 Alloy Showing Severe Corrosion Attack, Especially in the Matrix Area.



because they poison the hydrogen recombination reaction on the metal surface. It is thought that these poisons retard the rate of formation of molecular hydrogen and increase the accumulation of adsorbed hydrogen atoms on the electrode surfaces. Therefore, there is an increased supply of atomic hydrogen which can interact with the specimen.

The enhanced hydrogenation effect in the presence of promoters involves the formation of stable hydrides, according to Newman and Shreir.<sup>69</sup> Having performed the experiments with high strength steel specimens over a wide range of pH, they also found that As and P are effective promoters at all pH's (their hydrides are stable over the entire pH range), whereas, S, Se, and Te are more effective in acid solutions. However, McCright and Staehle<sup>70</sup> reported that the entry of hydrogen does not depend upon arsine ( $\text{AsH}_3$ ) formation; the greatest relative permeation occurs in the potential range where arsenic is the stable phase. They also found that only when the specimen is polarized to sufficiently cathodic potentials is there noticeable entry and permeation of hydrogen.

Figures 20 and 21 present the cathodic polarization curves for the W-10 and W-3 alloys in aerated 3% NaCl solution with and without 60 ppm of arsenic, respectively. They show that the limiting current density is almost the same, and that the cathodic reaction rate is

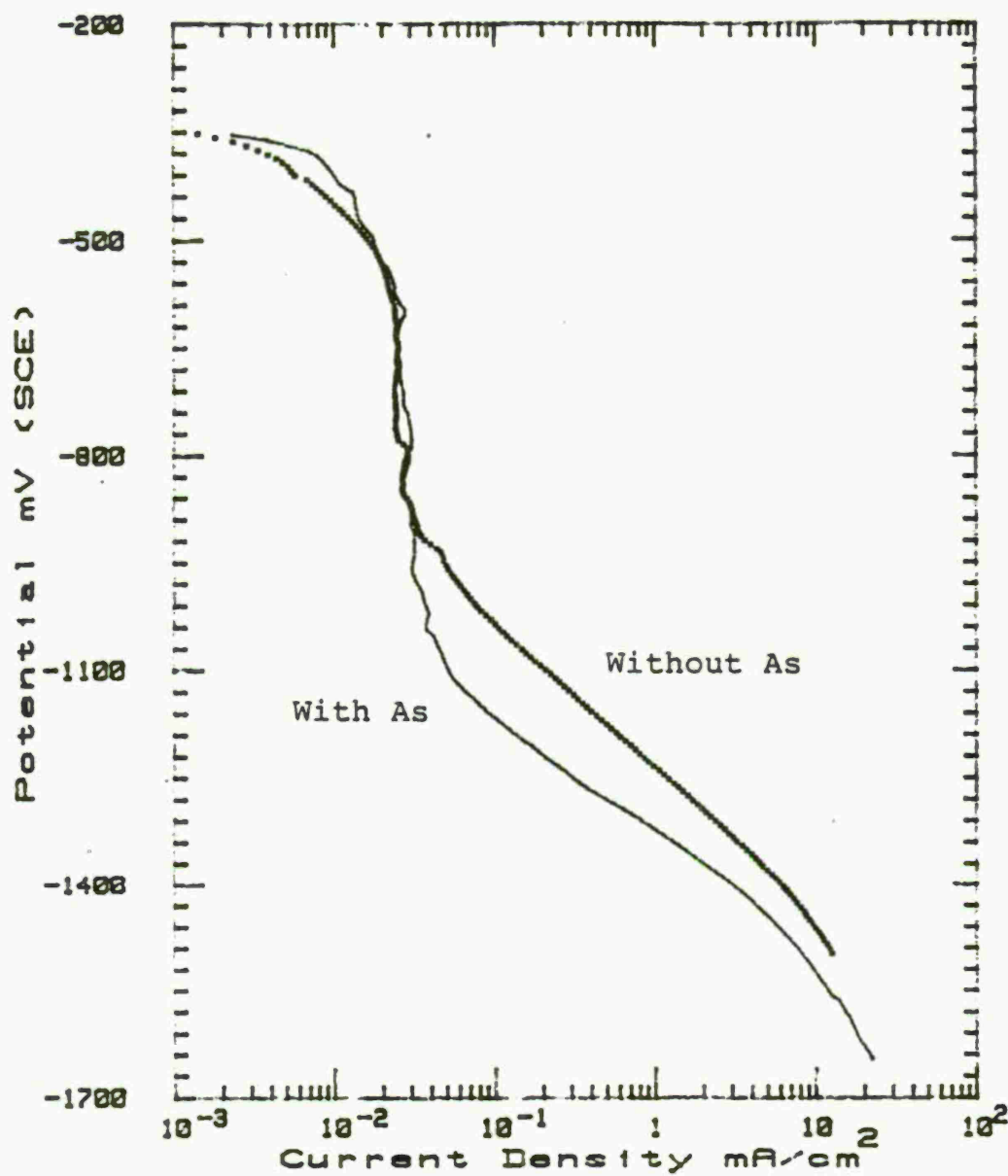


Figure 20 Effect of As Addition on the Cathodic Polarization Curves for the W-10 Alloy in Aerated 3% NaCl Solution.



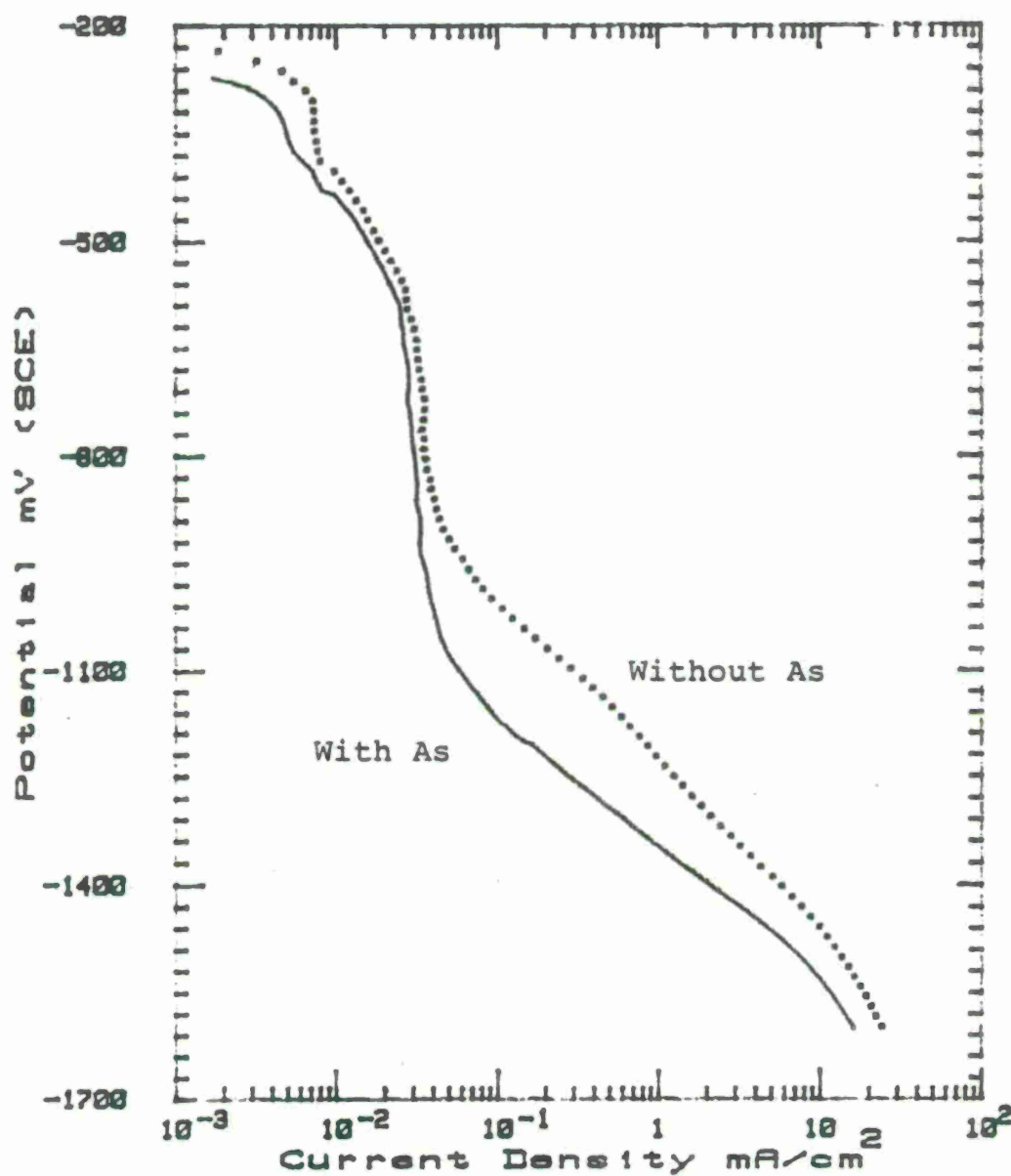


Figure 21 Effect of As Addition on the Cathodic Polarization Curves for the W-3 Alloy in Aerated 3% NaCl Solution.

inhibited over the hydrogen evolution reaction range so that additional polarization is necessary to produce a reaction rate equivalent to that observed in pure NaCl solution.

Cathodic charging at -1.2 V vs. SCE was performed on the specimen in the NaCl solution containing 60 ppm of As. Figure 22 shows the  $K_I$  vs.  $da/dt$  curves for the W-10 alloy at -1.2 V vs. SCE in the NaCl solution containing 60 ppm of As. When compared to the test results from the pure NaCl solution,  $K_{ISCC}$  was decreased and the crack growth rate in the plateau region was almost the same.

Cathodic chargings at -0.8 V, -1.0 V, -1.2 V, -1.4 V, and -1.6 V vs. SCE in the NaCl solution containing As did not result in crack propagation in the W-3 specimens.

In order to study the effectiveness of As in an acidic solution, cathodic charging was conducted at -1.2 V vs. SCE in 10% sulfuric acid solution containing 60 ppm of As. Figure 23 shows the  $K_I$  vs.  $da/dt$  curve for the W-10 alloy. When compared to the cathodically charged case in the NaCl solution containing 60 ppm of As, the  $K_{ISCC}$  was decreased and the crack growth rate in the plateau region was almost the same.

When the W-3 alloy was cathodically charged in 10% sulfuric acid solution containing 60 ppm of As, it showed the crack propagation.  $K_{ISCC}$  is  $33.7 \text{ MPa}\sqrt{\text{m}}$

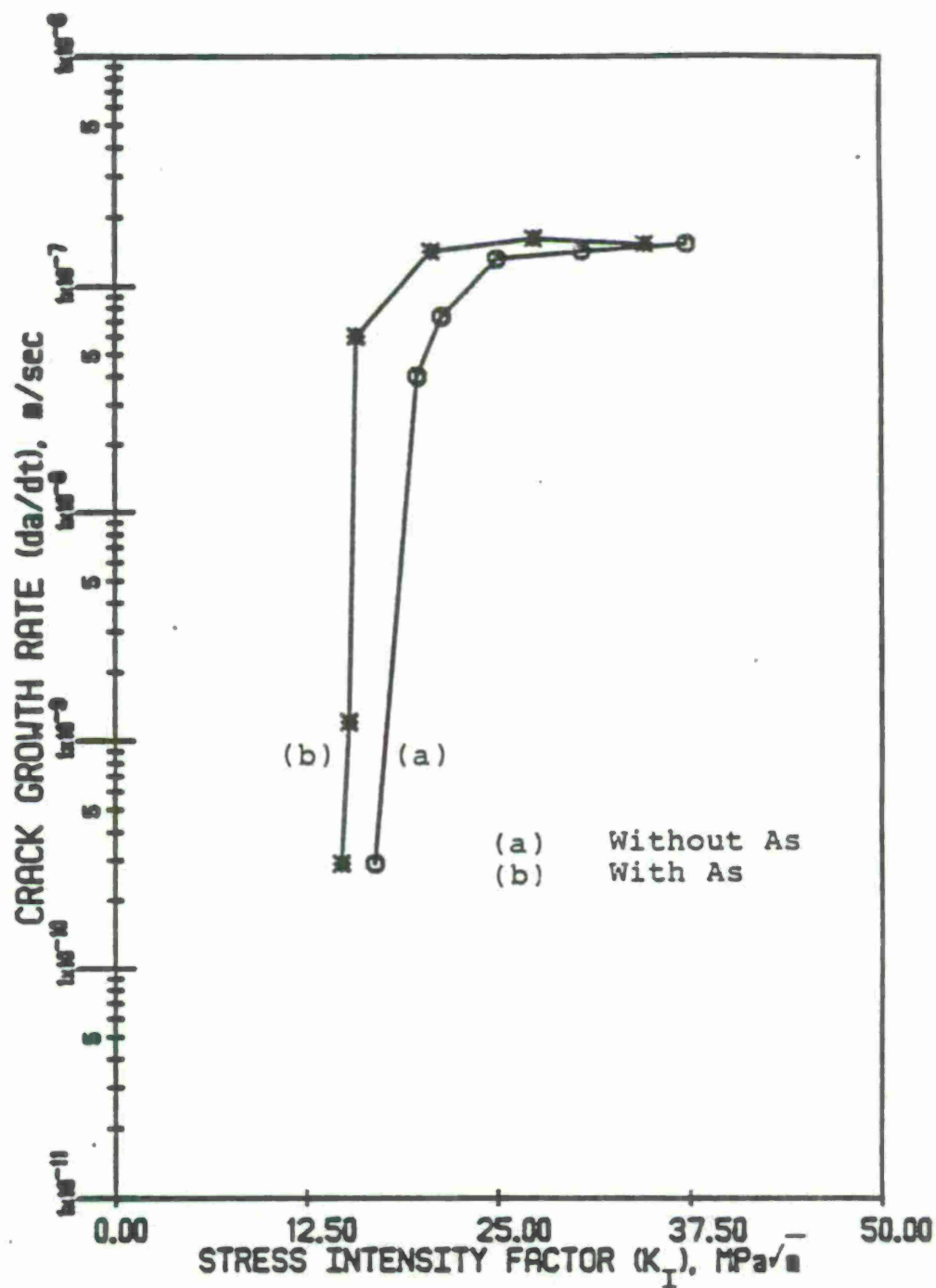


Figure 22 Influence of a Hydrogen Catalyst (As) on The  $K_{ISCC}$  and Crack Growth Rate of the W-10 Alloy at -1.2 V vs. SCE in NaCl Solution.

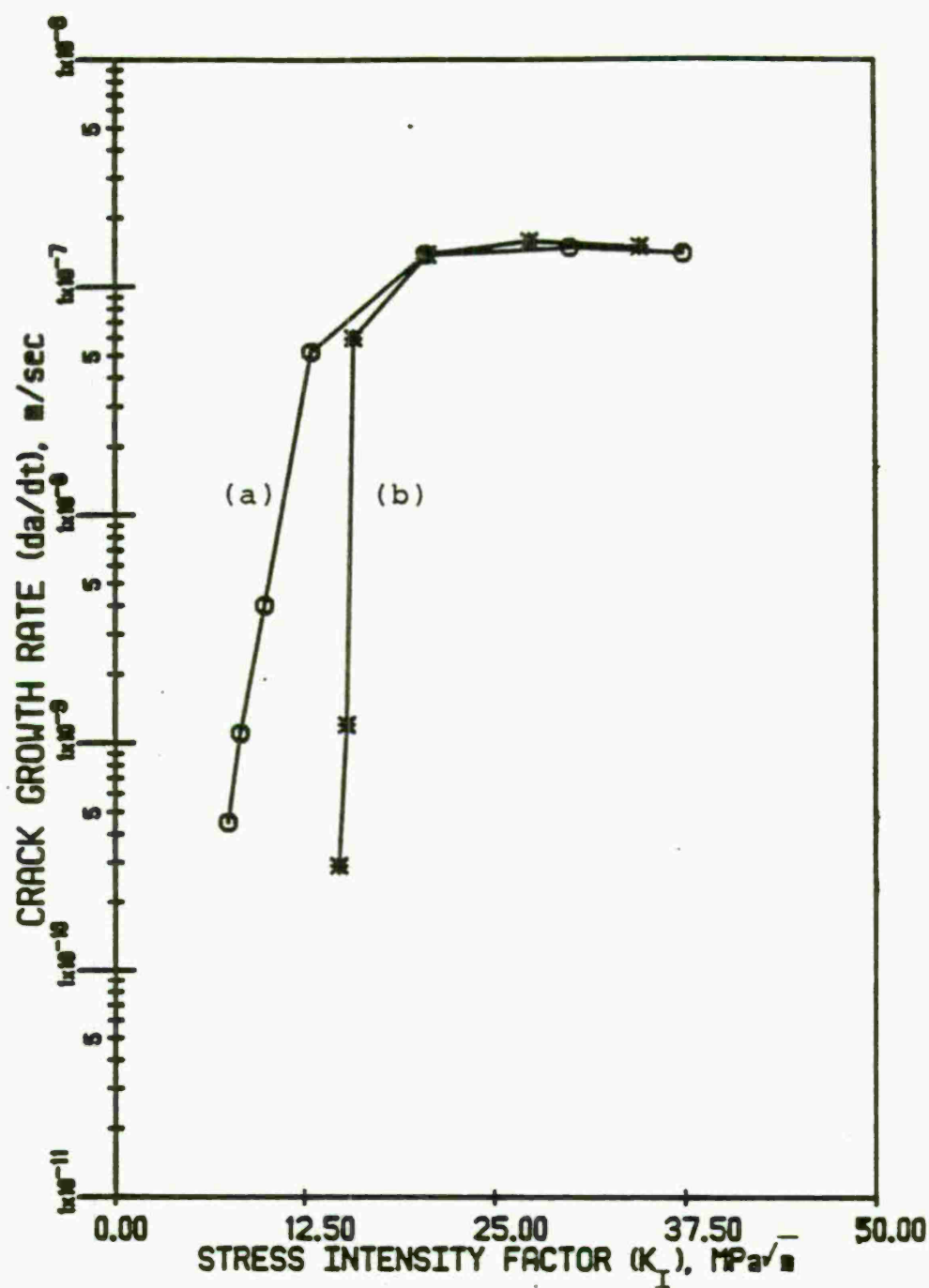


Figure 23 The Stress Intensity Factor vs. Crack Growth Rate Curve for the W-10 Alloy at  $-1.2$  V vs. SCE: (a) in 10%  $\text{H}_2\text{SO}_4$  Solution Containing 60 ppm of As, (b) in 3% NaCl Solution Containing 60 ppm of As.

and the crack growth rate in the plateau region is  $3.7 \times 10^{-9}$  m/sec as shown in Figure 24.

#### 4.1.3 Effects of Heat Treatment

It is well known that the chemical composition of the matrix plays an important role in determining mechanical and chemical properties of tungsten heavy alloys. It could be changed with different sintering and post-sintering heat treatment conditions. Minakova et al.<sup>71</sup> found that both decreasing the rate of cooling from the sintering temperature and annealing after quenching lower the tungsten content in the matrix.

EPMA data giving chemical composition in the matrix and tungsten grain phases of the W-10 and W-3 alloys are presented in Table 3 and 4, respectively.

Heat treatment was performed to study the influence of the matrix phase composition on the SCC behavior. Specimens were water-quenched after heat treating at 1100°C in argon atmosphere for 1 hr and 16 hrs. As shown in Figure 25, heat treatment did not change the microstructure and size of the tungsten grains very much. The resulting chemical composition of the phases are reported in Tables 3 and 4. In the case of W-10 alloy, the variations of chemical composition with the heat treatment were negligible when the accuracy of the EMPA was considered. The results are not surprising because the as-received material is



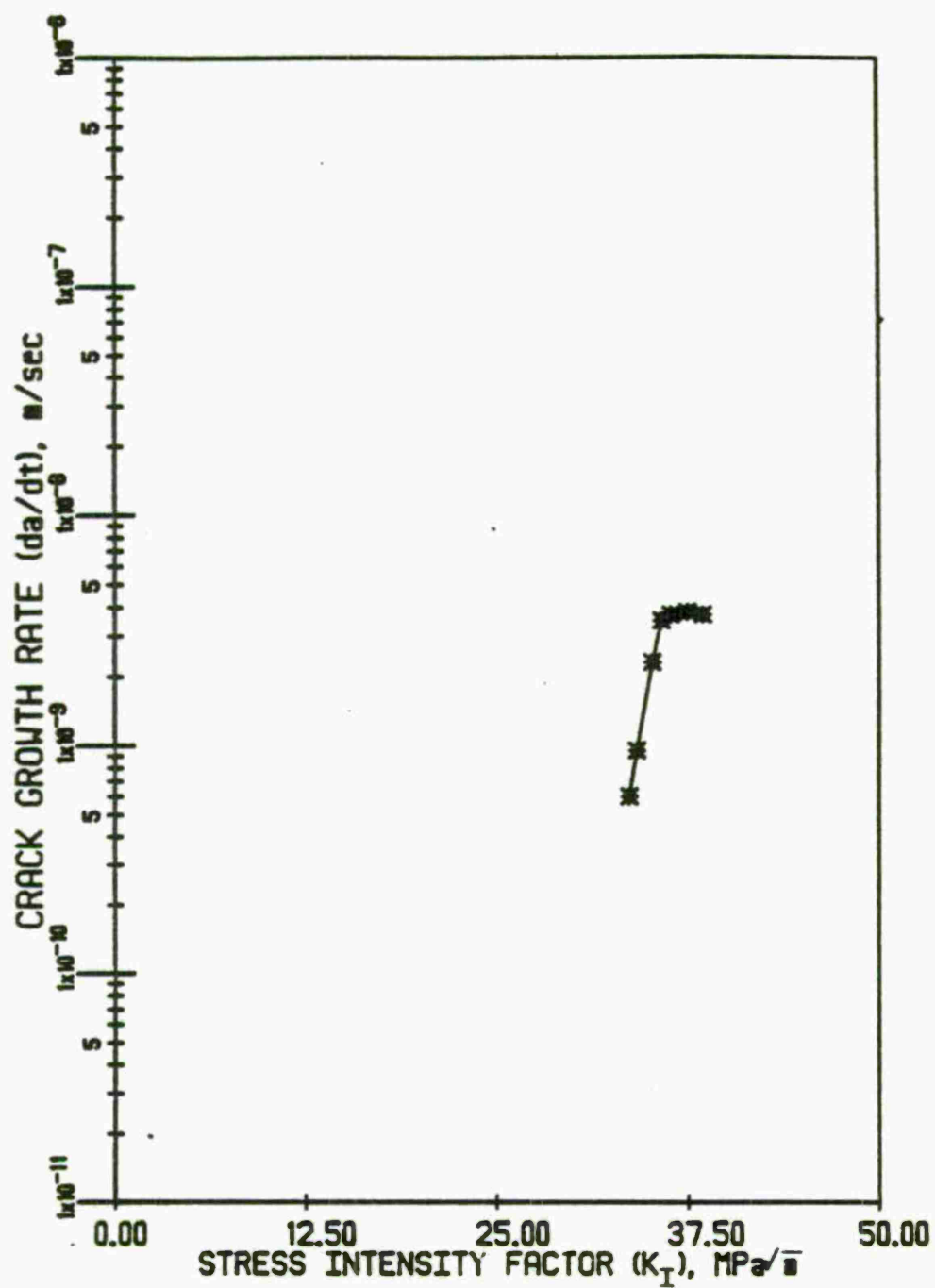


Figure 24 SCC Behavior of the W-3 Alloy at -1.2 V vs. SCE in 10%  $\text{H}_2\text{SO}_4$  Containing 60 ppm of As.

**Table 3**  
**Compositions of the W-10 Alloy Phases**

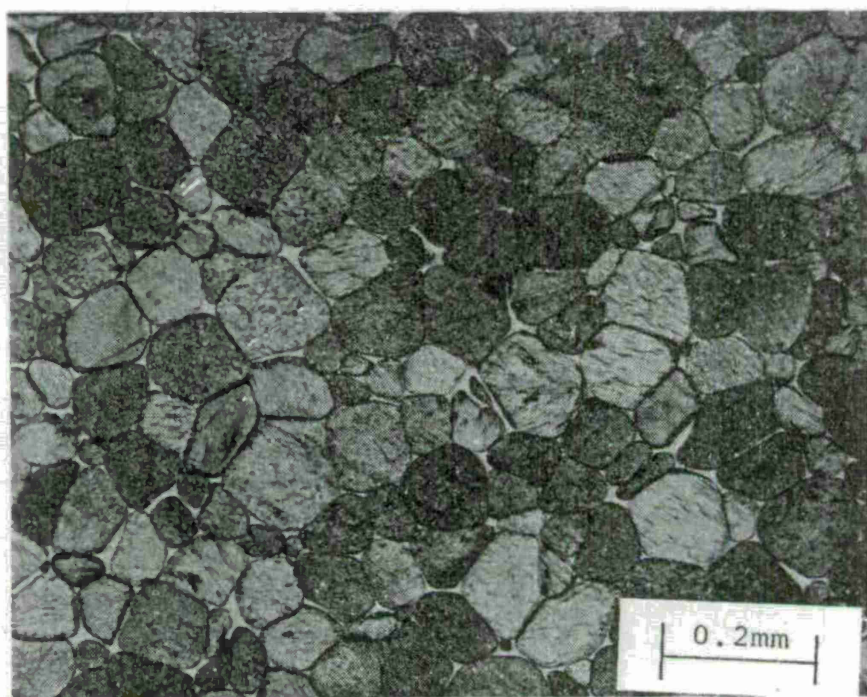
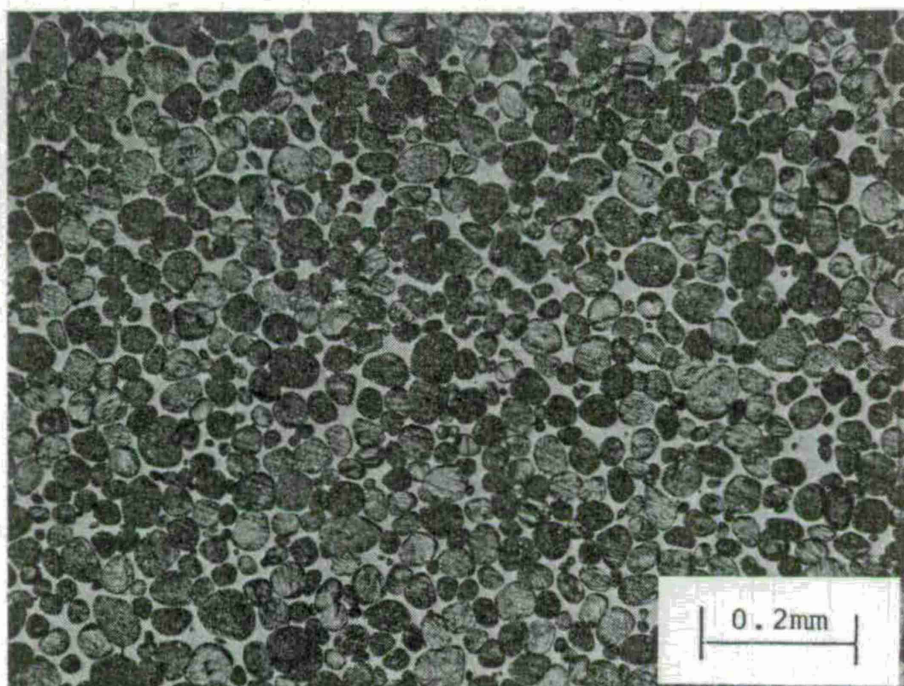
(unit: wt.%)

Conditions	Tungsten Phase		Matrix Phase	
As-received	Ni	0.00	Ni	53.67
	Fe	0.21	Fe	24.30
	W	99.79	W	22.03
Heat treated at 1100°C for 1 hr	Ni	0.00	Ni	52.88
	Fe	0.18	Fe	25.12
	W	99.82	W	22.01
Heat treated at 1100°C for 16 hrs	Ni	0.00	Ni	56.62
	Fe	0.20	Fe	23.33
	W	99.80	W	20.05

**Table 4**  
**Compositions of the W-3 Alloy Phases**

(unit: wt.%)

Conditions	Tungsten Phase		Matrix Phase	
As-received	Ni	0.00	Ni	47.88
	Fe	0.20	Fe	19.78
	W	99.67	W	8.86
	Cu	0.08	Cu	20.37
	Co	0.05	Co	3.11
Heat treated at 1100°C for 1 hr	Ni	0.00	Ni	51.72
	Fe	0.18	Fe	22.94
	W	99.75	W	14.47
	Cu	0.04	Cu	7.19
	Co	0.03	Co	3.68
Heat treated at 1100°C for 16 hrs.	Ni	0.00	Ni	48.91
	Fe	0.20	Fe	20.74
	W	99.66	W	13.32
	Cu	0.09	Cu	13.57
	Co	0.05	Co	3.56



(b)

Figure 25    Optical Micrographs Showing Microstructure of  
the Heat-Treated (a) W-10 Alloy and (b) W-3 Alloy.



already heat treated once after sintering.

In the case of the W-3 alloy, there are significant differences in the chemical composition in the matrix phase between the as-received and heat treated samples. Tungsten content in the matrix phase increased with 1 hr heat treatment. 16 hrs heat treatment did not make further increase tungsten content in the matrix phase.

The  $K_{ISCC}$  tests were conducted on the heat treated specimens in aerated 3% NaCl solution. The results for the W-10 alloy are plotted in Figure 26. No remarkable differences exist between the as-received and heat treated specimens. At the open circuit potential,  $K_{ISCC}$  was 16.0 MPa $\sqrt{m}$  and the crack growth rate in the plateau was  $4.0 \times 10^{-8}$  m/sec. In the case of W-3 alloy, there was not SCC propagation at open-circuit, anodic, and cathodic potentials.

In order to study the effects of internal hydrogen on the SCC behaviors, heat treatment was performed at 1100°C in hydrogen atmosphere for 1 hr. According to Powell,<sup>72</sup> the diffusivity of hydrogen in 95 W-3.5 Ni-1.5 Fe alloy follows the following equation:

$$D = 0.0057 \exp (-10.8 \text{ kcal/RT}).$$

So, 1 hr is enough time for hydrogen to penetrate the specimen.

The  $K_{ISCC}$  tests with the heat treated W-10 alloy

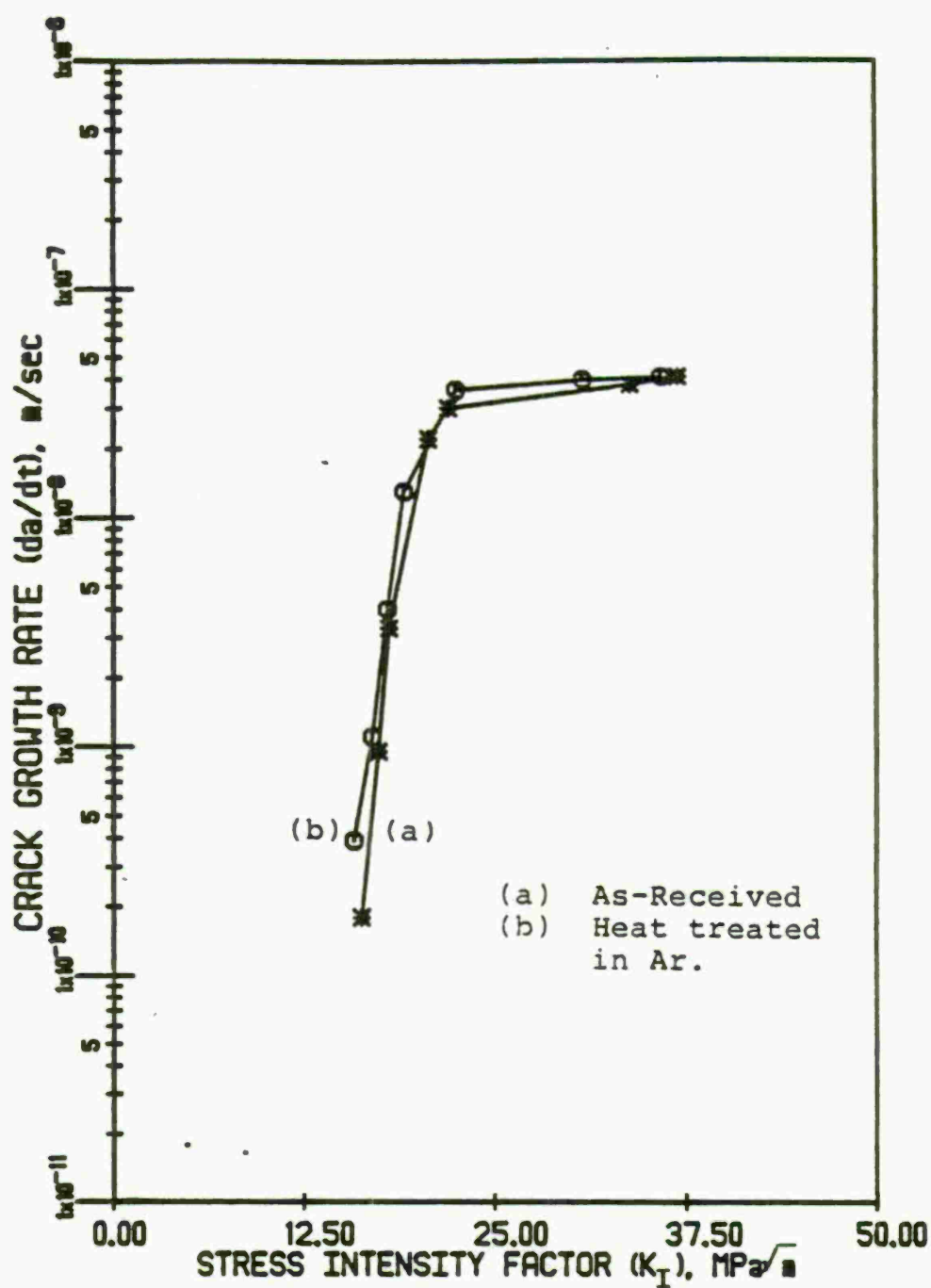


Figure 26 Influence of Heat Treatment in Argon Atmosphere on the SCC Behavior of the W-10 Alloy in NaCl Solution. No Remarkable Differences Exist Between the As-Received and the Heat Treated Specimens.

show remarkable changes in  $K_{ISCC}$  and crack growth rate as presented in Figure 27. At corrosion potential,  $K_{ISCC}$  was  $12.6 \text{ MPa}\sqrt{\text{m}}$  and the crack growth rate in the plateau was  $1.3 \times 10^{-7} \text{ m/sec}$ . At  $-1.2 \text{ V vs. SCE}$ ,  $K_{ISCC}$  was  $4.5 \text{ MPa}\sqrt{\text{m}}$  and the crack growth rate in the plateau was  $1.5 \times 10^{-7} \text{ m/sec}$  as shown in Figure 28.

The heat treated W-3 alloy did not show the SCC propagation at the open-circuit, anodic, and cathodic potentials in the NaCl solution.

#### 4.1.4 Constant Load Tests

Constant load tests on smooth tensile specimens of the W-3 alloy were performed in aerated 3% NaCl solution. Tensile stresses were applied using dead weight. When the stresses of lower than 140 ksi were applied, fracture did not occur after 200 hr testing. Optical microscopy showed that no crack was initiated on the specimen surface, and that thin oxide film was formed on the surface.

However, at the stress of 140 ksi, the specimen was fractured in less than 1 hr. It is thought that the sudden fracture occurred because the applied stress may be close enough to the ultimate tensile strength.

#### 4.1.5 SCC in Sulfide Cracking Solution

The  $K_I$  vs. crack growth rate curves for the alloys in the NACE recommended sulfide cracking solution

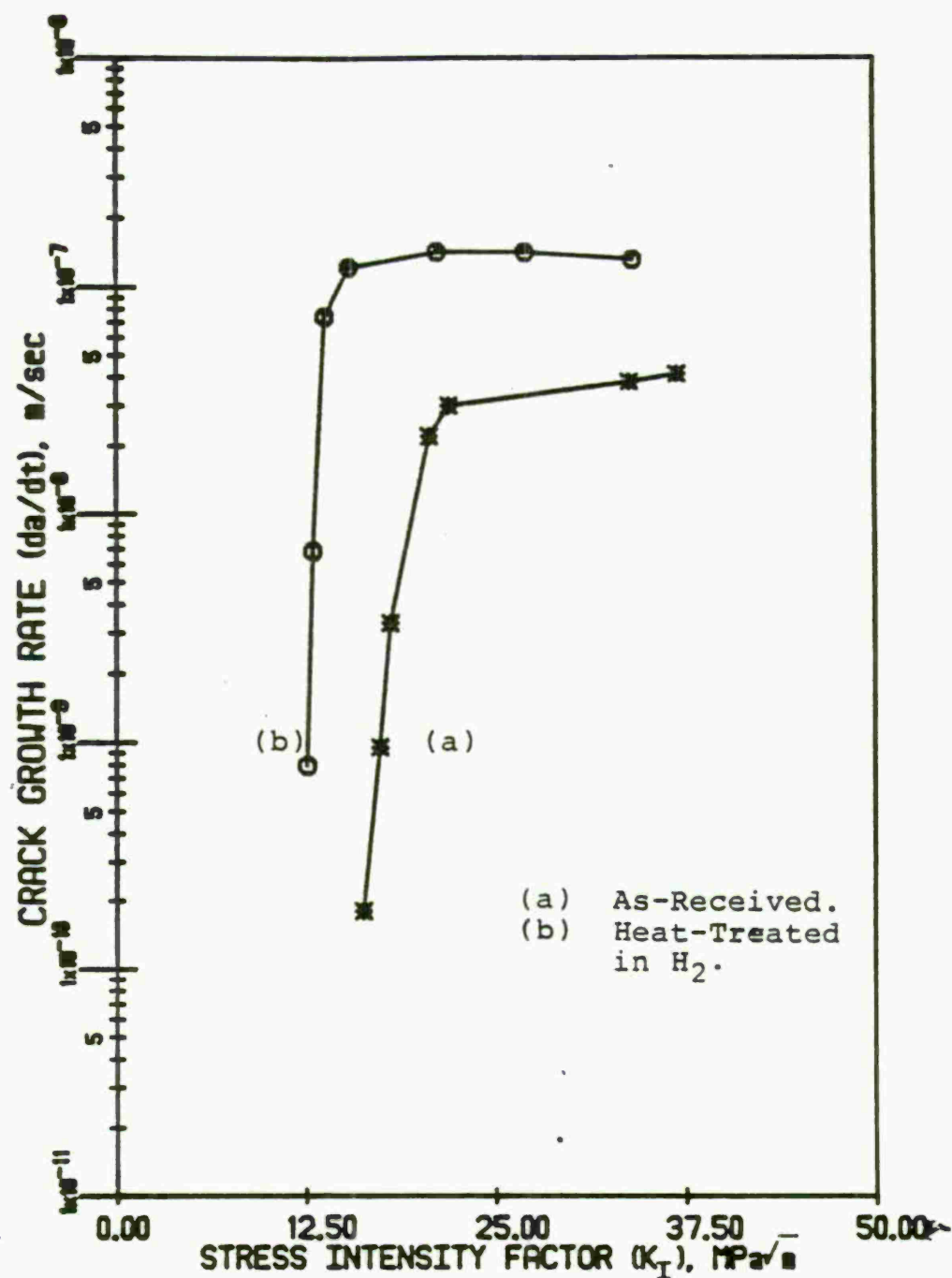


Figure 27 Influence of Heat Treatment in Hydrogen Atmosphere on the SCC Behavior of the W-10 Alloy in NaCl Solution  $K_{ISCC}$  was Lowered and Crack Growth Rate was Increased.



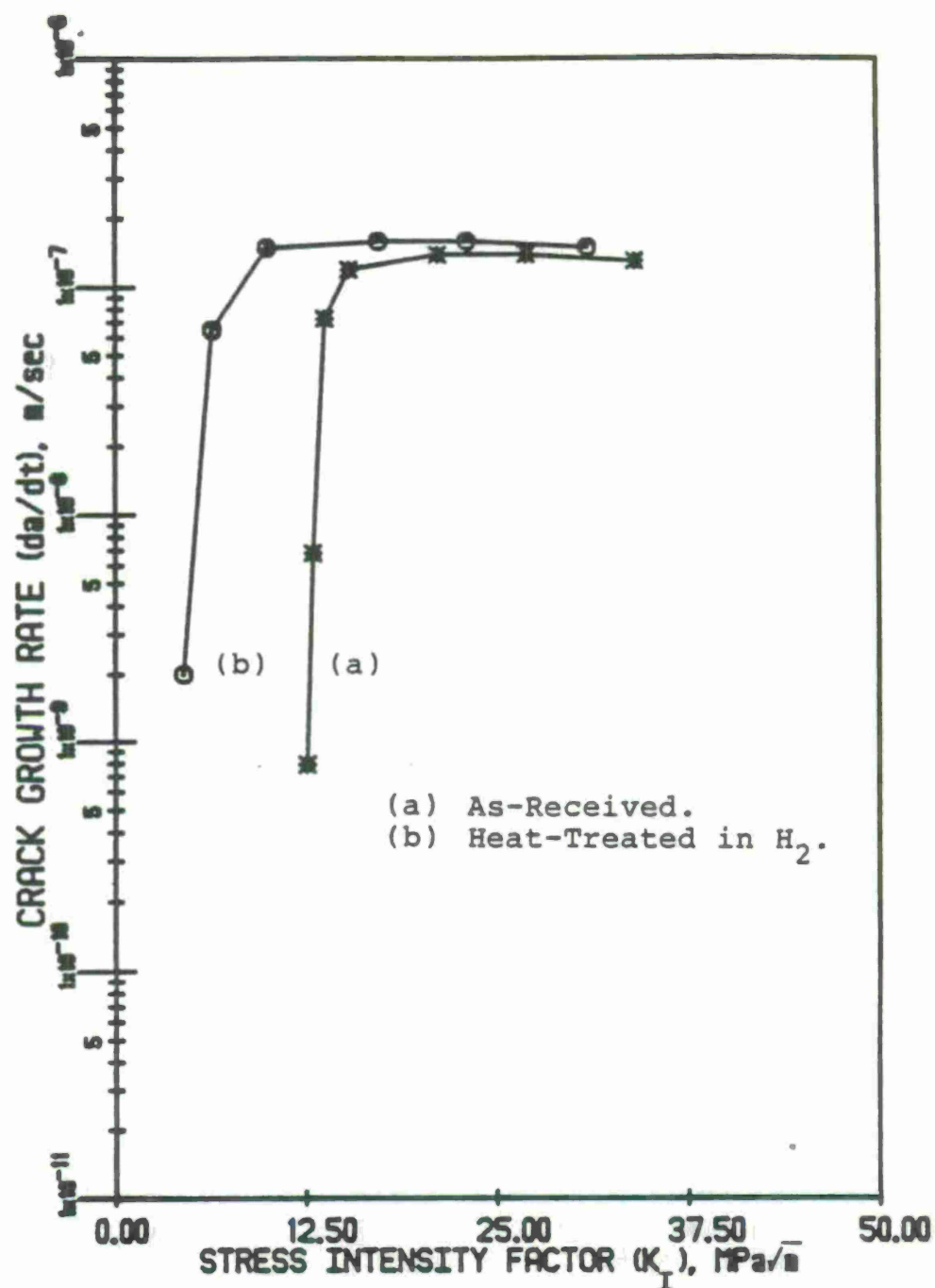


Figure 28 Influence of Heat Treatment in Hydrogen Atmosphere on the  $K_{ISCC}$  and Crack Growth Rate of the W-10 Alloy at -1.2 V vs. SCE in NaCl Solution.  $K_{ISCC}$  Was Lowered and Crack Growth Rate Was Not Changed Very Much.

are presented in Figures 29 and 30. Heat treatment of the W-10 alloy in hydrogen atmosphere did not affect  $K_{ISCC}$  of the specimen, but resulted in faster crack propagation in the plateau region. In the W-3 alloy, heat treatment in hydrogen atmosphere increased the crack growth rate and lowered  $K_{ISCC}$ . Heat treatment in Ar slightly increased both the crack growth rate and  $K_{ISCC}$ . However, the W-3 alloy shows much higher  $K_{ISCC}$  and slower crack growth rate than the W-10 alloy.

## 4.2 Fractography

### 4.2.1 Effects of Polarization

Fractographs for the W-10 alloy from the tension test are shown in Figure 31. Failure occurred primarily by ductile rupture of the matrix with separation of tungsten-tungsten interfaces and cleavage of the tungsten grains. In fact, tungsten-tungsten grain boundaries, cleavage of the tungsten particles, dimples in the matrix area, and secondary cracks are all present.

In the precracked region, fracture predominantly occurs through tungsten-matrix interfaces, although cleavage of a tungsten grain is sometimes observed. Most of the matrix phase has run out of this region, creating the interparticle voids as shown in Figure 32. These voids may have played a role as initiation sites for fatigue pre-cracking.

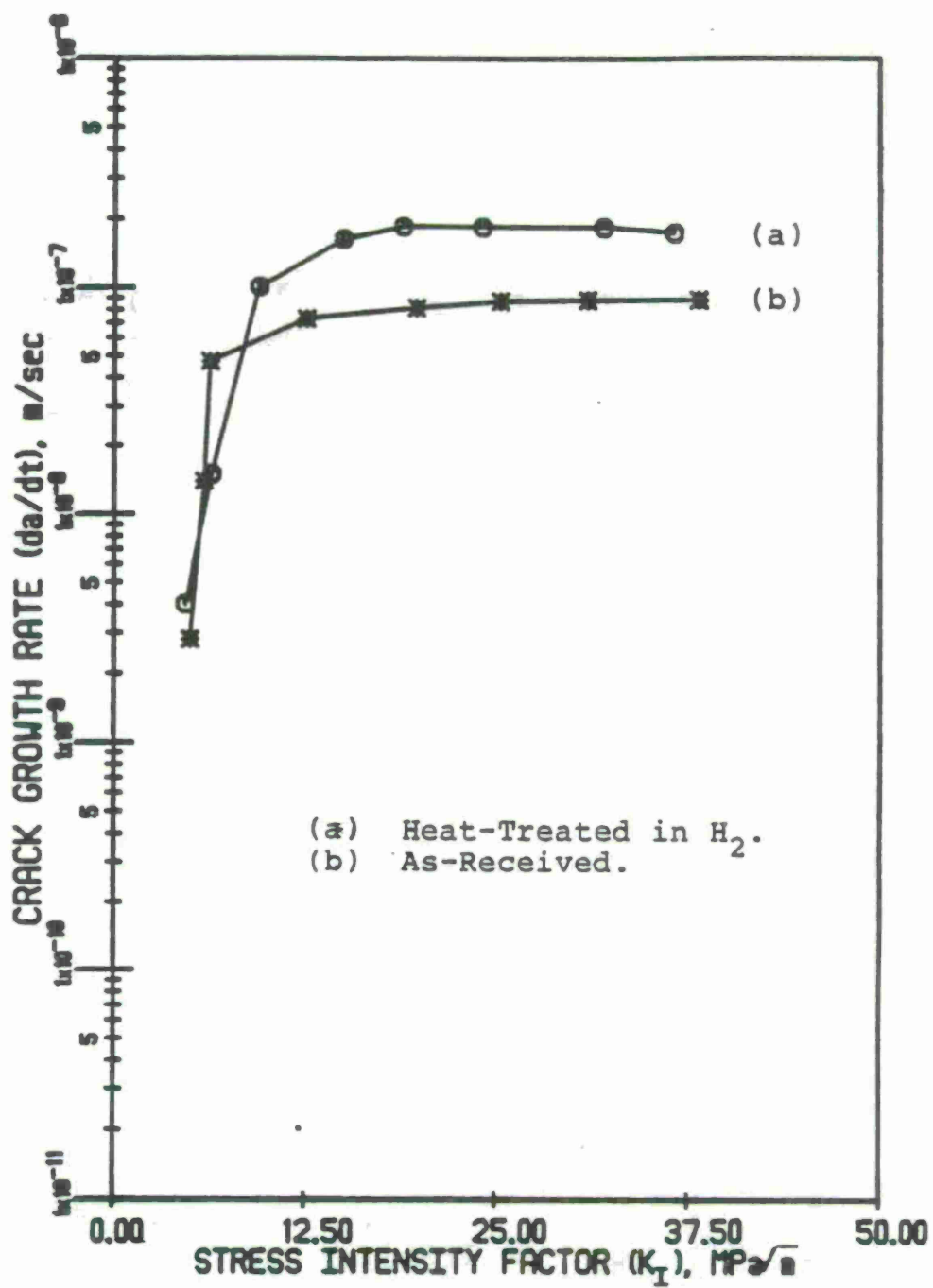


Figure 29 SCC Behavior of the W-10 Alloy in Sulfide Cracking Solution.

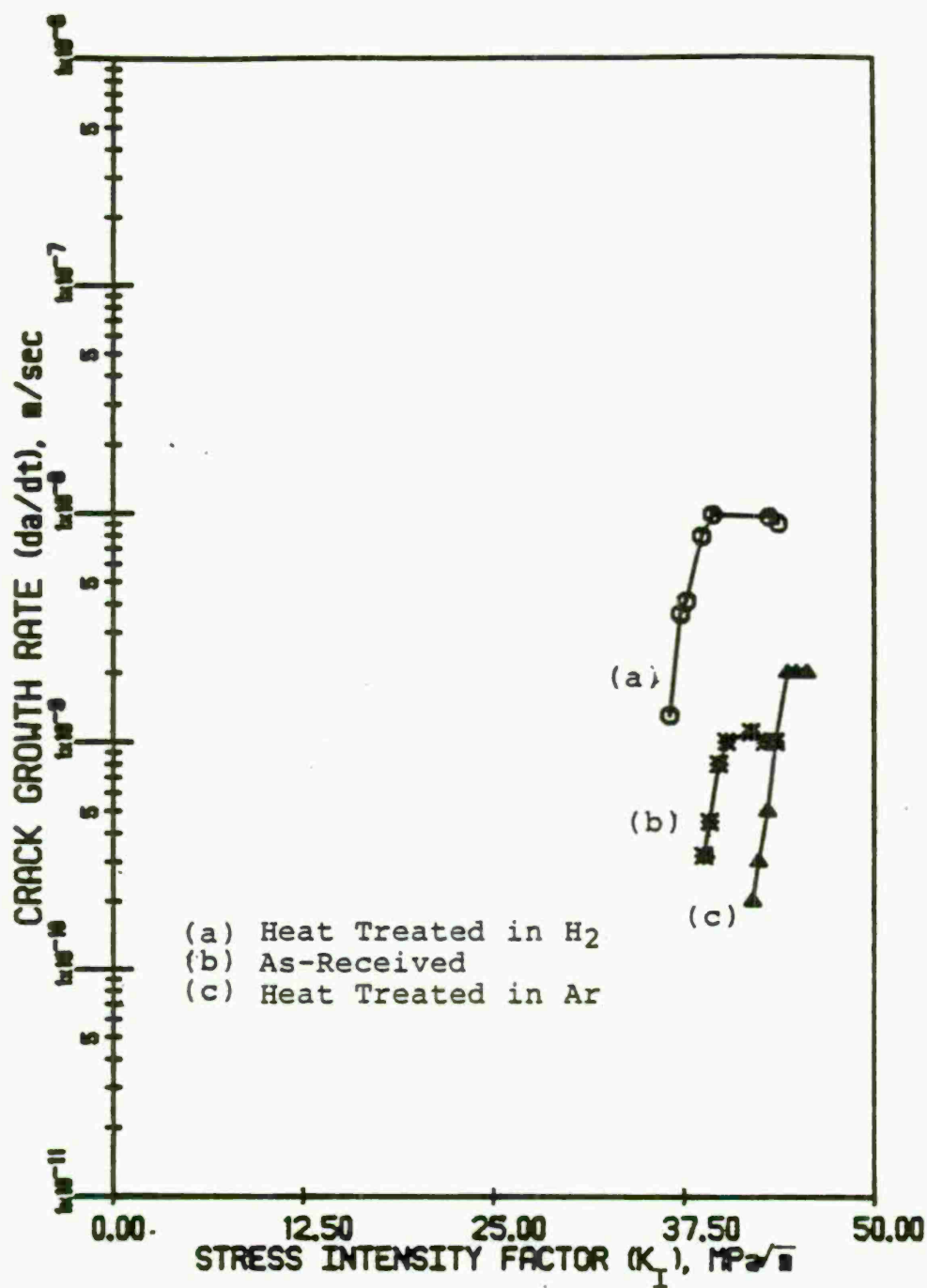
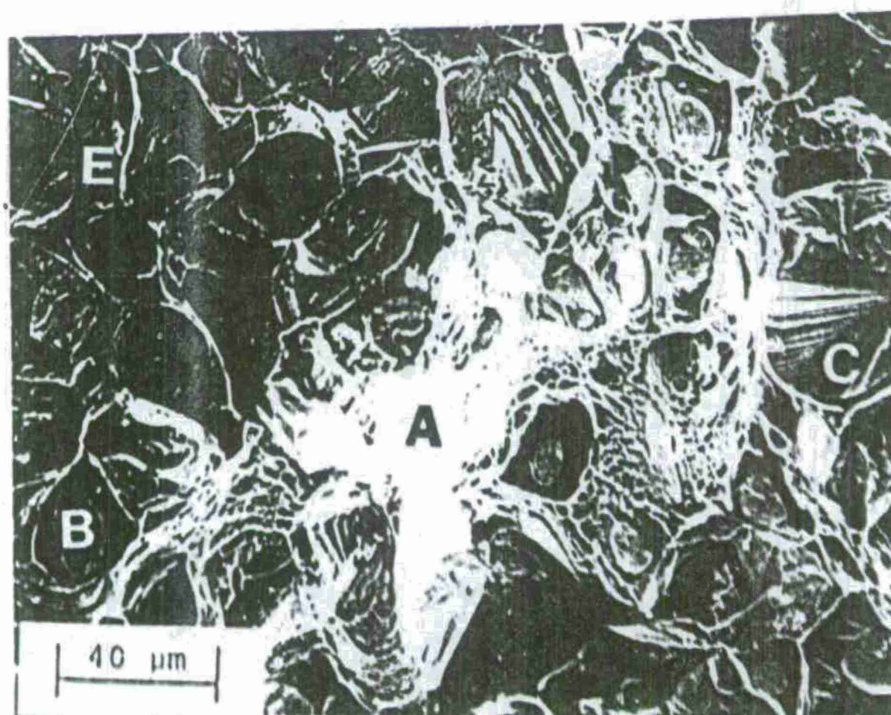
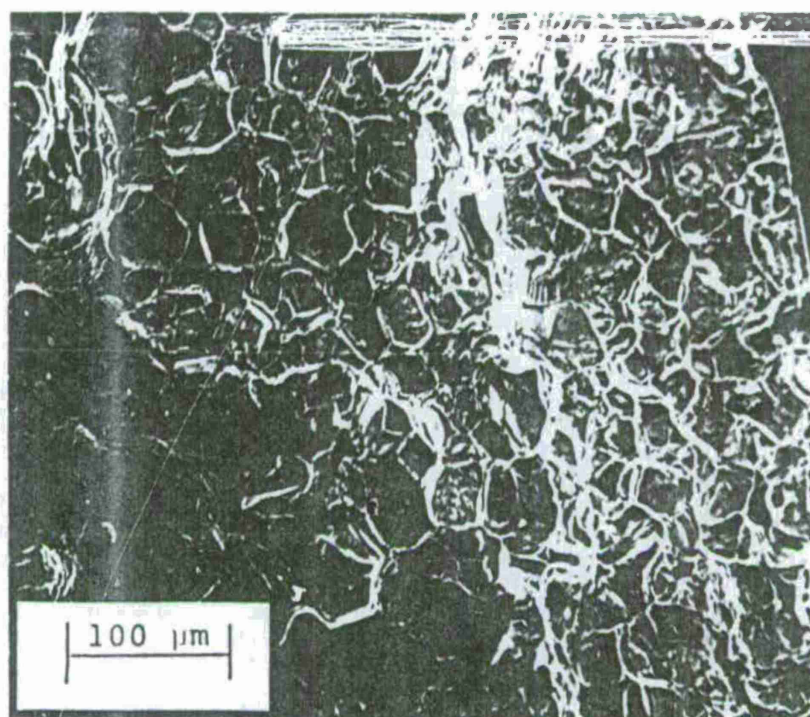


Figure 30 Heat Treatment Effects on the  $K_{ISCC}$  and Crack Growth Rate of the W-3 Alloy in Sulfide Cracking Solution.





**Figure 31** Fractographs for Tension Specimen of the W-10 Alloy, Showing Rupture of the Matrix (A), Tungsten-Tungsten Interfaces (B), Cleavage of the Tungsten Particles (C), Dimples in the Matrix (D), and Secondary Cracks (E).



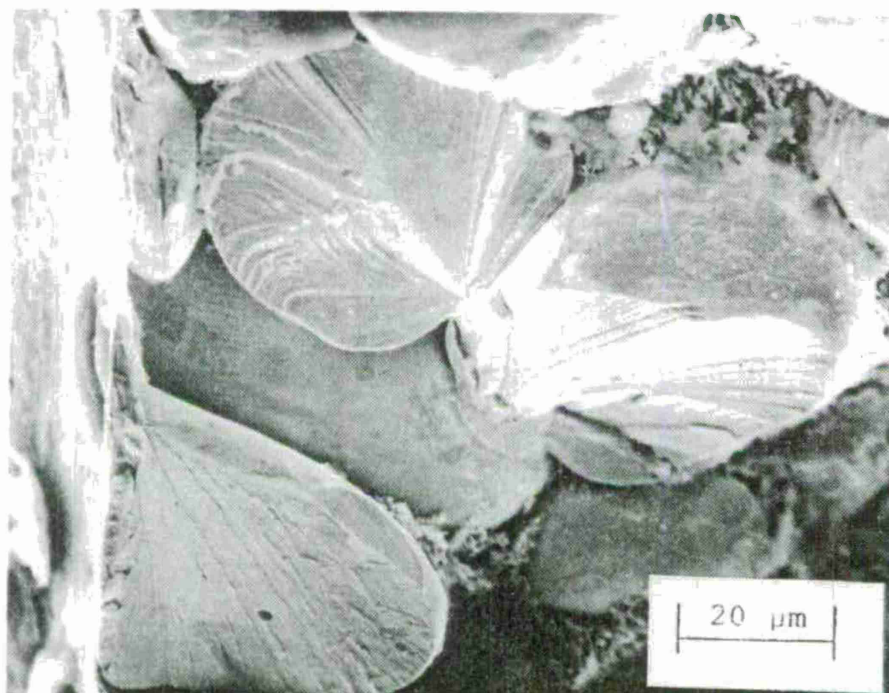
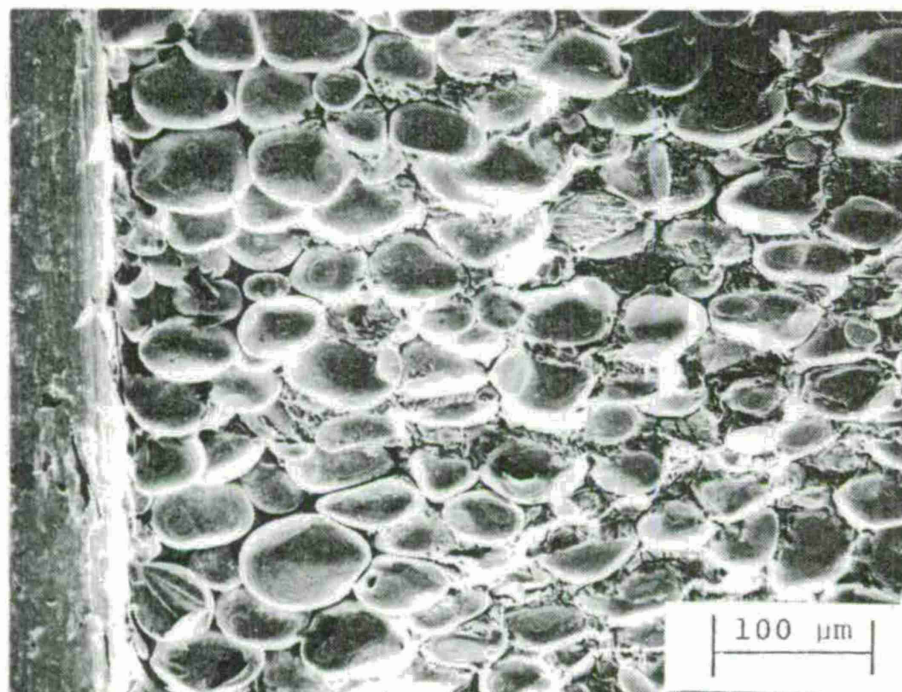


Figure 32    Fracture Surface of the W-10 Alloy in the  
Pre-cracked Region.

At the open-circuit potential and anodic potentials, cracks propagated by separation of tungsten-tungsten and tungsten-matrix interfaces, and ductile rupture of the matrix phase, as shown in Figures 33 and 34. At -1.2 V vs. SCE, cracks propagated by separation of tungsten-matrix and tungsten-tungsten interface, and cleavage of some tungsten grains, as shown in Figure 35. Some secondary cracks also are visible. In some cases (Figure 36), the localized nature of precipitate formation was confirmed by scanning electron microscopy. Groups of tungsten particles were observed to be covered with an apparently brittle film. In these local areas, fracture appeared to occur along either the interface between the brittle film and the matrix phase or that between the tungsten particles and the precipitate. The precipitate itself failed readily in an intergranular fashion. In Figure 37, some precipitates also are visible in fractured tungsten-tungsten grain boundaries. They have been identified as  $W(Ni\ Fe)$  intermetallic compounds and are responsible for embrittlement of tungsten heavy alloys, as shown by several investigators.<sup>14,68</sup>

Fractographs for a tensile specimen of the W-3 alloy are shown in Figure 38. Fracture occurred primarily by cleavage of the tungsten grains. Some dimples in the matrix phase and interfaces of tungsten-tungsten are also



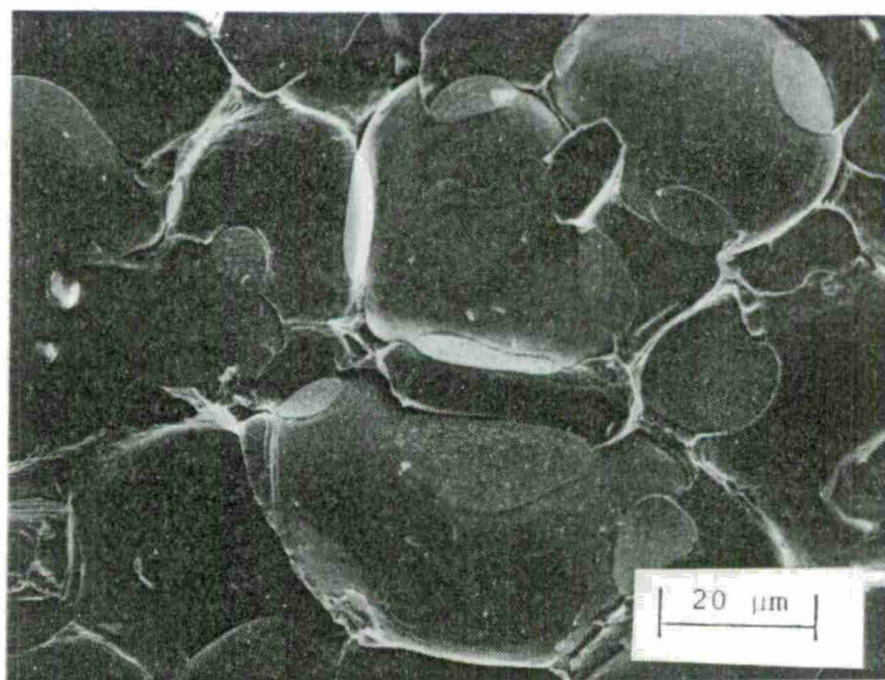
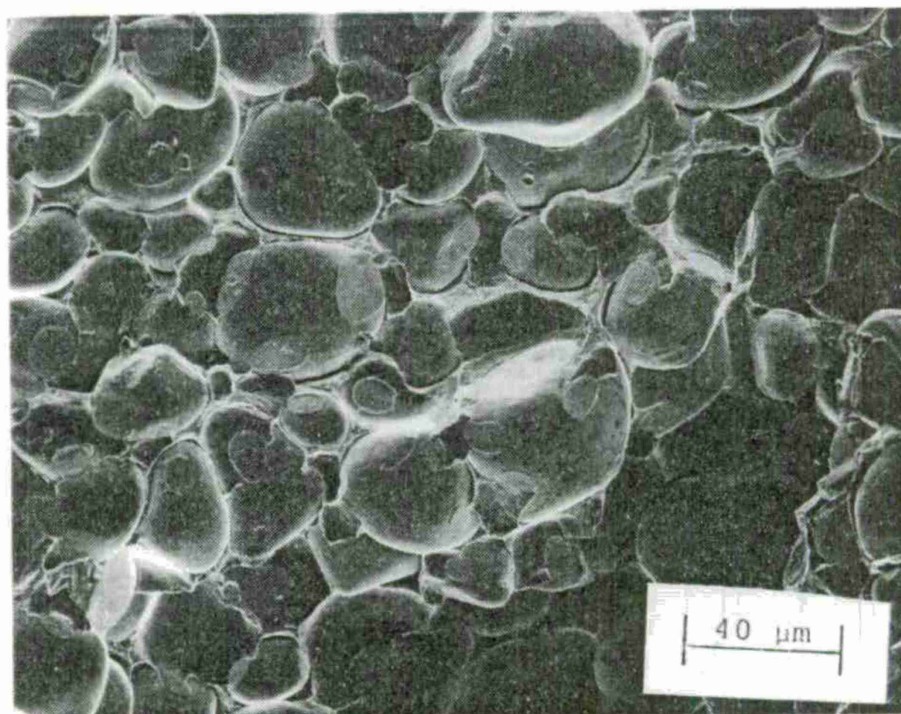


Figure 33 Fracture Surface of the W-10 Alloy Specimen Tested at the Open-Circuit Potential in 3% NaCl Solution.

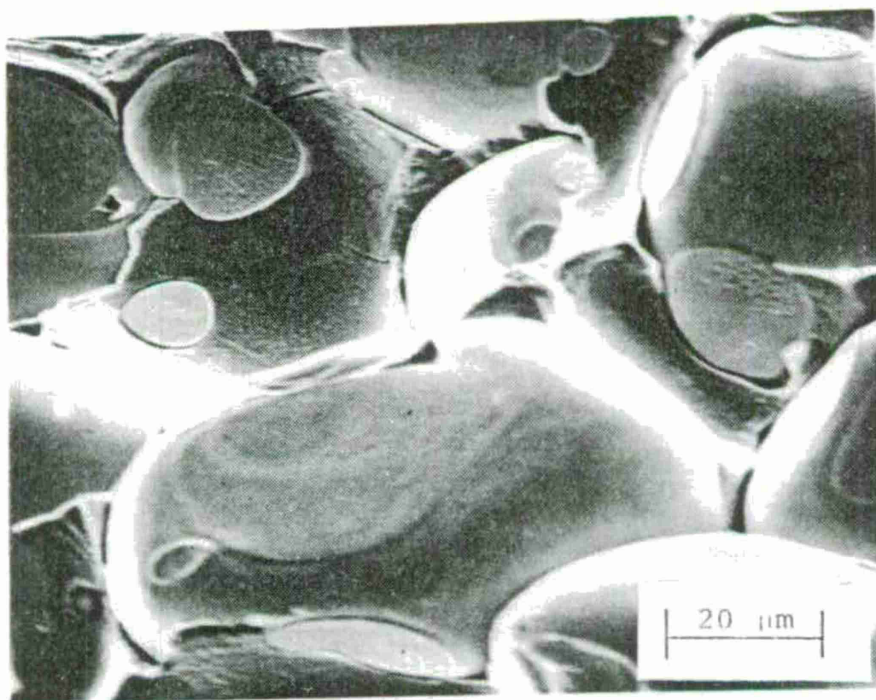
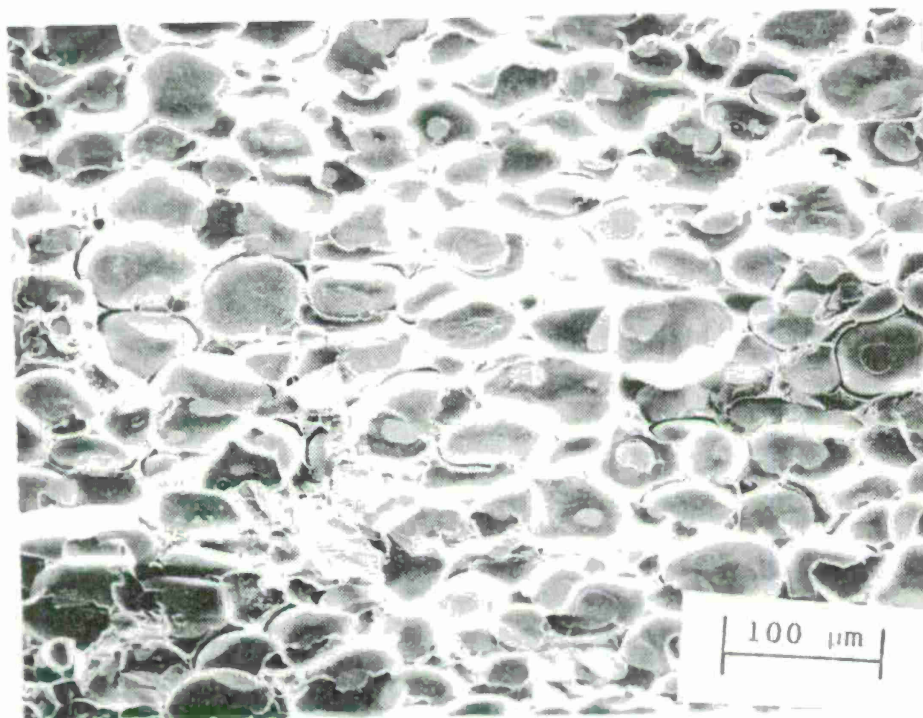


Figure 34 Fracture Morphology of the W-10 Alloy Sample  
Tested at  $-0.2\text{V}$  vs. SCE in 3% NaCl Solution.



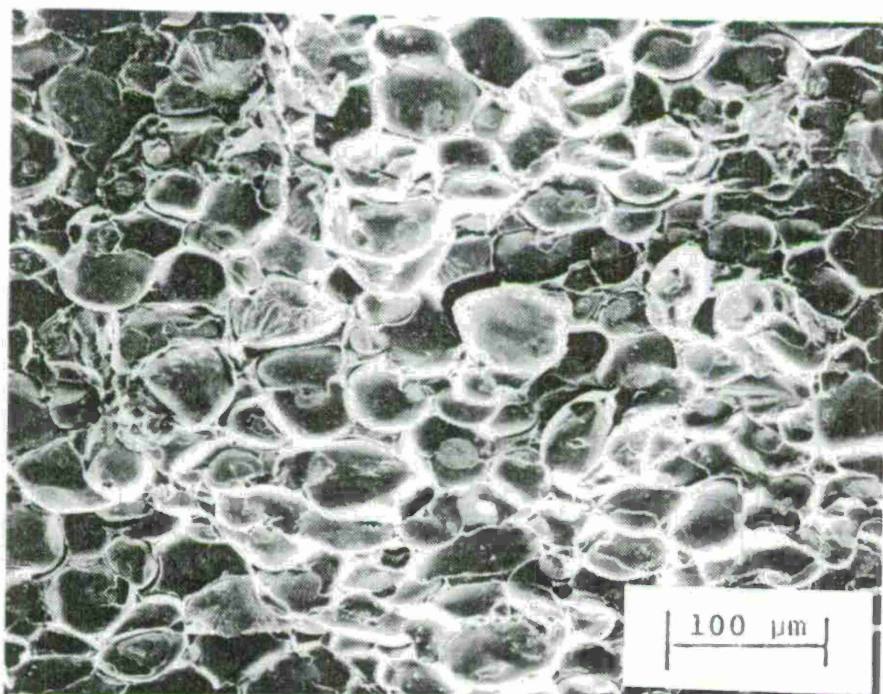


Figure 35     Fractograph of the W-10 Alloy Sample Tested at  
                 -1.2 V vs. SCE in 3% NaCl Solution.

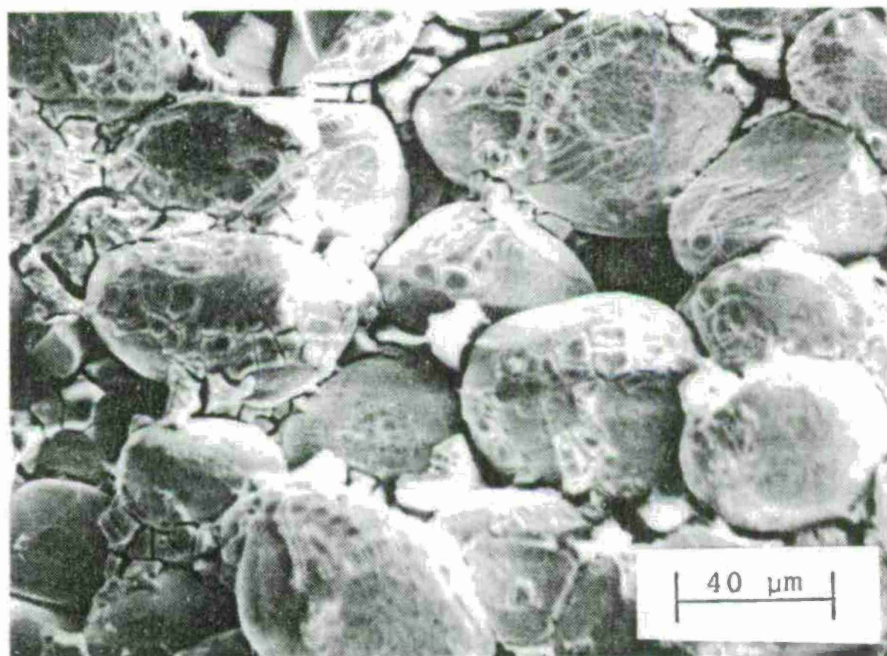
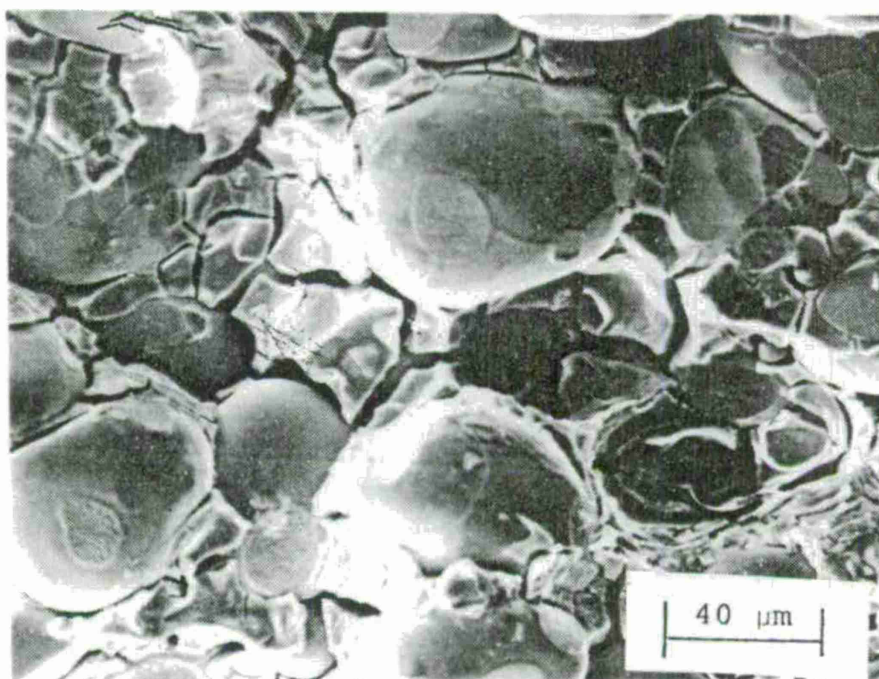


Figure 36      Scanning Electron Micrographs of the W-10 Alloy  
Showing Regions of Brittle Interphase Boundary  
Precipitate Exposed on Fracture Surface.

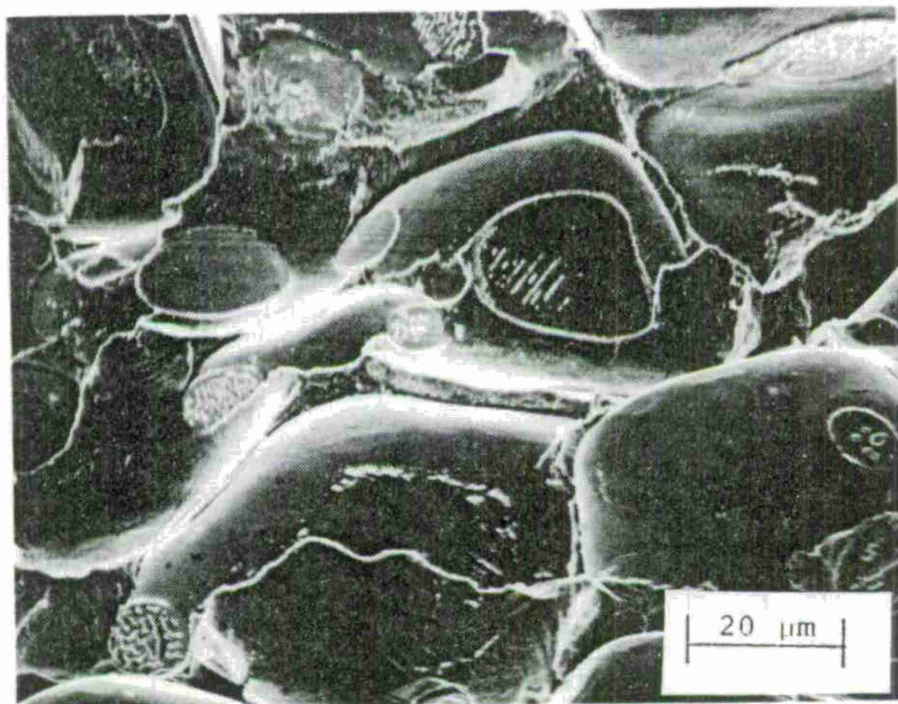


Figure 37      Fracture Surface of the W-10 Alloy Showing Pre-  
cipitates Exposed on the Tungsten-Tungsten Grain  
Boundaries.



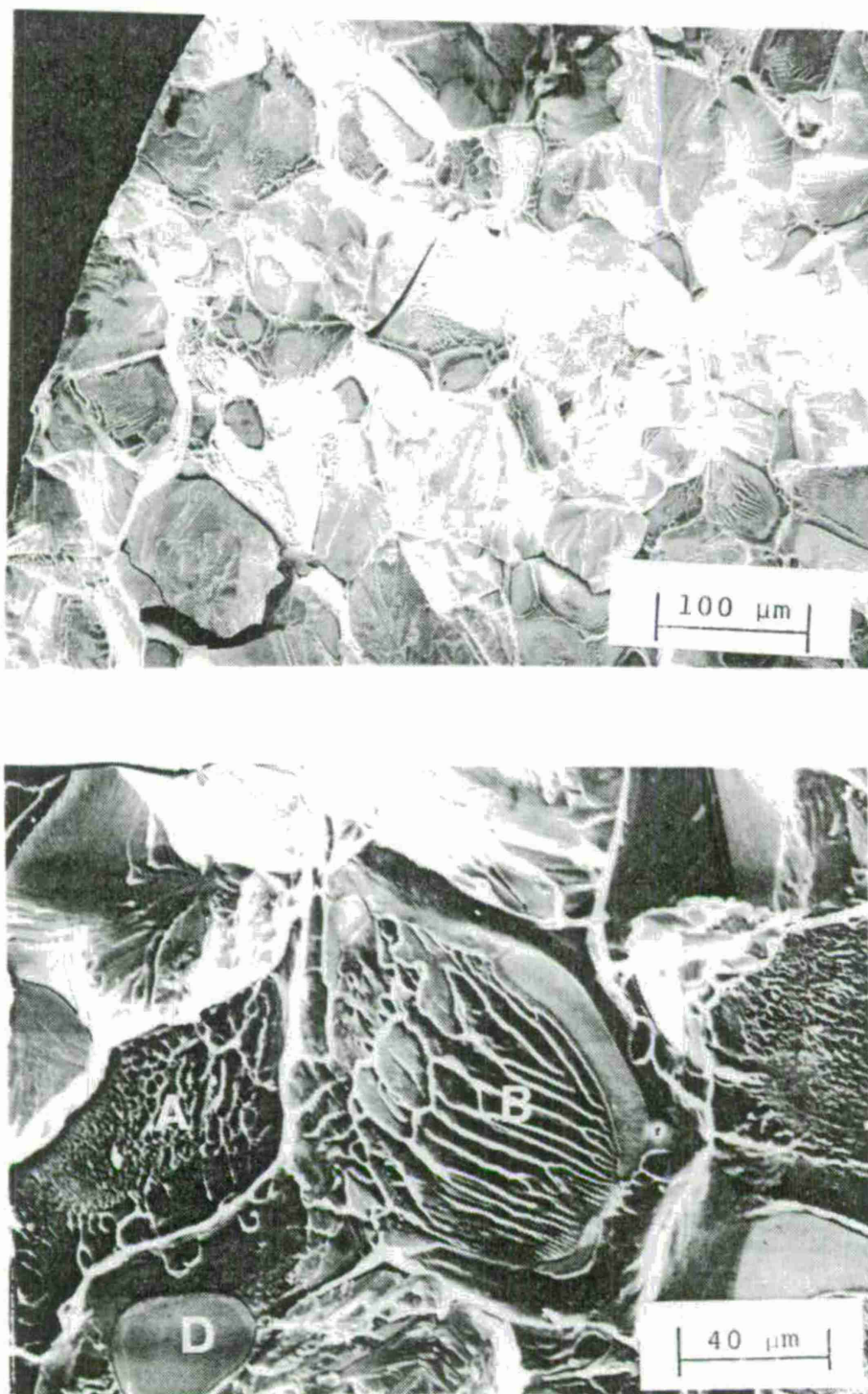


Figure 38 Fractographs for a Tension Specimen of the W-3 Alloy Showing Dimples (A) and River Lines (B) in the Matrix, Cleavage of the Tungsten Particle (C), and the Tungsten-Tungsten Interfaces (D).



visible.

In the precracked region, ductile rupture of the matrix with cleavage of the tungsten grains is predominant (Figure 39). Secondary cracks also are present.

#### 4.2.2 Effects of Hydrogen Catalyst

In 3% NaCl solution containing 60 ppm of As, fracture of the W-10 alloy occurred through tungsten-matrix interfaces and tungsten-tungsten grain boundaries as shown in Figure 40.

In 10%  $H_2SO_4$  containing 60 ppm of As, fracture occurred predominantly with the separation of tungsten-matrix interfaces and tungsten-tungsten grain boundaries although cleavage of a tungsten particle was visible as shown in Figure 41.

As shown in Figure 42, fracture of the W-3 alloy occurred in 10%  $H_2SO_4$  containing 60 ppm of As primarily by cleavage of tungsten grains and dimple formation in the matrix.

#### 4.2.3 Effects of Heat Treatment

As shown in Figure 43, fracture of the heat treated W-10 alloy in aerated 3% NaCl solution occurred with ductile rupture of the matrix, separation of tungsten-matrix interfaces and tungsten-tungsten grain boundaries. Cleavage of a tungsten particle also is visible.

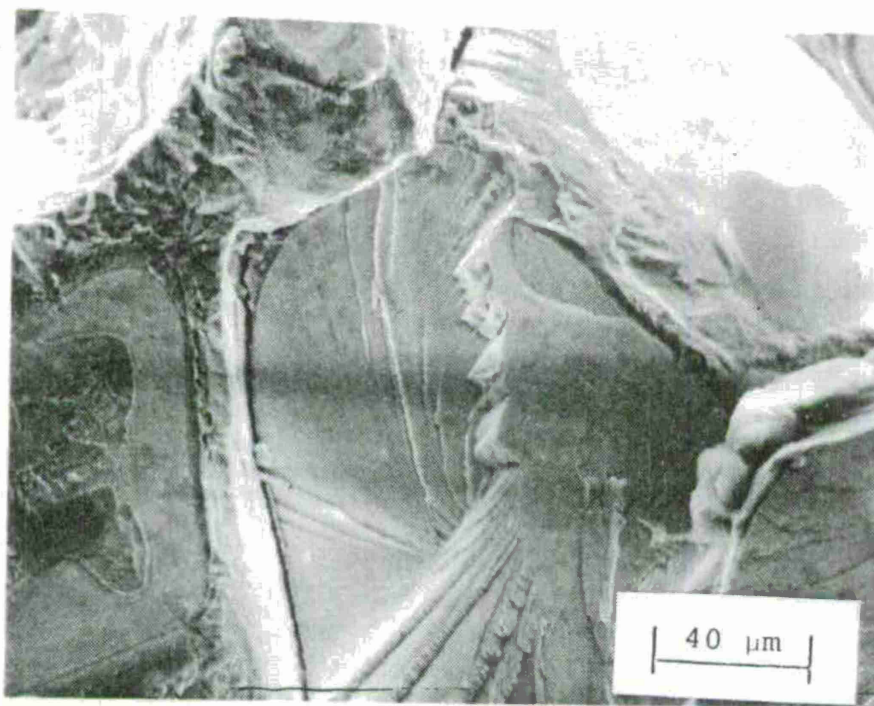
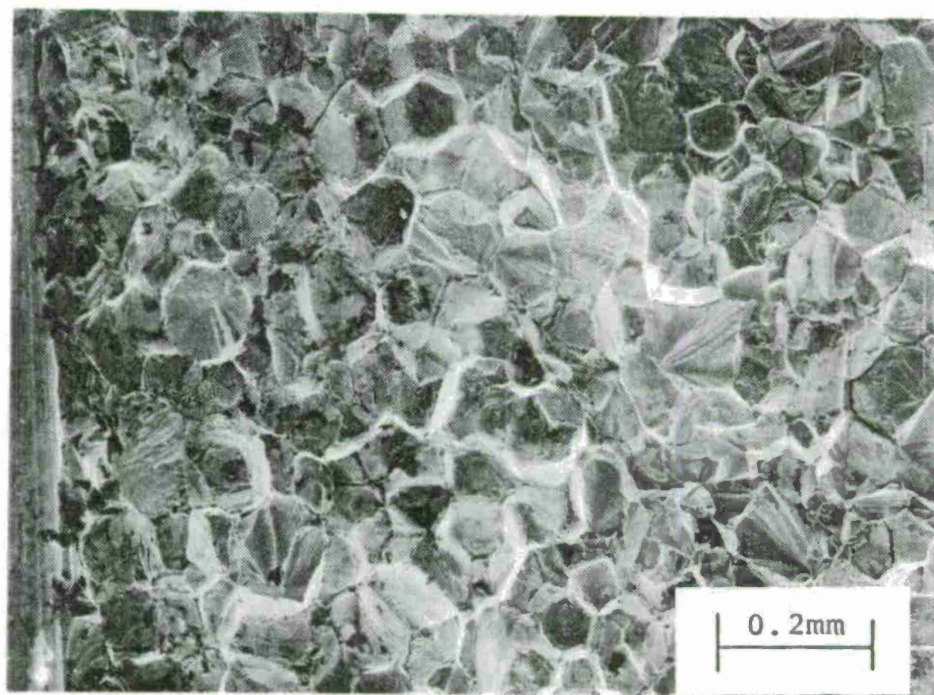


Figure 39 Fracture Surface of the W-3 Alloy in the Precracked Region, Showing Ductile Rupture of the Matrix with Cleavage of the Tungsten Particles.

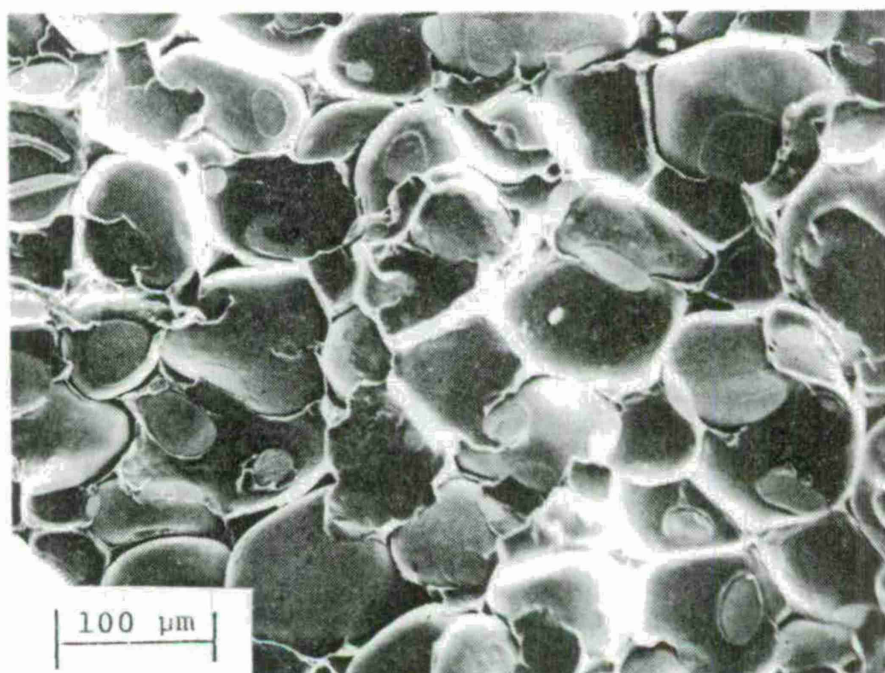


Figure 40      Fracture Appearance of the W-10 Alloy in 3%  
NaCl Solution Containing 60 ppm of As.



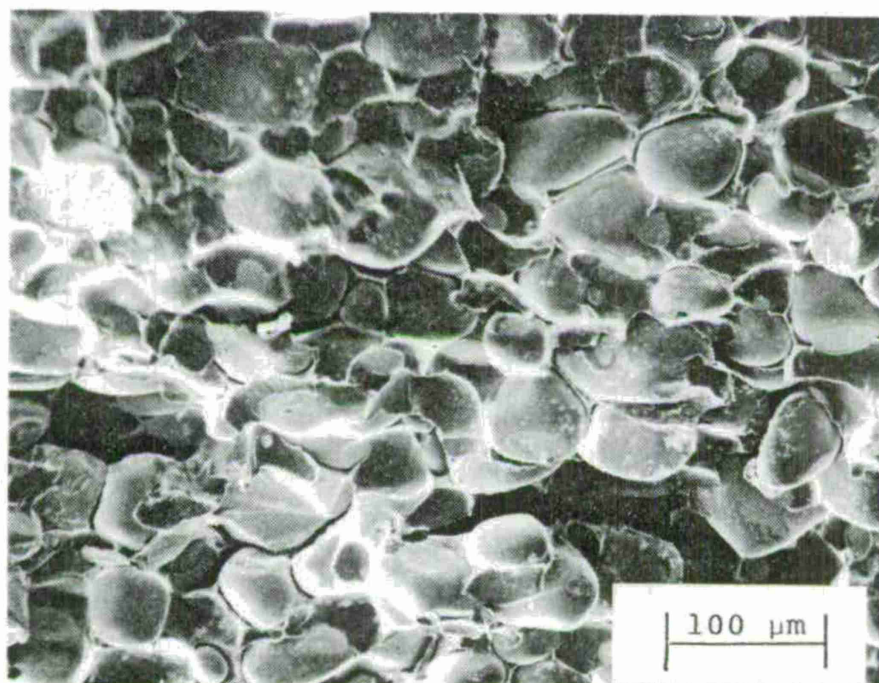


Figure 41    Fracture Morphology of the W-10 Alloy Tested at  
-1.2V vs. SCE in 10%  $\text{H}_2\text{SO}_4$  Containing 60 ppm of  
As.



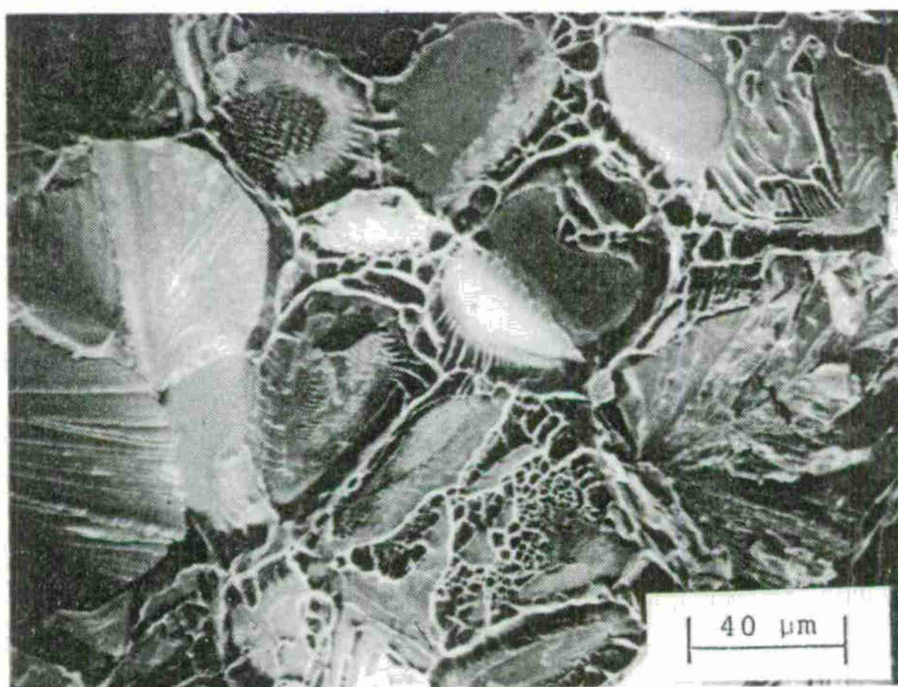
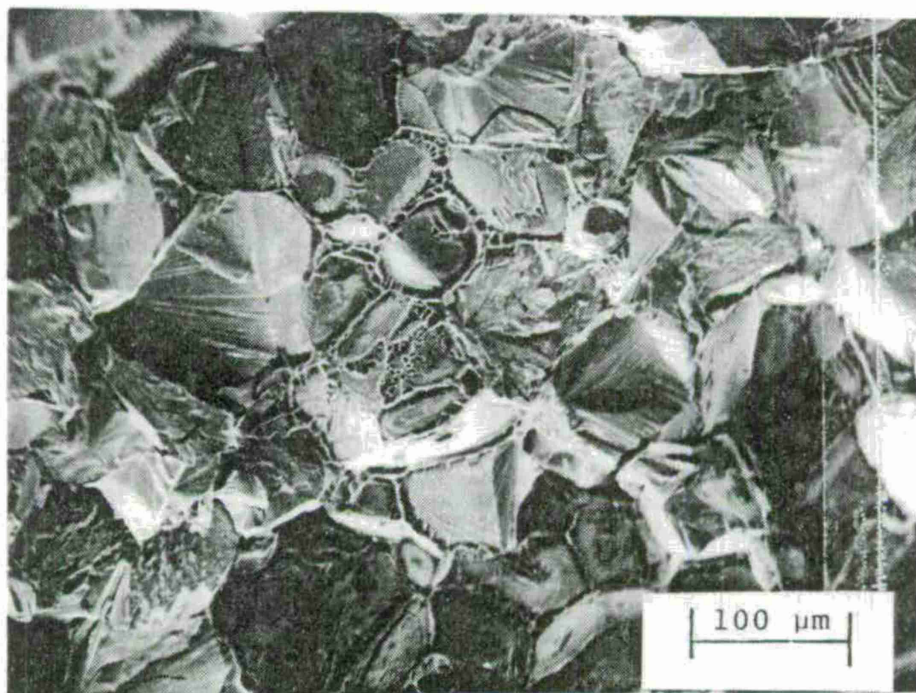


Figure 42      Fracture Appearance of the W-3 Alloy Tested at  
-1.2 V vs. SCE in 10%  $\text{H}_2\text{SO}_4$  Containing 60 ppm of  
As.

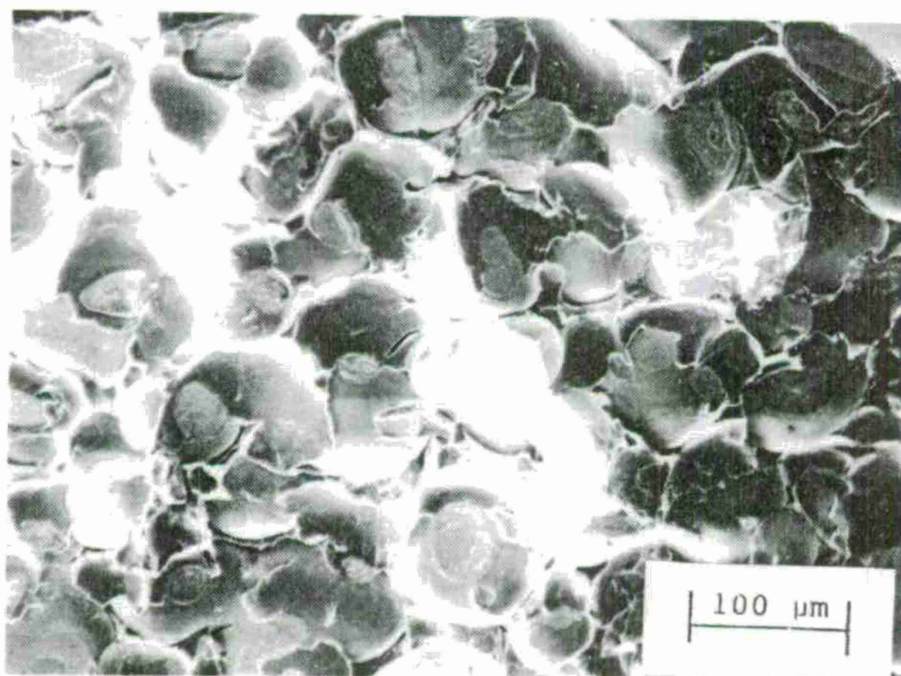
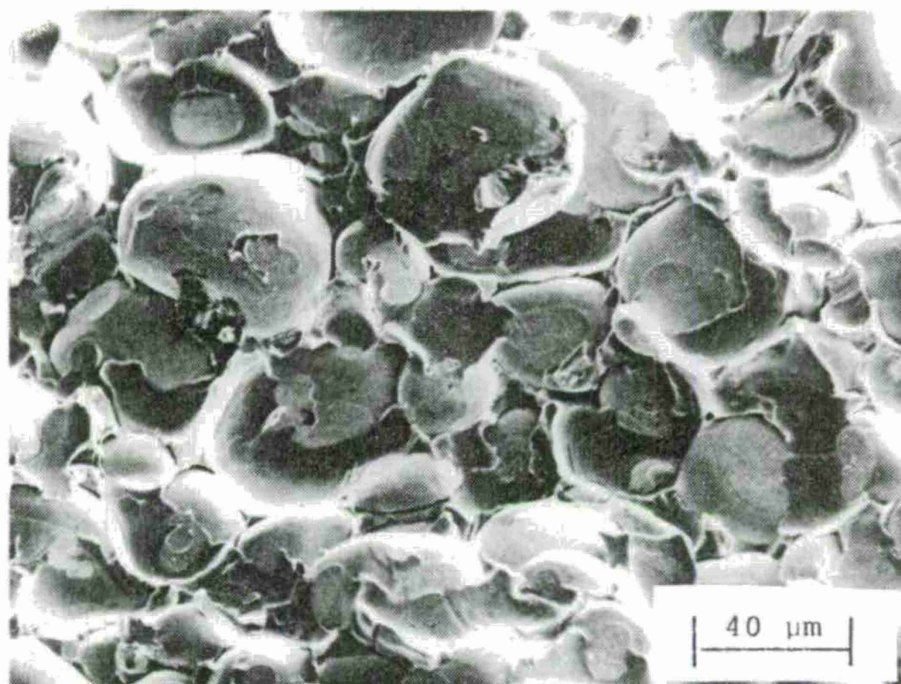


Figure 43 Fracture Morphology of the Heat Treated W-10 Alloy Sample Tested in 3% NaCl Solution.

#### 4.2.4 Constant Load Tests

Fracture morphology is similar to that of tension specimen tested in the air, as shown in Figure 44. Fracture occurred by dimple formation in the matrix, cleavage of the tungsten grains, and separation of tungsten-tungsten grain boundaries.

#### 4.2.5 Sulfide Stress Cracking

Fractographs of the W-10 alloy are shown in Figure 45. Although cleavage of some tungsten grains is visible, failure occurs primarily by separation of the tungsten-tungsten grain boundaries and rupture of the matrix. As shown in Figure 46, failure of the W-3 alloy occurs mainly by cleavage of tungsten grains and dimple formation in the matrix.



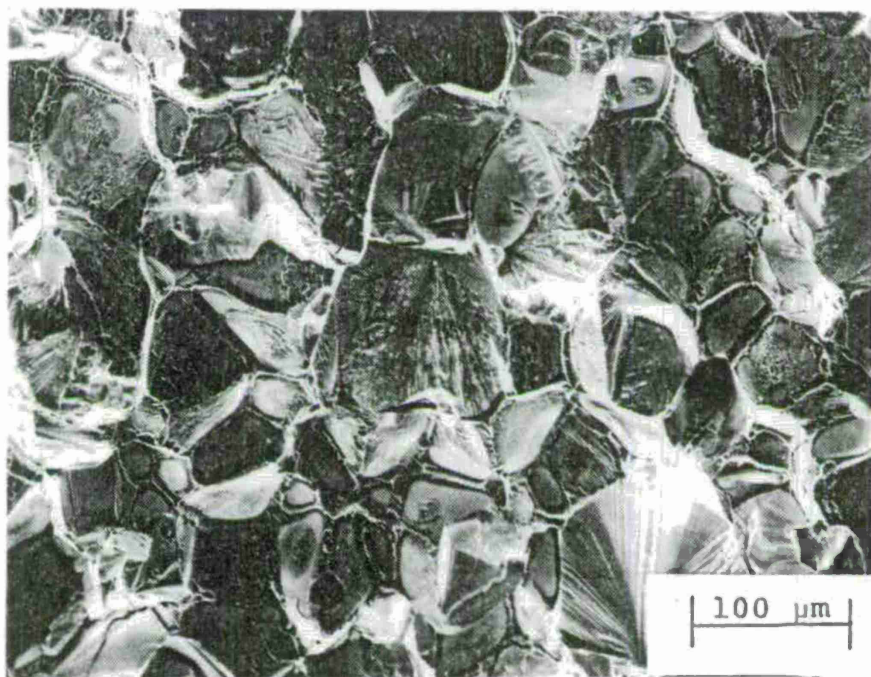


Figure 44      Fracture Morphology of the W-3 Alloy Sample  
Tested in 3% NaCl Solution Under Constant Load.



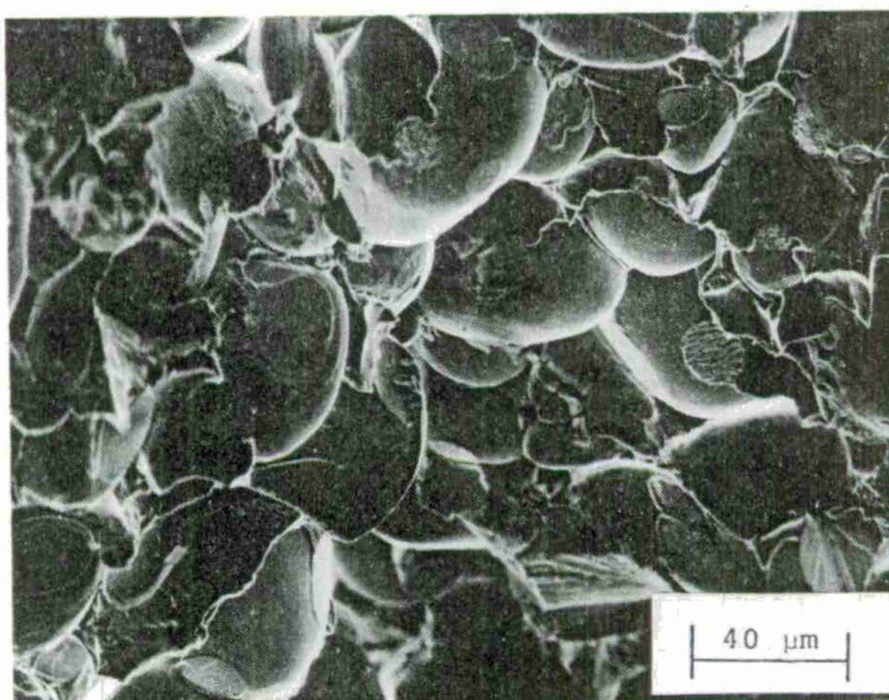
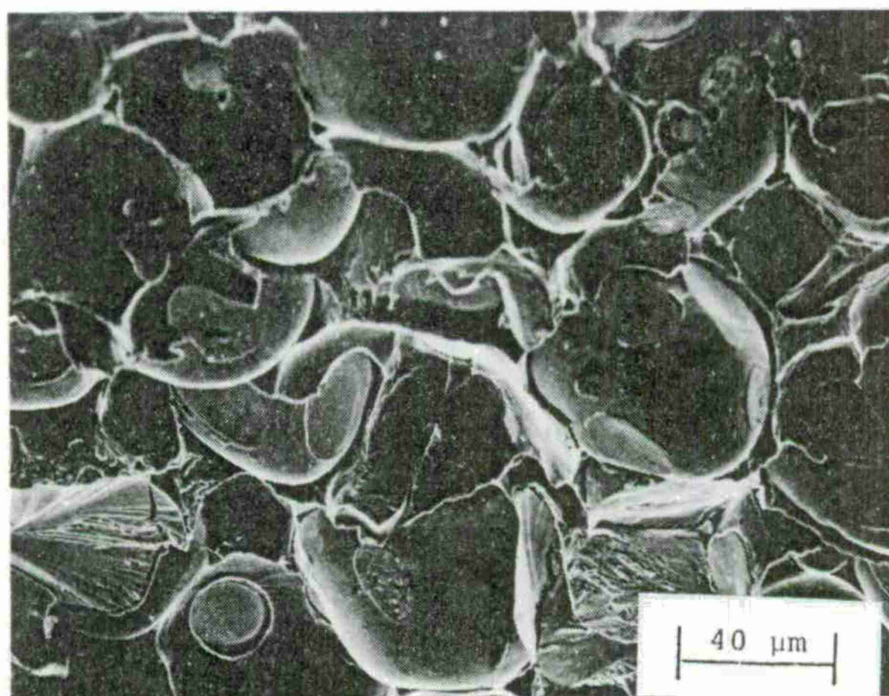
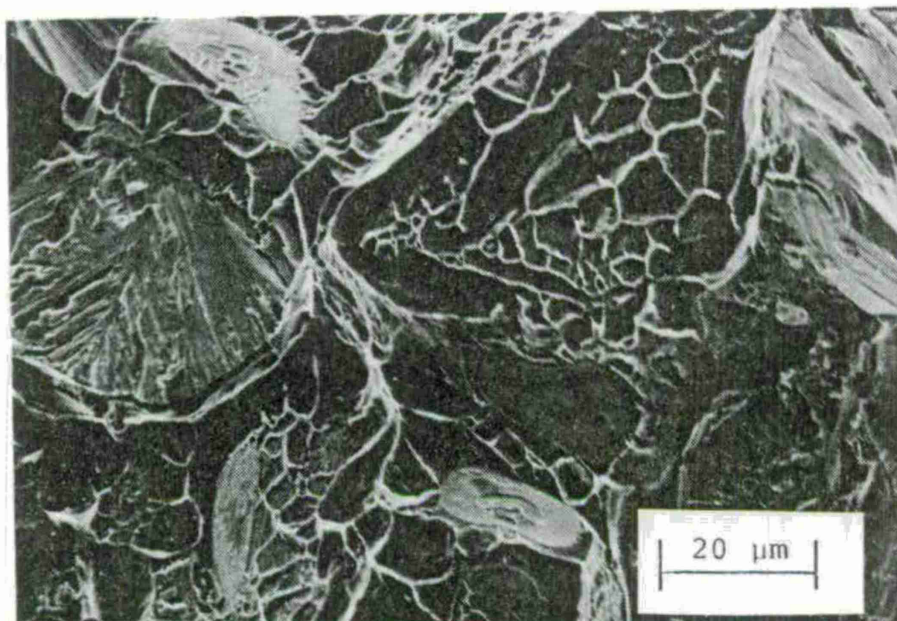
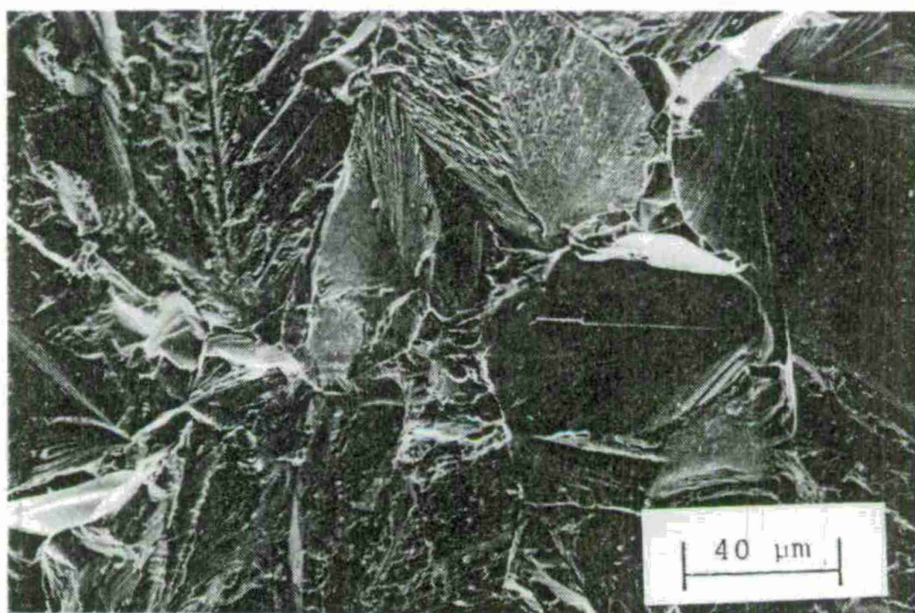


Figure 45 Fractographs for the W-10 Alloy Tested in the Sulfide Cracking Solution.



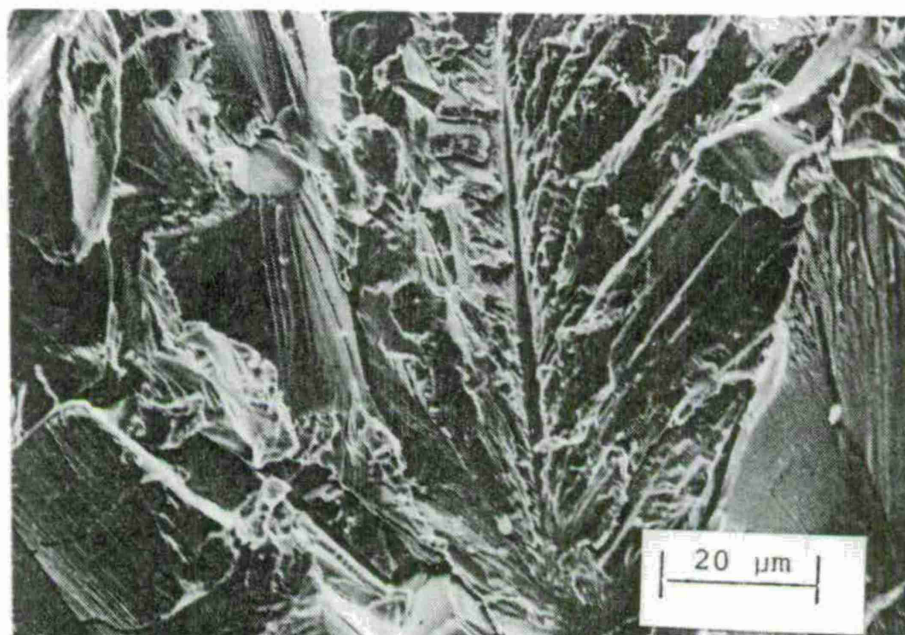
(a)



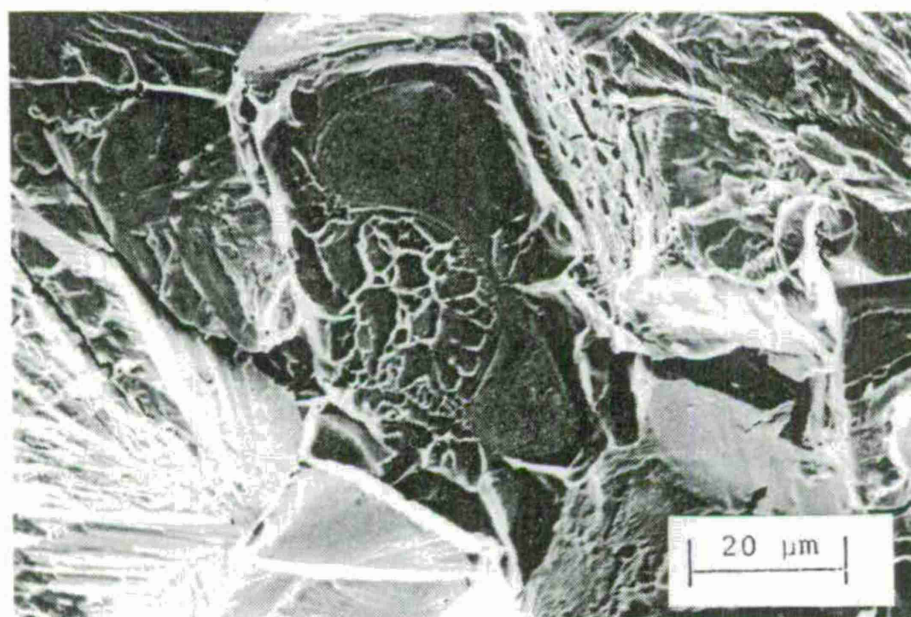
(b)

Figure 46 Fracture Appearance of the W-3 Alloy Tested in the Sulfide Cracking Solution.  
(a) Dimples in the Matrix.  
(b) Cleavage of the Tungsten Grains and Dimples in the Matrix.





(c)



(d)

Figure 46 Fracture Appearance of the W-3 Alloy Tested in the Sulfide Cracking Solution.  
(c) Higher Magnification of the Cleavage in (b).  
(d) Higher Magnification of the Dimples in (b).

## PART 5

### DISCUSSION

#### 5.1 Effects of Polarization

The results show that the W-10 alloy is susceptible to SCC in aerated 3% NaCl solution, but that the W-3 alloy is not. In both alloys, corrosion took place primarily in the matrix. Under the open-circuit potential, the matrix and tungsten phases are thought to form an electro chemical cell, where the matrix serves as the anode and the tungsten grains as the cathode. Hence, stress corrosion cracks propagate at the expense of active dissolution in the matrix.

Koger<sup>78</sup> determined polarization curves of a W-3.5Ni-1.5Fe alloy in aqueous chloride solutions. To fully explain the corrosion behavior of the alloy, he obtained polarization curves for its constituent phases: tungsten and Ni-24Fe-21W alloy. As shown in Figure 47, tungsten and the W-3.5Ni-1.5Fe alloy both show active-passive transitions with similarly shaped curves. However, the Ni-24Fe-21W alloy shows only active dissolution. Therefore, it was thought that the tungsten phases are responsible for the passive behavior of the two-phase alloys (W-3.5Ni-1.5Fe) and the matrix phases contribute to active dissolution behavior.



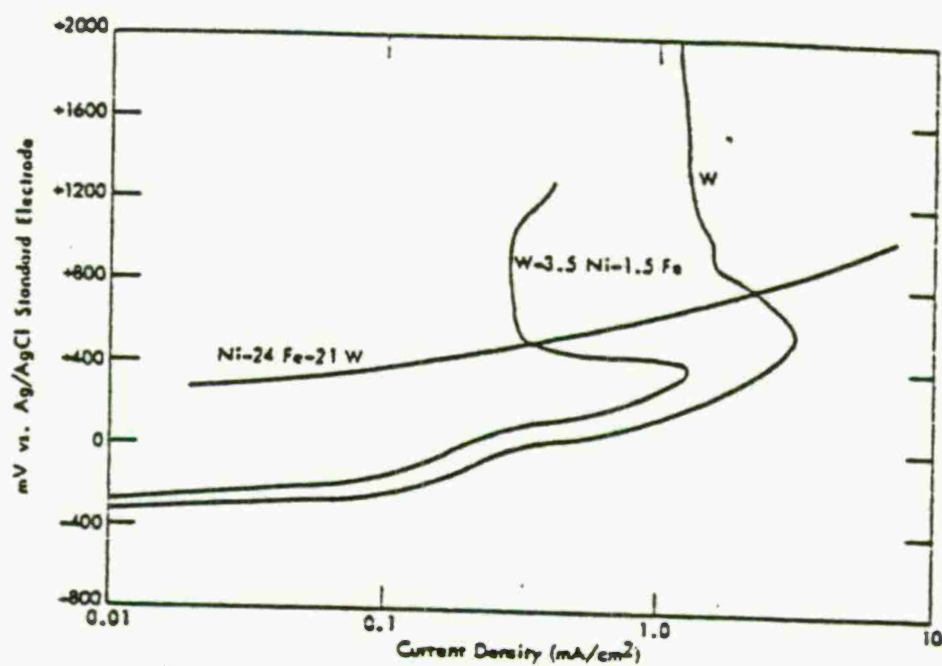


Figure 47 Polarization Curves of W-3.5 Ni-1.5 Fe, W, and Ni-24 Fe-21 W exposed to 0.1M NaCl, pH = 9.8

If SCC propagated by active dissolution in the matrix, susceptibilities of the alloys depend upon the proportion of the matrix area. Volume fractions of the matrix phase in the alloys are about 20% in the W-10 alloy and about 5% in the W-3 alloy. Since the W-3 alloy has a small matrix volume and high tungsten contiguity, cracks cannot grow even though severe dissolution occurs in the matrix area.

Results of the influence of electrochemical polarization on the SCC of the W-10 alloy in NaCl solution suggest that both anodic and cathodic polarization can be detrimental.

When a sample is anodically polarized from the corrosion potential, dissolution and oxidation are enhanced. The polarization creates a sufficient potential difference across the film to allow for outward migration of cations through the film. Once this has happened, the film is destroyed, resulting in severe dissolution and therefore, faster crack propagation.

Cathodic polarization decreases the free energy for dissolution and the oxidation reaction. As the equilibrium potential is approached, the overpotential for oxide film growth decreases.

Cathodic polarization also enhances both hydrogen and oxygen reduction. The rate of the oxygen reduction

reaction quickly becomes diffusion limited with 200 mV of cathodic polarization. Further polarization (at -1.0 V vs. SCE) brings the hydrogen reduction reaction. Since the rate of the hydrogen reduction reaction is governed by the hydrogen over potential, more negative cathodic polarization yields higher rate of hydrogen reduction, and therefore increases the hydrogen surface coverage.

Results of polarization effects on the stress corrosion cracking behavior in aerated 3% NaCl solution are presented in Figure 16. At -0.2 V vs. SCE, which is in the active dissolution region,  $K_{ISCC}$  and the crack growth rate remain the same as for the case of the open-circuit potential. When the specimen was polarized to +0.2 V vs. SCE, which is in the passive region,  $K_{ISCC}$  was remarkably lowered while the crack growth rate in the plateau did not change. When the specimen was polarized to -1.2 V vs. SCE, which is in the hydrogen evolution region, the crack growth rate in the plateau was increased.

The constancy of the crack growth rate in the plateau is consistent with mass transport controlled reactions. In other words, the rate limiting reactions in the plateau region are the same in all three cases of open-circuit potential and anodic potentials.

The decrease in  $K_{ISCC}$  at +0.2 V vs. SCE can be explained by passive film formation on the crack surface.

For SCC propagation to occur by mechanisms involving interaction of the alloy with the environment, film breakdown must occur. Breakdown may occur in two ways: (1) by chemical breakdown, and (2) by mechanical rupture. Chemical breakdown arises when pitting or crevice corrosion are initiated on filmed surfaces. Mechanical rupture arises when slip processes in the adjacent metal break the film and expose fresh, unfilmed metal to the solution. In this alloy, pitting or crevice corrosion are not observed. Therefore, the passive film is thought to be ruptured by localized plastic deformation at the crack tip, permitting rapid anodic dissolution of the exposed matrix while the non-deforming crack walls remain protected by the film, as shown in Figure 3. The potential difference between filmed and unfilmed surfaces could constitute a strong driving force for the dissolution.

Furthermore, since anodic dissolution occurs only at the crack tip, sharp cracks can be formed and propagate at lower  $K_I$ . However, in the cases of -0.2 V vs. SCE and open-circuit potential, general corrosion occurs not only at the crack tip but all over the crack surface, as shown in Figure 48. Hence, the crack front is easily blunted, preventing crack from propagation even at higher  $K_I$ .

The increase in the plateau crack growth rate



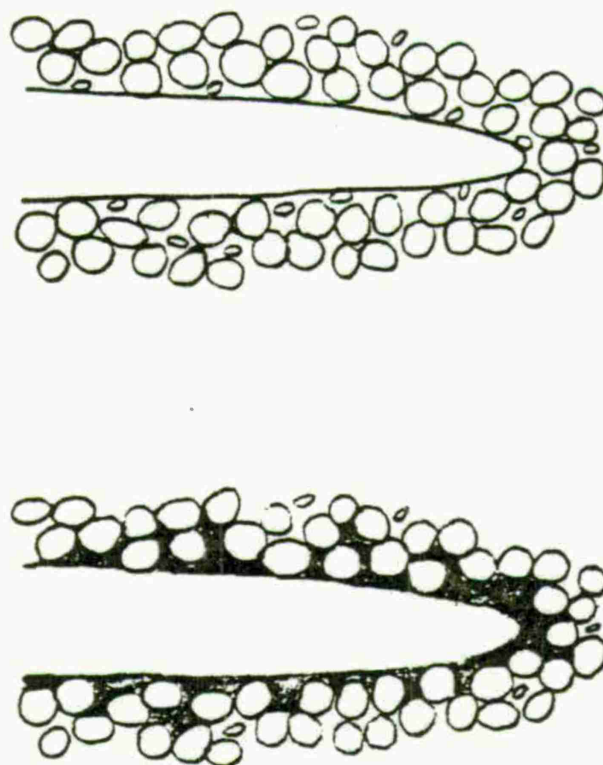


Figure 48      Schematic of the Crack Blunting by Anodic Dissolution in the Matrix of the Crack Surface Due to the Lack of Passive Film.

at -1.2 V vs. SCE results from different mass transport processes and kinetics. At the open-circuit potential and anodic potentials, which are above the potential for hydrogen evolution, cracks propagate by the repetition of the following processes:

(1) Oxidation of metals:  $M \rightarrow M^{++} + 2e^{-}$

(2) diffusion of oxygen into the crack

(3) Oxygen reduction reaction:



(to consume electrons produced by reaction (1))

(4) diffusion of  $M^{++}$  out of the crack tip to expose fresh metal surface to the surface.

At -1.2 V vs. SCE, the following processes are necessary for cracks to propagate:

(1) diffusion of  $H^{+}$  to the crack tip

(2) adsorption of H:  $H^{+} + e^{-} \rightarrow H_{ads}$

(3) absorption of H:  $H_{ads} \rightarrow H_{abs}$

(4) diffusion of H to the tungsten-matrix interface ahead of the crack tip.

It is difficult to say which step is rate controlling for either case because of the lack of electrochemical kinetic data for this system. However, the case of transport of  $M^{++}$  away from the crack tip limiting the

rate of anodic dissolution and transport of  $H^+$  to the crack tip limiting the rate of hydrogen reduction and subsequent interface embrittlement might explain the observed plateau crack growth rates. The larger  $M^{++}$  ion diffuses down the crack more slowly than the  $H^+$  ion. Therefore, the dissolution limiting rate is less than the hydrogen production limiting rate. Assuming that approximately equivalent extents of reaction result in equivalent crack advance, this means the limiting crack growth rate due to anodic dissolution is less than that for the case of hydrogen embrittlement.

The result, Figure 49 indicates that the crack growth rate in the plateau region is independent of the specific anion present and its aggressiveness, when the specimen is cathodically polarized at  $-1.2$  V vs. SCE. Thus, the presence of hydrogen in the specimen may be sufficient to cause significant increase in the crack growth rate in the plateau region. This result would be expected because film formation on the surface is impossible at that potential, and therefore a bare surface exists at the crack tip in both chloride and sulfate solutions.

The immunity of the W-3 alloy to SCC in NaCl solution at anodic potentials is probably due to its small volume fraction of matrix phase and high tungsten contiguity. Since the W-3 alloy has a much smaller matrix volume and higher tungsten

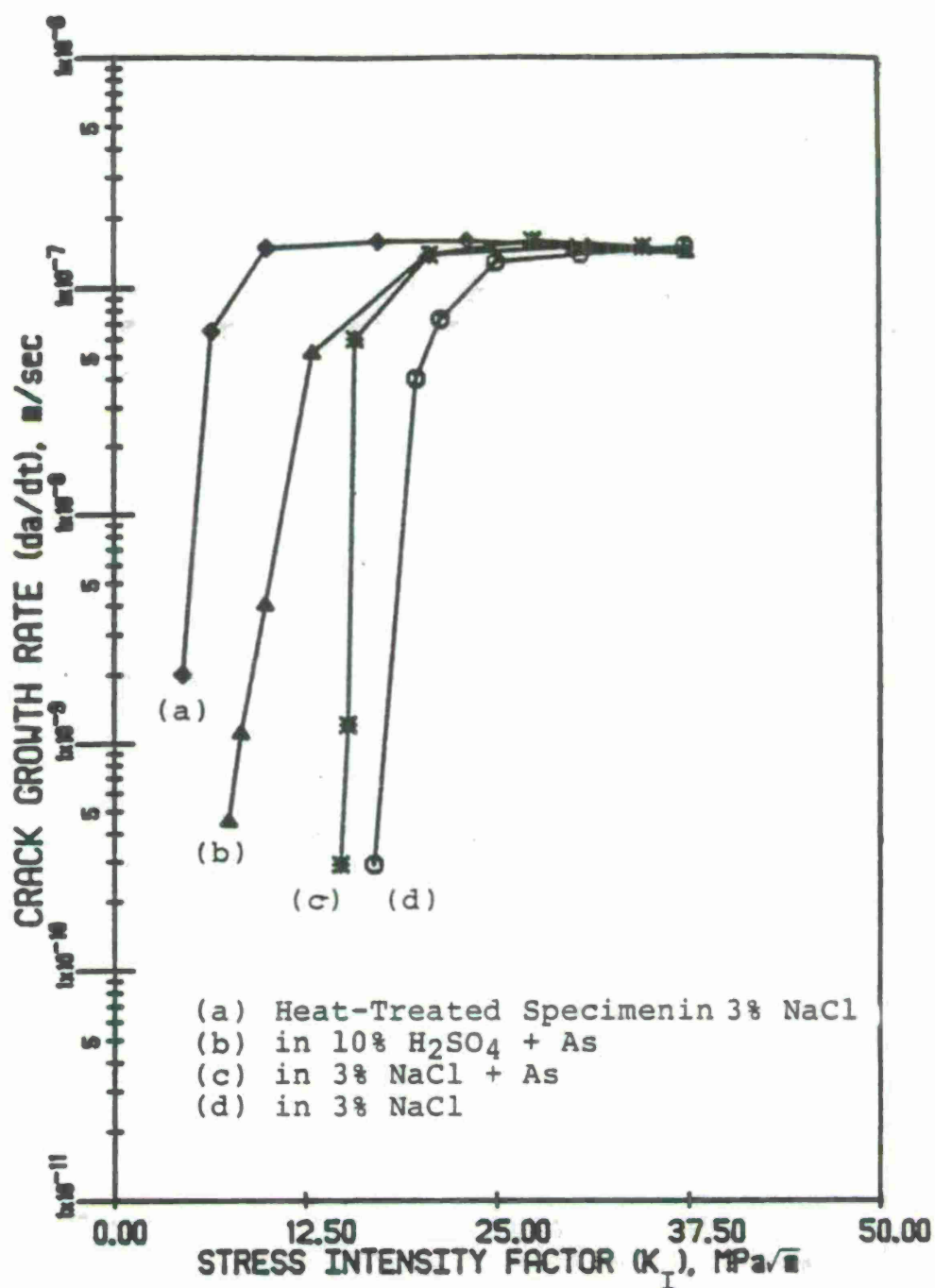


Figure 49  $K_I$  - da/dt Curves Showing That Crack Growth Rate in the Plateau Region is Independent of the Specific Anion Present and its Aggressiveness, at -1.2 V vs. SCE.



contiguity, cracks cannot grow even though severe dissolution occurred in the matrix, as seen in Figure 19. Hence, cracks are blunted rather than advancing. Electrochemical polarization curve, Figure 14, also provides some explanation of the immunity. Since the critical current density and current density at passivity is very high (about 100 times greater than for the W-10 alloy), passive film formation is very difficult and effectiveness of the passive film formed in preventing metal dissolution is poor. Therefore, the film cannot serve as an effective barrier against  $\text{Cl}^-$ , only severe dissolution occurs.

The immunity of the W-3 alloy to SCC in NaCl solution at cathodic potentials may be related to the small matrix volume and the inability of the tungsten-matrix interfaces to accept hydrogen because of microstructural constraints. Since the W-3 alloy has very small matrix volume and hydrogen diffuses mostly through the tungsten particles, as Powell pointed out, it is very difficult for the hydrogen to accumulate in the tungsten-matrix interfaces to cause hydrogen embrittlement.

Even if hydrogen may be concentrated in the interfaces and reduce their strength, cracks can not grow because of small tungsten-matrix interfaces.

## 5.2 Effects of Hydrogen Catalyst

The results (Figure 22) show that the addition of a hydrogen catalyst (As) to NaCl solution decreased  $K_{ISCC}$  of the W-10 alloy. The decrease is of further significance because the hydrogen catalyst addition slowed the hydrogen evolution reaction, as shown in Figure 20. Therefore, it is evident that the hydrogen catalyst increased the surface coverage of atomic hydrogen on the specimen, compensating the reaction rate decrease. This increased atomic hydrogen on the specimen surface could also increase the rate of hydrogen permeation into the material.

As seen in Figure 23, the W-10 alloy showed a lower  $K_{ISCC}$  in 10%  $H_2SO_4$  containing As than in 3% NaCl containing As. Moreover, the W-3 alloy showed crack propagation only in 10%  $H_2SO_4$  containing As. From these observations, it can be deduced that As acts as a more effective hydrogen entry catalyst in the acidic solution than in a neutral solution.

## 5.3 Effects of Heat Treatment

The experimental results show that the heat treatment in a hydrogen atmosphere decreased SCC resistance of the W-10 alloy. It has been pointed out<sup>52</sup> that HE requires the development of a critical hydrogen concentration at the stress concentration sites. It has also been

reported<sup>18,19</sup> that heat treatment in a hydrogen atmosphere causes strength and ductility degradation of this alloy. Heat treatment in a hydrogen atmosphere will introduce a certain amount of hydrogen into the specimen. Therefore, it takes shorter time for the heat treated specimen to attain the critical hydrogen concentration at the crack tip than for the as-received one, during the cathodic charging. Therefore, the heat treated specimen exhibits faster crack propagation. Furthermore, the dissolved hydrogen embrittles the strength of the matrix-tungsten interfaces so that cracks can propagate at a lower  $K_I$ .

Since the solubility of hydrogen in tungsten<sup>79</sup> is much lower than the solubility of hydrogen in nickel<sup>80</sup> or iron,<sup>81</sup> hydrogen in this two phase alloy would probably be concentrated in the matrix phase and/or at the tungsten-matrix interfaces. The presence of hydrogen at the interface is thought to reduce the strength of the interface, facilitating crack propagation. This can be deduced from scanning electron fractography. The as-received tension specimen failed by rupture of the matrix with cleavage of the tungsten grains and separation of tungsten-tungsten grain boundaries. However, the hydrogen embrittled alloy failed by separation of tungsten-matrix and tungsten-tungsten interfaces and cleavage of some tungsten particles.

When the matrix-tungsten interface is strong,

the matrix configuration around the tungsten particle is such that the matrix is put into a stress state with multi-axial components, as shown in Figure 50. The flow stress in the matrix is thus raised as the result of this plastic constraint. The strength increase and localized strain are sufficient to cause the tungsten particles to fail in transcrystalline cleavage. As soon as a tungsten particle cracks, the crack acts as a sharp notch in the highly stressed matrix surrounding the particle, leading to a knife edge failure in the matrix.

When the matrix-particle interface is weakened by hydrogen, however, there is an early separation of tungsten-matrix interfaces. Tungsten contiguity leads to tungsten-tungsten grain boundary failure. The matrix can neck down and rupture independent of the tungsten particles.

#### 5.4 Effects of Alloy Composition

The heat treated W-3 did not exhibit SCC susceptibility in NaCl solution, under any conditions, even though the chemical composition of the matrix was altered substantially, as seen in Table 4. Hence, the SCC susceptibility does not depend upon the chemical composition of the matrix produced by heat treatment.

In an attempt to examine, the influence of overall tungsten content on SCC behavior, slow strain rate tests



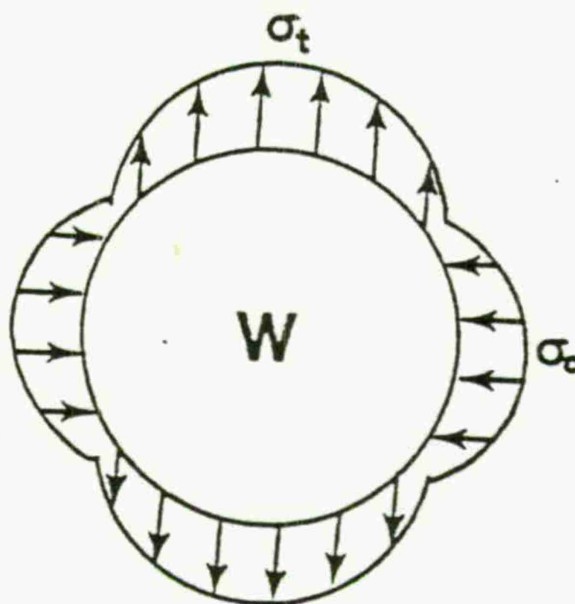


Figure 50 Schematic Representation of Stresses Around a Tungsten Grain from the Matrix During Tensile Testing.<sup>3</sup>

were conducted on pure tungsten wire. A description of experimental procedure and results are presented in Appendix I. As shown in Table 5 and Figure 51, pure tungsten is immune to SCC in aerated 3% NaCl solution. Therefore, the overall tungsten content in the alloy may be an important factor determining SCC susceptibility in NaCl solution.

As seen in Table 3 and 4, the W-3 alloy has a considerable amount of copper in the matrix, but the W-10 alloy does not. Moreover, only the W-10 alloy exhibited SCC propagation in NaCl solution. Hence, it is worthwhile to examine effects of copper on SCC behavior. In order to qualitatively examine, SCC initiation tests were conducted on the copper diffused W-10 alloy and heat treated W-10 alloy specimens. Details of the experimental procedure and results are given in Appendix II and III. At an applied  $K_I$  of  $19.7 \text{ MPa}\sqrt{\text{m}}$ , only the copper diffused specimen exhibited crack initiation and propagation in aerated 3% NaCl solution. The heat treated W-10 alloy did not exhibit crack initiation even at  $K_I$  of  $35.0 \text{ MPa}\sqrt{\text{m}}$ . Crack initiation and propagation in the copper diffused W-10 alloy may occur by mechanical rupture of the copper layer at the root of the notch in the specimen. Once this happens, cracks initiate and propagate by dissolving the matrix. The copper surface layer is thought to act as an efficient cathode, increasing the rate of matrix dissolution as compared to

specimens lacking the copper surface. In addition the copper surface layer concentrates all of the anodic dissolution at the exposed matrix in the notch root. Coupling the increased dissolution rate with the concentration effect leads to cracking by dissolution of the matrix at the notch root instead of general matrix attack seen in specimens without the copper surface.

In the W-3 alloy, however, copper exists in the matrix as one component of a nickel based solid solution. There are no large clumps of pure copper to act as efficient cathodic sites. Since the copper is equally distributed throughout the matrix, there is no concentration of the anodic dissolution reaction to any particular region of the matrix. As a result, only extensive general attack of the matrix is observed.

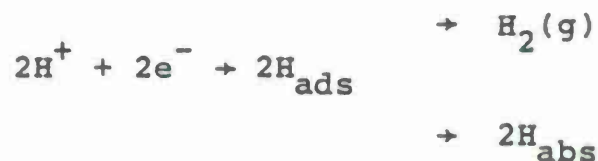
### 5.5 Sulfide Stress Cracking

The results, Figures 29 and 30 show that both the W-10 and W-3 alloys are susceptible to SCC in the sulfide cracking solution. Sulfide stress cracking of the W-3 alloy occurs primarily by cleavage of the tungsten grains and dimple formation in the matrix, whereas the fracture morphology of the W-10 alloy remains the same as that observed in aerated 3% NaCl solution. Although the W-3 alloy shows crack propagation, it has a much higher  $K_{ISCC}$  and slower crack growth rate than that of the W-10 alloy.

It has been suggested that sulfide stress cracking is a form of hydrogen embrittlement<sup>82-85</sup>. hydrogen is present due to the corrosion of the alloy in the acidic environment. At the corrosion potential, the dissolution of the matrix,



is accompanied by the cathodic reaction,



The hydrogen atoms which are produced at the specimen surface may recombine to form  $H_2$  or may be adsorbed by the specimen as atomic hydrogen. It is also suggested that the  $H_2S$  acts to poison the recombination reaction, thus facilitating hydrogen entry.

In both alloys, cracks are thought to propagate as a result of hydrogen embrittlement where the hydrogen was made available by an  $H_2S$  corrosion.  $H_2S$  is thought to enhance dissolution of the alloy, and increases the relative amount of hydrogen absorption.

In the W-10 alloy, hydrogen may accumulate in the tungsten-matrix interfaces near the crack tip and reduce



the strength of the interfaces. Hence, cracks propagate along the phase boundaries. In the W-3 alloy, hydrogen may accumulate in internal pores and form high pressure bubbles. The high pressure bubbles exerts an internal stress to assist fracture.

### 5.6 Mechanisms

Optical micrograph, Figure 17 and fractographs, Figure 33 strongly suggest that SCC of the W-10 alloy at the open-circuit potential in NaCl solution occurs by dissolution of the matrix. The matrix and tungsten phases are thought to form an electrochemical cell, where the matrix serves as an anode and the tungsten grains as a cathode. Hence, stress corrosion cracks propagate at the expense of active dissolution in the matrix. Small matrix volume fraction and high tungsten contiguity in the W-3 alloy prevents cracks from growing even though severe matrix dissolution occurs.

The observed susceptibility of both alloys to cracking in the NACE recommended sulfide cracking solution and when cathodically charged in 10%  $H_2SO_4$  with As indicates that both alloys are highly susceptible to hydrogen embrittlement. Scanning electron fractographs, Figures 41 and 45 show that fracture of the W-10 alloy occurred primarily by separation of the tungsten-matrix interfaces. This means that dissolved hydrogen may be concentrated

at the interfaces in the vicinity of the crack tip by lattice diffusion, dislocation sweeping, and the large amount of deformation associated with crack tip stress and strain concentrations. When the concentration at the interface reaches a critical concentration, it reduces the strength of the interface, facilitating crack propagation.

Fractographs of the W-3 alloy, Figures 42 and 46 demonstrate that crack propagation of the alloy proceeded primarily by dimple formations in the matrix and cleavage of the tungsten particles. Therefore, it is suggested that hydrogen may accumulate in internal microvoids and form high pressure hydrogen bubbles, exerting an internal stress to assist fracture of the alloy.

In summary, the following mechanisms are suggested for the alloys:

1) Anodic dissolution mechanisms:

For the W-10 alloy at the open-circuit potential and anodic potentials in NaCl solution.

2) Hydrogen embrittlement (Decohesion model):

For the W-10 alloy in the NACE sulfide cracking solution and when cathodically charged in NaCl solution and 10%  $H_2SO_4$  solution containing As.

3) Hydrogen embrittlement (High pressure bubble formation model):

For the W-3 alloy in the NACE sulfide cracking solution and when cathodically charged in 10%  $\text{H}_2\text{SO}_4$  solution containing As.

## PART 6

### CONCLUSIONS

1. In the W-10 alloy, SCC in 3% NaCl solution propagates with separation of tungsten-tungsten interfaces and ductile rupture of the matrix. However, the W-3 alloy is not susceptible to SCC in NaCl solution.

In both alloys, severe corrosion takes place primarily in the matrix area. The matrix and tungsten phases are thought to form an electrochemical cell, where the matrix area serves as the anode and the tungsten grain as a cathode. Hence, stress corrosion cracks propagate at the expense of active dissolution in the matrix. Since the W-3 alloy has a small matrix volume and high tungsten contiguity, cracks cannot grow even though dissolution occurs severely in the matrix area.

2. Under constant loading condition, the W-3 alloy does not show crack initiation and fracture until a load level of the order of the UTS is applied.

Under slow strain rate testing in NaCl solution, pure tungsten shows the same stress-strain curve as in air. Therefore, tungsten contiguity is thought to be a very important factor determining SCC susceptibility in NaCl solution. The higher is tungsten contiguity of the material, the less susceptible it is to SCC.

3. Polarization lowers resistance of the W-10



alloy to SCC in NaCl solution. Cathodic polarization increases the crack propagation kinetics substantially when compared to the open-circuit potential. Thus, this alloy is believed to be highly susceptible to HE, although the fracture morphology remains unchanged from SCC.

Polarization does not cause SCC propagation of the W-3 alloy in NaCl solution.

4. The addition of a hydrogen catalyst (As) in the NaCl solution further decreases the SCC resistance of the W-10 alloy but does not bring crack propagation of the W-3 alloy.

5. Heat treatment in a hydrogen atmosphere increases SCC susceptibility of the W-10 alloy, whereas heat treatment in argon has no effect on SCC susceptibility.

Heat treatments of the W-3 alloy do not result in crack propagation in 3% NaCl solution even though the chemical compositions in the matrix were substantially altered.

6. Copper in these alloy systems has a deleterious effect on SCC resistance.

7. Both the W-10 and W-3 alloys are susceptible to SCC in the sulfide cracking solutions, and also show SCC propagation when cathodically charged in 10%  $H_2SO_4$  + As.

In these solutions, SCC of the W-3 alloy occurs

primarily by cleavage of the tungsten grains and dimple formation in the matrix, whereas the fracture morphology of the W-10 alloy remains the same as that observed in NaCl solution. Although the W-3 alloy shows crack propagation, it has a much higher  $K_{ISCC}$  and slower crack growth rate than that of the W-10 alloy.

Both alloys are thought to be susceptible to HE in these solutions.

## PART 7

### SUGGESTIONS FOR FUTURE WORK

It is suggested to perform SCC tests with a series of tungsten heavy alloys having same alloying elements but different compositions.

- Study effects of compositions on the SCC susceptibility.
- Study the dependence of SCC susceptibility on the matrix volume fraction.
- Study post-sintering heat treatment effects.
- Perform both constant displacement and constant load tests on the modified WOL specimens of the same general design.
- Compare the  $K_{ISCC}$  value and crack growth rate performance.

## PART 8

### REFERENCES

1. D.J. Jones and P. Munnery: Powder Metall., 1967, Vol. 10, pp. 156-173.
2. H. Takeuchi: J. Jap. Inst. Metals, 1967, Vol. 31, pp. 1064-1070.
3. K.S. Churn and R.M. German: Met. Trans., 1984, Vol. 15A, pp. 331-338.
4. K.S. Churn and D.N. Yoon: Powder Metall., 1979, Vol. 22, pp. 175-177.
5. E. Ariel, J. Barta, and D. Brandon: Powder Metall. Int., 1973, Vol. 5, pp. 126-129.
6. L.G. Bazhenova, A.D. Vasilev, R.V. Minakova, and V.I. Trefilov: Soviet Powder Metall. Met. Ceram., 1980, Vol. 19, pp. 34-38.
7. G.H.S. Price, C.J. Smithells, and S.V. Williams: J. Inst. Metals, 1938, Vol. 62, pp. 239-54.
8. E.G. Zukas and H. Sheinberg: Powder Technol., 1976, Vol. 13, pp. 85-96.
9. F.H. Ellinger and W.P. Sykes: Trans. ASM, 1940, Vol. 28, pp. 619-42.
10. G.C. Kuczynski: J. Met. Trans., 1949, Vol. 1, pp. 301-303.
11. Conyers Herring: J. Appl. Phys., 1950, Vol. 21, pp. 301-303.
12. H.S. Cannon and F.V. Lenel: Plansee Proc., Metallwerk Plansee G.m.b.He, Reutte/Tyrol, 1953, pp. 106-122.
13. A.N. Niemi, L.E. Baxa, J.K. Lee, and T.H. Courtney: Modern Developments in Powder Metallurgy, H.H. Hausner, H.W. Hausner, H.W. Antes, and G.D. Smith, eds., Metal Powder Industries Federation, Princeton, NJ, 1981, Vol. 12, pp. 483-95.
14. D.V. Edmonds and P.N. Jones: Met. Trans., 1979, vol. 10A, pp. 289-295.



15. R.V. Minakova, A.N. Pityankevich, O.K. Teodorovich, and I.N. Frantsevich: Soviet Powder Met. Meal Ceram., 1968, Vol. 7, pp. 396-99.
16. E.-T. Henig, H. Hofmann, and G. Petzow: Proceedings of the 10th Plansee-Seminar, H.M. Ortner, ed., Metallwerk Plansee, Reutte, Austria, 1981, Vol. 2, pp. 335-59.
17. R.M. German and J.E. Hanafée: Processing of Metal and Ceramic Powders, R.M. German and K.W. Lay, eds., TMS-AIME, Warrendale, PA, 1982, pp. 267-82.
18. H.K. Yoon, S.H. Lee, S.-J.L. Kang and D.N. Yoon: J. Mater. Sci., 1983, Vol. 18, pp. 1374-80.
19. F.E. Sczerenie and H.C. Rogers: Hydrogen in Metals, Ed. by I.M. Bernstein and A.W. Thompson, 1974, pp. 645-655.
20. T.K. Kang, E.-T. Henig, W.A. Kaysser, and G. Petzow: Modern Developments in Powder Metallurgy, H.H. Hausner, H.W. Antes, and G.D. Smith, eds., Metal Powder Industries, Princeton, NJ, 1981, Vol. 14, pp. 1127-34.
21. D.G. Branodn, E. Ariel, and J. Barte: Proc. 5th Intl. Symposium on Electron Microscopy and Structure of Materials, Berkeley, CA, 1971, pp. 849-858.
22. E.A. Steigerwald: Proceedings of the ASTM, Vol. 60, 1960, pp. 750-760.
23. H.H. Johnson and A.M. Willner: Applied Materials Research, Jan. 1965, pp. 34-40.
24. C.F. Tiffany and J.N. Masters: Fracture Toughness Testing and Its Applications (ASTM STP 381), 1965, pp. 249-277.
25. S.R. Novak and S.T. Rolfe: J. of Materials, Vol. 4, No. 3, 1969 p. 701.
26. B.F. Brown and C.D. Beachem: "A Study of the Stress Factor in Corrosion Cracking by Use of the Precracked Cantilever-Beam Specimen", Corrosion Science, Vol. 5, 1965, pp. 745-750.
27. B.F. Brown: "A New Stress-Corrosion Cracking Test for High Strength Alloys", Materials Research and Standards, Vol. 6, No. 3, 1966, pp. 129-133.

28. M.J. Manjoine: "Biaxial Brittle Fracture Tests", Journal of Basic Engineering Transactions, ASME, 1965, pp. 293-298.
29. M.J. Manjoine: Plane-Strain Crack Toughness Testing of High Strength Metallic Materials (ASTM STP 410), 1967, pp. 66-70.
30. E.T. Wessel: Engineering Fracture Mechanics, Vol. 1, 1968, pp. 77-103.
31. R.W. Staehle: Stress-Corrosion Cracking and Hydrogen Embrittlement of Iron-Base Alloys, p. 180, NACE, Houston, 1977.
32. F.A. Champion: Symposium on Internal Stressses in Metals and Alloys, p. 468, Inst. of Metals, London, 1948.
33. H.L. Logan: J. Res. Natn. Bur. Stand., 1952, Vol. 48, p. 99.
34. Scully, J.C., Kinetic Features of Stress Corrosion Cracking, Corrosion Science, Vol. 7, 1967, pp. 197-208.
35. J.C. Scully: The Electrochemical Parameters of Stress Corrosion Cracking, Corrosion Science, Vol. 8, 1968, pp. 513-524.
36. H.W. Pickering and P.R. Swann: Corrosion, 1963, Vol. 19, p. 373t.
37. P.R. Swann and J.D. Embury: High Strength Materials p. 327. John Wiley and Sons, Inc., New York, 1965.
38. N.J. Petch, Phil. Mag., Vol. 1, 331 (1956).
39. H. Nichols and W. Rostoker: Acta. Met., 1961, Vol. 9, p. 504.
40. R.J.H. Wanhill: Corrosion, 1975, Vol. 31, p. 66.
41. H.H. Uhlig: Physical Metallurgy of Stress Corrosion Fracture, p. 1, Interscience New York, 1959.
42. E.G. Coleman, D. Weinstein, and W. Rostoker: Acta. Met., 1961, Vol. 9, p. 491.
43. A.J. Forty and P. Humble: Phil. Mag., L963, Vol. 8, p. 247.

44. A.J. McEvily, Jr., and A.P. Bond: J. Electrochem. Soc., 1965, Vol. 112, p. 141.
45. E.N. Pugh: Stress Corrosion Cracking and Hydrogen Embrittlement of Iron-Base Alloys, p. 37, NACE, Houston, 1977.
46. A.J. Forty: Physical Metallurgy of Stress Corrosion Fracture, p. 99, Interscience, New York, 1959.
47. J. Vokl and G. Alefeld: Diffusion in Solids-Recent Developments, Academic Press, New York, Ed. by A.S. Nowick and J.J. Burton, 1975, p. 272.
48. M.R. Louthan, G.R. Caskey, J.A. Donovan, and D.E. Rawl: Mat. Sci., and Eng., 10 (1972), p. 357.
49. J.K. Tien: Effect of Hydrogen on Behavior of Materials, AIME, New York, Ed. by A.W. Thompson and I.M. Bernstein, 1976, p. 309.
50. J.D. Frandsen and H.L. Marcus: Effect of Hydrogen on Behavior of Materials, AIME, New York, Ed. by A.W. Thompson and I.M. Bernstein, 1976, p. 233.
51. A.W. Thompson and I.M. Bernstein: Advances in Corrosion Science and Technology (R.W. Staehle and M.G. Fontana, eds.), Vol. 7, Plenum, New York.
52. H.K. Birnbaum and H. Wadley: Scripta Met., Vol. 9, 1975, p. 1113.
53. J.C.M. Li, R.A. Oriani and L.S. Darken, Zeits. fur Phys. Chem., 1966, Vol. 49, pp. 271-90.
54. R.A. O'Brien: Ber. Bunsenges fur Phys. Chem., 1972,, Vol. 76, pp. 848-57.
55. C. Zappfe and C. Sims: Trans. AIME, 1941, Vol. 145, pp. 225-59.
56. C.P. Beachem: Met. Trans., 1972, Vol. 3, pp. 43751.
57. J.P. Hirth and H.H. Johnson: Corrosion, 1976, Vol. 32, pp. 3-15.
58. D.G. Westlake, Trans. ASM, 62 (1969) p. 1000.
59. A.W. Thompson, Hydrogen in Metals, ASM, Ed. by I.M. Bernstein and A.W. Thompson, 1974, p. 91.



60. A.W. Thompson and J.A. Brooks: Met. Trans. 6A (1975), p. 1431.
61. I.M. Bernstein, R. Garber and G. Pressouyre: Effect of Hydrogen on Behavior of Metals, AIME, New York, Ed. by. A.W. Thompson and I.M. Bernstein, 1976.
62. S. Gahr, M.L. Grossbeck and H.K. Birnbaum: Acta. Met., Vol. 25, 1977, p. 125.
63. T.M. Devine: Scripta Met., Vol. 10, 1976, p. 447.
64. ASTM Standards, Part I-B, 1946.
65. D.M. Fisher, R.T. Bubsey, and J.E. Srawley: "Design and Use of Displacement Gage for Crack Extension Measurements", Technical Note D-3724, NASA, Nov. 1966.
66. J.B. Greer: Interlaboratory Sulfide Stress Cracking Results Using the T-1F-9 Proposed Test Method, Paper No. 97, presented at Corrosion/75, Toronto, Ontario, April, 1975, NACE.
67. ASTM Standards G5-72.
68. B.C. Muddle: Interphase Boundary Precipitation in Liquid Phase Sintered W-Ni-Fe and W-Ni-Cu Alloys, Met. Trans., 1984, Vol. 15A, pp. 1089-98.
69. J.F. Newman and L.L. Shreir: Corrosion Science, Vol. 9, 1969, pp. 631-641.
70. R.D. McCright and R.W. Staehle: J. Electrochem. Soc., Vol. 121, 1974, pp. 609-618.
71. R.V. Minakova, N.A. Storchak, P.A. Verkhovodov, L.G. Bazhenova, and V.L. Poltoratskaya: Soviet Powder Metall. Met. Ceram., Dec. 1980, Vol. 19, pp. 842-846.
72. G.L. Powell: Analytical Chemistry, Vol. 44, No. 14, Dec. 1972, pp. 2357-2361.
73. Metals Handbook, 8th Edition, Vol. 2, p. 259.
74. Metals Handbook, 8th Edition, Vol. 2, p. 424.
75. M. Arita, M. Tanaka, J.S. Goto, and M. Someno: Metall. Trans., 1981, Vol. 12A, pp. 497-504.



76. H. Helfmeier and M. Feller-Kniepmeier: J. Appl. Phys., Vol. 41, No. 8, 1970, pp. 3202-5.
77. Metals Handbook, 8th Edition, Vol. 2, p. 485.
78. J.W. Koger: "Corrosion of Tungsten-3.5 Nickel-1.5 Iron and Its Constituent Phases in Aqueous Chloride Solutions", Paper No. 42, Corrosion/75, NACE, Houston, TX, 77001, 1975, p. 14.
79. R. Frauenfelder: J. Vac. Sci. Technol., Vol. 6, 1969, p. 388.
80. A. Sieverts: Z. Metallk., Vol. 21, 1929, p. 37.
81. A. Sieverts: Z. Phys. Chem. (Peipzig), Vol. 77, 1911, p. 591.
82. R.L. McGlasson and W.D. Greathouse: Corrosion, Vol. 15, 1959, p. 437.
83. D. Warren and G.W. Beckman: Corrosion, Vol. 13, 1957, p. 33.
84. B.J. Berkowitz and H.H. Horowitz: J. Electrochem. Soc., Vol. 129, 1982, pp. 468-474.
85. B.J. Berkowitz and F.H. Heubaum: Corrosion, Vol. 40, No. 5, 1984, pp. 240-245.

## PART 9

### APPENDIX I

#### SLOW STRAIN RATE TESTS

In an effort to examine overall tungsten content influence on the SCC behavior, slow strain rate tests were conducted on pure tungsten wire. The material was purchased from Alfa Products. For stress relieving,<sup>73</sup> the wire was heat treated at 1040°C in argon atmosphere for 1 hr, and furnace cooled.

Diameter and gage length of the wire specimen was 0.75 mm and 2.8 in, respectively. Specimens were loaded at a strain rate of  $40 \times 10^{-6} \text{ s}^{-1}$  to 100 lbs. and then to fracture at the constant strain rate of  $4 \times 10^{-6} \text{ s}^{-1}$ . The tests were performed in the air as a baseline and aerated 3% NaCl solution.

The test results are summarized in Table 5, and the stress strain curves are presented in Figure 51. No significant differences exist between the two test results.

Table 5

## Results of Slow Strain Rate Tests on Pure Tungsten

Test Media	UTS (ksi)	YS (ksi)	Elongation (%)	Time to Failure (hrs.)
Air	182	152	5.1	4.3
3% NaCl	179	147	5.1	4.3

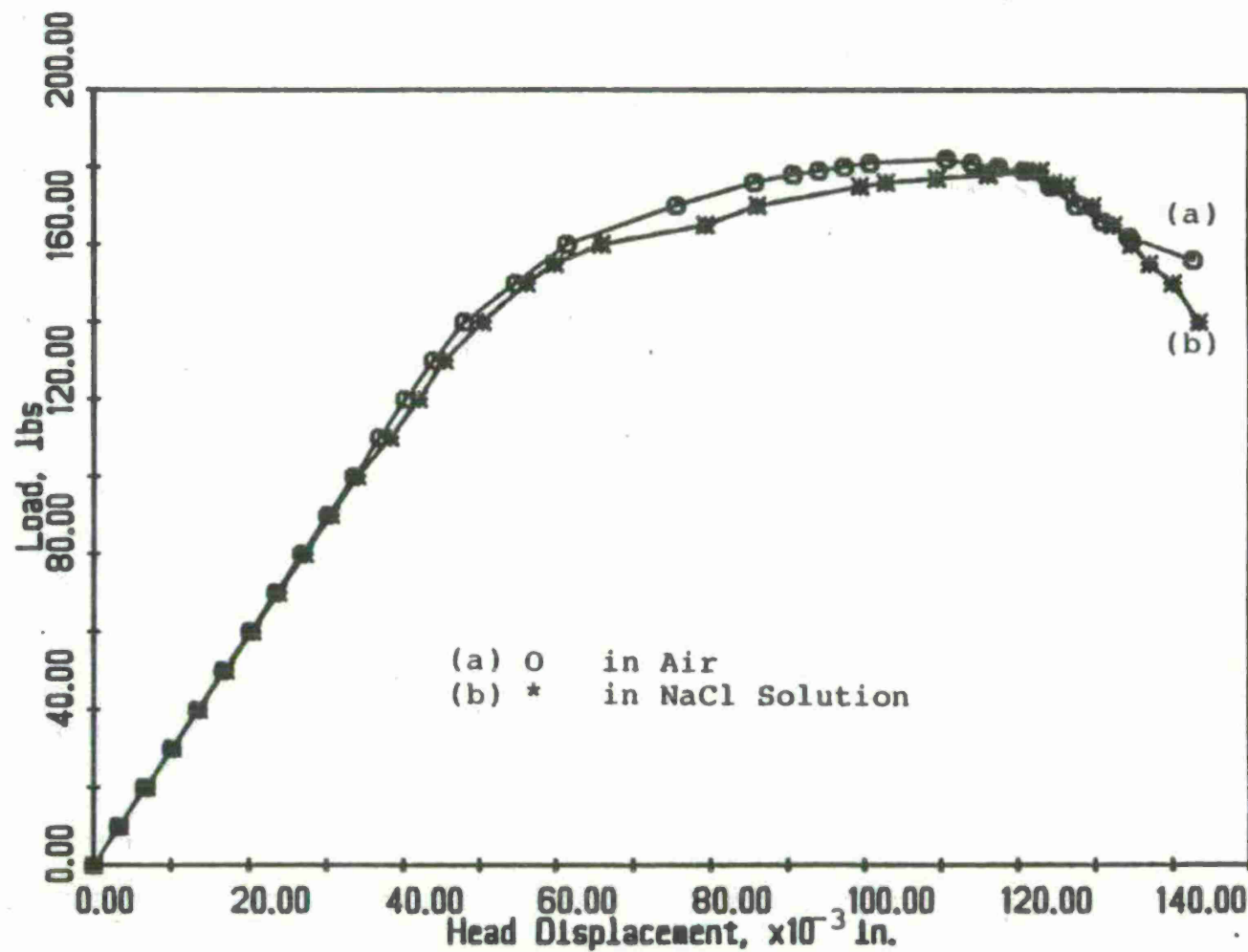


Figure 51 Load vs. Displacement Curves from Slow Strain Rate Tests of Pure Tungsten in Air and 3% NaCl Solution.



## APPENDIX II

## CRACK INITIATION TESTS

In order to qualitatively examine copper effects on the SCC behavior, SCC initiation tests were conducted on the W-10 alloy specimens. Electroplating<sup>74</sup> of copper was performed on the modified WOL specimen until the final electroplated copper layer was 1 mil thick. The electroplating condition is described in Appendix III.

Following the electroplating, heat treatment was carried out to diffuse copper into the base material at 1050°C for 120 hrs in the evacuated silica tube. Since copper has diffusion coefficient of  $10^{-11}$  cm<sup>2</sup>/sec in this alloy system at 1050°C. Since the resulting depth of copper penetration is so shallow (about 40 μm), the remaining copper layer on the specimen was removed electrochemically.<sup>77</sup>

To see the copper effects only on the SCC initiation behavior, tests were performed on both the copper diffused W-10 alloy specimen and the W-10 alloy which was heat treated at the same condition. If there was no initiation at a  $K_I$  after 200 hrs testing, tests were performed at higher  $K_I$  until the crack initiates.

At the applied  $K_I$  of 19.7 MPa√m, only the copper diffused specimen showed crack initiation and propagation in less than 20 hours in aerated 3% NaCl solution. Optical

micrograph of the specimen is shown in Figure 52. Figure 53 shows the fractography of the specimen. Fracture occurred through separation of tungsten-matrix interfaces and rupture of the matrix. Existence of Cu on the fracture surface was confirmed by EDAX, as shown in Figure 54. The heat treated W-10 alloy did not show crack initiation even at the  $K_I$  of  $35.0 \text{ MPa}\sqrt{\text{m}}$ .

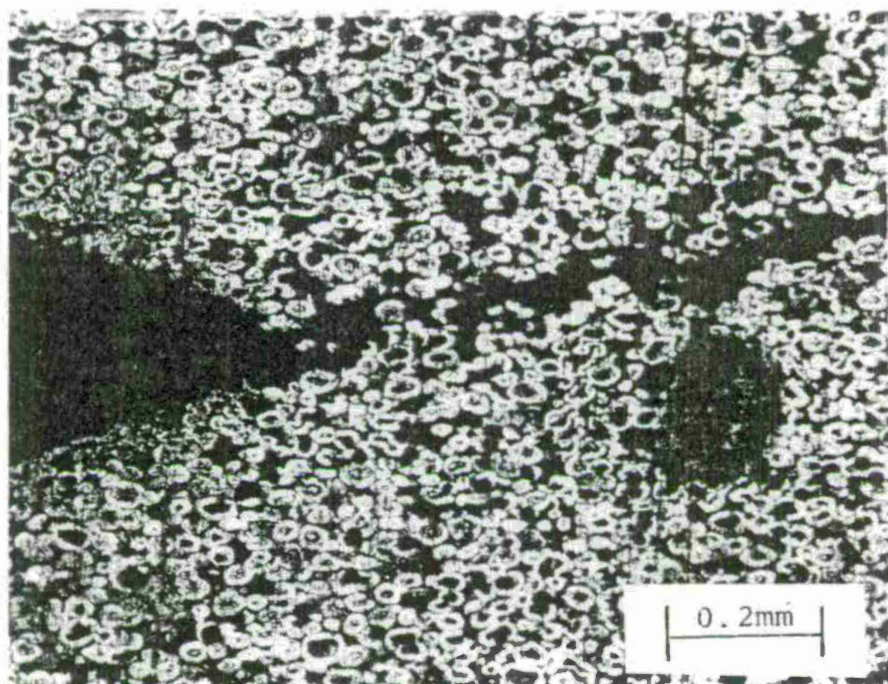


Figure 52    Optical Micrograph Showing Crack Initiation and Propagation of the Cu Diffused W-10 Alloy in 3% NaCl Solution.



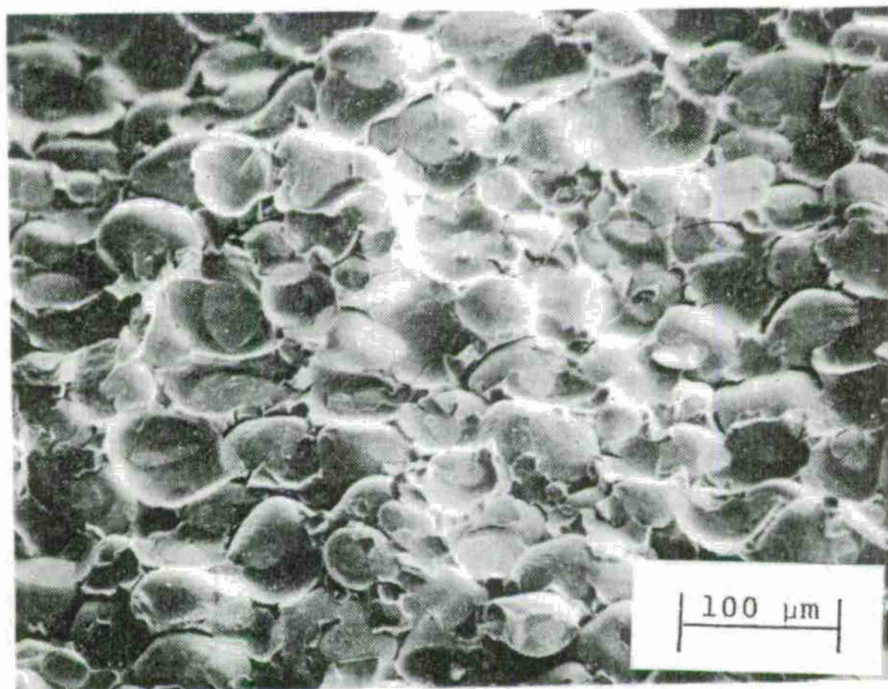
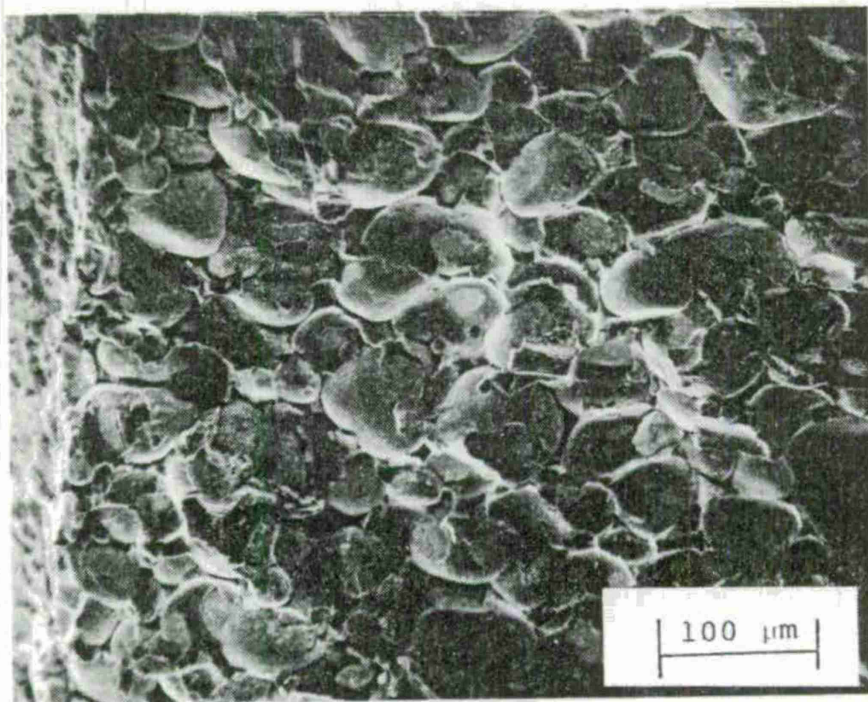
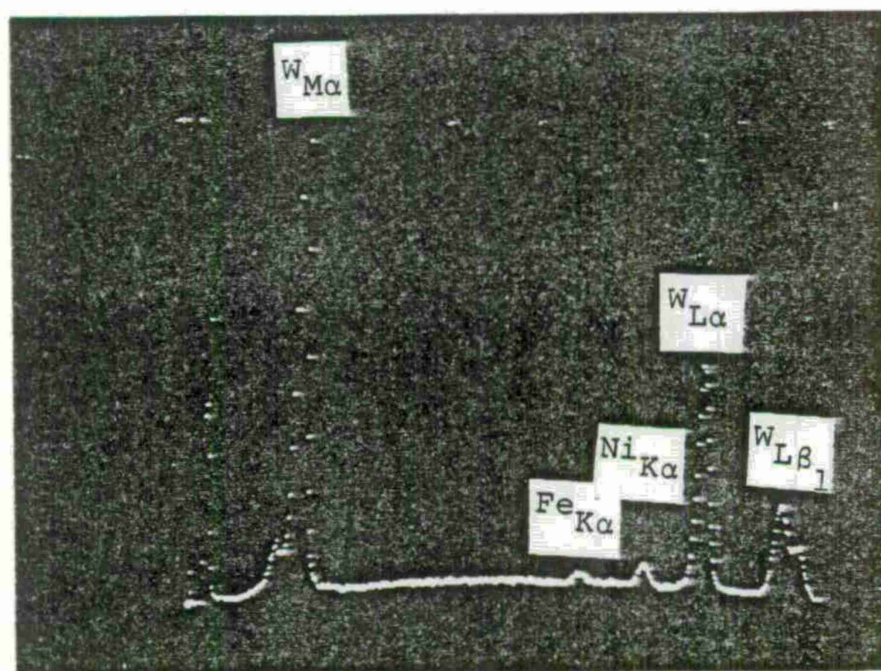
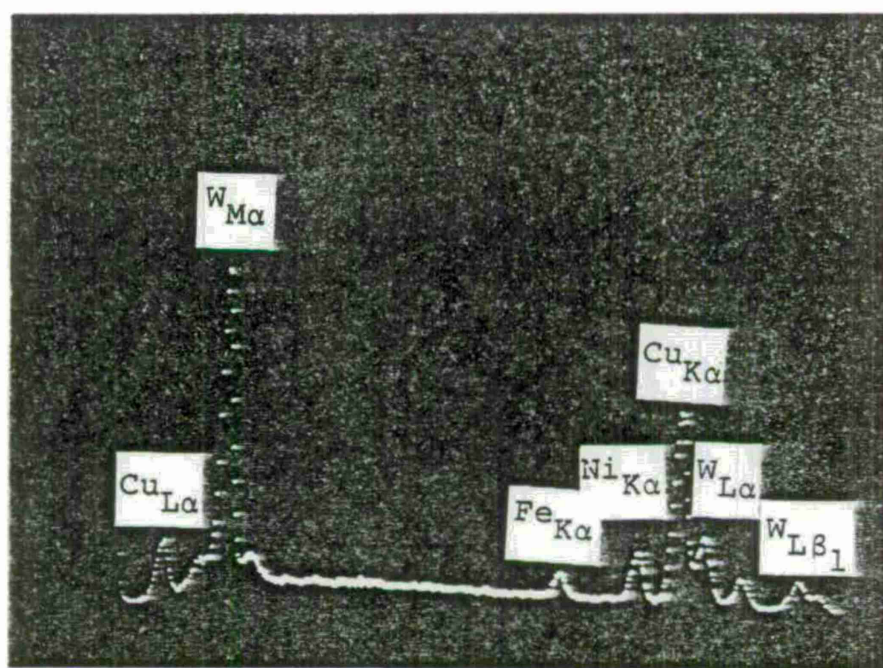


Figure 53      Fracture Appearance of the Cu Diffused W-10 Alloy Specimen Tested in 3% NaCl Solution.





(a)



(b)

Figure 54 EDAX Spectrum of (a) the As-Received W-10 Alloy and (b) the Cu Diffused W-10 Alloy.

### APPENDIX III

#### COPPER ELECTRODEPOSITION

Copper electrodeposition are usually performed in two separate steps: strike coating in dilute cyanide bath up to about 0.1 mil thickness, and plating in the high concentration bath.

Before being coated, mechanically polished specimen was cleaned in acetone and distilled water. Strike coating of copper on the specimen was carried out in dilute cyanide bath whose compositions are listed in Table 6. Operating conditions of the bath are also listed in Table 6. Following the strike coating, about 1 mil of copper was electroplated in the copper sulfate bath. Compositions and operating conditions of the bath are shown in Table 7.

Table 6  
Compositions and Operating Conditions of  
Dilute Cyanide Bath

Compositions:

Cuprous cyanide	22.5 g
Sodium cyanide	34.0 g
Sodium carbonate	15.0 g
Distilled water	1000 ml

Operating Conditions:

Current density	0.2 A/dm <sup>2</sup>
Temperature	30 to 40°C
Cathode	Specimen
Anode	Copper

Table 7  
Compositions and Operating Conditions of  
Copper Sulfate Bath

Compositions:

Copper sulfate	250.0 g
Sulfuric acid	75.0 g
Distilled water	1000 ml

Operating Conditions:

Current density	2-4 A/dm <sup>2</sup>
Temperature	Room temperature
Cathode	Specimen
Anode	Copper



# TECHNICAL REPORT INTERNAL DISTRIBUTION LIST

	<u>NO. OF COPIES</u>
CHIEF, DEVELOPMENT ENGINEERING BRANCH	
ATTN: SMCAR-LCB-D	1
-DA	1
-DP	1
-DR	1
-DS (SYSTEMS)	1
-DS (ICAS GROUP)	1
-DC	1
CHIEF, ENGINEERING SUPPORT BRANCH	
ATTN: SMCAR-LCB-S	1
-SE	1
CHIEF, RESEARCH BRANCH	
ATTN: SMCAR-LCB-R	2
-R (ELLEN FOGARTY)	1
-RA	1
-RM	2
-RP	1
-RT	1
TECHNICAL LIBRARY	5
ATTN: SMCAR-LCB-TL	
TECHNICAL PUBLICATIONS & EDITING UNIT	2
ATTN: SMCAR-LCB-TL	
DIRECTOR, OPERATIONS DIRECTORATE	1
DIRECTOR, PROCUREMENT DIRECTORATE	1
DIRECTOR, PRODUCT ASSURANCE DIRECTORATE	1

NOTE: PLEASE NOTIFY DIRECTOR, BENET WEAPONS LABORATORY, ATTN: SMCAR-LCB-TL,  
OF ANY ADDRESS CHANGES.

# TECHNICAL REPORT EXTERNAL DISTRIBUTION LIST

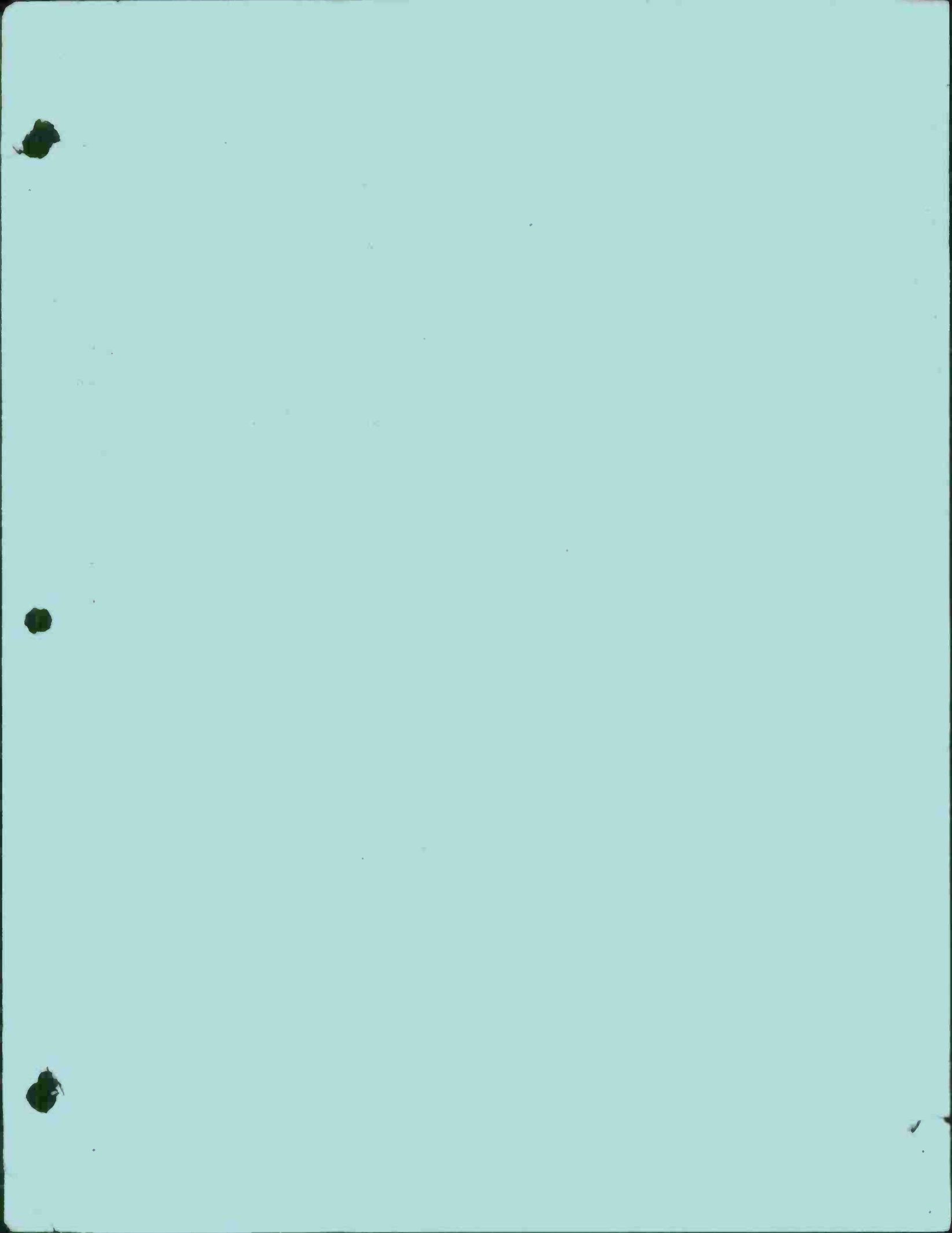
	<u>NO. OF COPIES</u>		<u>NO. OF COPIES</u>
ASST SEC OF THE ARMY RESEARCH & DEVELOPMENT ATTN: DEP FOR SCI & TECH THE PENTAGON WASHINGTON, D.C. 20315	1	COMMANDER US ARMY AMCCOM ATTN: SMCAR-ESP-L ROCK ISLAND, IL 61299	1
COMMANDER DEFENSE TECHNICAL INFO CENTER ATTN: DTIC-DDA CAMERON STATION ALEXANDRIA, VA 22314	12	COMMANDER ROCK ISLAND ARSENAL ATTN: SMCRI-ENM (MAT SCI DIV) ROCK ISLAND, IL 61299	1
COMMANDER US ARMY MAT DEV & READ COMD ATTN: DRCDE-SG 5001 EISENHOWER AVE ALEXANDRIA, VA 22333	1	DIRECTOR US ARMY INDUSTRIAL BASE ENG ACTV ATTN: DRXIB-M ROCK ISLAND, IL 61299	1
COMMANDER ARMAMENT RES & DEV CTR US ARMY AMCCOM ATTN: SMCAR-LC SMCAR-LCE SMCAR-LCM (BLDG 321) SMCAR-LCS SMCAR-LCU SMCAR-LCW SMCAR-SCM-O (PLASTICS TECH EVAL CTR, BLDG. 351N) SMCAR-TSS (STINFO) DOVER, NJ 07801	1 1 1 1 1 1 1 2	COMMANDER US ARMY TANK-AUTMV R&D COMD ATTN: TECH LIB - DRSTA-TSL WARREN, MI 48090  COMMANDER US ARMY TANK-AUTMV COMD ATTN: DRSTA-RC WARREN, MI 48090  COMMANDER US MILITARY ACADEMY ATTN: CHMN, MECH ENGR DEPT WEST POINT, NY 10996  US ARMY MISSILE COMD REDSTONE SCIENTIFIC INFO CTR ATTN: DOCUMENTS SECT, BLDG. 4484 REDSTONE ARSENAL, AL 35898	1       1    2
DIRECTOR BALLISTICS RESEARCH LABORATORY ATTN: AMXBR-TSB-S (STINFO) ABERDEEN PROVING GROUND, MD 21005	1	COMMANDER US ARMY FGN SCIENCE & TECH CTR ATTN: DRXST-SD 220 7TH STREET, N.E. CHARLOTTESVILLE, VA 22901	1
MATERIEL SYSTEMS ANALYSIS ACTV ATTN: DRXSY-MP ABERDEEN PROVING GROUND, MD 21005	1		

NOTE: PLEASE NOTIFY COMMANDER, ARMAMENT RESEARCH AND DEVELOPMENT CENTER,  
US ARMY AMCCOM, ATTN: BENET WEAPONS LABORATORY, SMCAR-LCB-TL,  
WATERVLIET, NY 12189, OF ANY ADDRESS CHANGES.

# TECHNICAL REPORT EXTERNAL DISTRIBUTION LIST (CONT'D)

	<u>NO. OF COPIES</u>		<u>NO. OF COPIES</u>
COMMANDER US ARMY MATERIALS & MECHANICS RESEARCH CENTER ATTN: TECH LIB - DRXMR-PL WATERTOWN, MA 01272	2	DIRECTOR US NAVAL RESEARCH LAB ATTN: DIR, MECH DIV CODE 26-27, (DOC LIB) WASHINGTON, D.C. 20375	1 1
COMMANDER US ARMY RESEARCH OFFICE ATTN: CHIEF, IPO P.O. BOX 12211 RESEARCH TRIANGLE PARK, NC 27709	1	COMMANDER AIR FORCE ARMAMENT LABORATORY ATTN: AFATL/DLJ AFATL/DLJG EGLIN AFB, FL 32542	1 1
COMMANDER US ARMY HARRY DIAMOND LAB ATTN: TECH LIB 2800 POWDER MILL ROAD ADELPHIA, MD 20783	1	METALS & CERAMICS INFO CTR BATTELLE COLUMBUS LAB 505 KING AVENUE COLUMBUS, OH 43201	1
COMMANDER NAVAL SURFACE WEAPONS CTR ATTN: TECHNICAL LIBRARY CODE X212 DAHLGREN, VA 22448	1		

NOTE: PLEASE NOTIFY COMMANDER, ARMAMENT RESEARCH AND DEVELOPMENT CENTER,  
US ARMY AMCCOM, ATTN: BENET WEAPONS LABORATORY, SMCAR-LCB-TL,  
WATERVLIET, NY 12189, OF ANY ADDRESS CHANGES.





BOOK RATE

DEPARTMENT OF THE ARMY

ARMAMENT RESEARCH AND DEVELOPMENT CENTER

BENET WEAPONS LABORATORY, LCWSL

US ARMY ARMAMENT, MUNITIONS AND CHEMICAL COMMAND

WATERVLIET, N.Y. 12189

OFFICIAL BUSINESS

SMCAR-LCB-TL



POSTAGE AND FEES PAID  
DEPARTMENT OF THE ARMY  
DOD - 314

OFFICIAL BUSINESS  
PENALTY FOR PRIVATE USE, \$ 300

COMMANDER  
US ARMY AMCCOM  
ATTN SMCAR-ESP-L  
ROCK ISLAND, IL 61299

DA LABEL 18-1. 1 OCT. 74

RDD \_\_\_\_\_  
(AR 340-3)